Universidade Federal do Rio Grande do Sul

Instituto de Física

Programa de Pós-Graduação em Física

Spin-orbit interactions of light

(Interações spin-orbitais da luz)

Claire Marie Cisowski

Tese realizada sob a orientação do Prof. Dr. Ricardo Rego Bordalo Correia, co-orientada pelo Prof. Dr. Jandir M. Hickmann e apresentada ao Programa de Pós-Graduação do Instituto de Física da Universidade Federal do Rio Grande do Sul para a obtenção do Título de Doutor em Ciências, na Área de Física Experimental.

Porto Alegre, RS, Brazil
May 2019

Funding Agencies: Coordenação de Aperfeiçoamento de Pessoal de Nível Superior (CAPES), Conselho Nacional de Desenvolvimento Científico e Tecnológico (CNPq).

ABSTRACT

In the past decades, technological advances in the field of Optics have allowed to explore electromagnetic fields with rich scalar and vectorial properties. Their study have challenged our understanding of one of a fundamental property of light, namely, angular momentum. In particular, higher-order-Laguerre-Gauss modes have revealed a new type of angular momentum, different from the spin angular momentum carried by homogeneously polarized beams, called orbital angular momentum. This discovery led to passionate discussions regarding the definition of the "spin"and "orbital"parts of light and whether those quantities are independent. Recent studies have indicated that, under special circumstances, spin angular momentum can be converted into orbital angular momentum, shedding light on spin-orbit coupling of light. A general theoretical framework to describe spin-orbit interactions of light is being developed, bringing in a new perspective about the geometric and topological properties of light.

This thesis aims at providing an overview of our current understanding of spin-orbit interactions of light and presents a few original studies to illustrate some of those aspects.

I will first discuss how the spin and orbital parts of light are defined, using both the symmetric energy momentum-based method and the gauge-invariant canonical approach, highlighting the differences and similarities of the two approaches. A brief practical description of beams carrying spin and orbital angular momentum will also be provided. Spin-orbit interactions of light will be introduced by studying how beams of light transform, both from an algebraic and a geometric perspective. It will be shown that specific transformations cause the wavefunction to acquire a so-called "geometric phase". Geometric phases will be defined within the mathematical framework of fibre bundle theory, which emphasises the role of the underlying space properties and allows to draw some analogies between optical systems and other physical systems. Spin-orbit interactions of light will be interpreted in terms of geometric phases. I will review spin-orbit interactions driven by i) the evolution of the parameters describing the optical system ii) the evolution of the states describing the optical system iii) the introduction of correction terms in the equation of motion of the beam centroid.

Two original studies will then be presented. The first one evidences orbit-orbit interactions in a pair of complementary asymmetric beams, obtained upon wavefront division of a cylindrical Laguerre-Gauss beam by a Fresnel Biprism. Both experimental and numerical results reveal angular deviations from geometric expectations, dependent on the incident beam topological charge. The second study is concerned with the transformation of the orbital angular momentum content of an optical beam propagating in a vertical gradient of refractive index. Preliminary results indicate the smooth inversion of the beam topological charge, accompanied by astigmatic changes. In addition to these works, a few illustrative short studies will be presented through this thesis, namely, spin-to-orbit conversion in an air nanoring on a metallic substrate, a practical visualisation of the orthogonality condition in vector vortex beams and a study of the interaction of a pair of vortex cores in a diffracting beam.

RESUMO

Nas décadas passadas, avanços tecnológicos na área da ótica permitiram estudos de campos eletromagnéticos com grandes variações das propriedades escalares e vetoriais. Os estudos destes campos desafiaram a nossa compreensão de uma das propriedades fundamentais da luz, a saber, o momento angular. Modos Laguerre-Gauss de ordens superiores, em particular, revelaram um novo tipo de momento angular, diferente do momento angular de spin característico de feixes homogeneamente polarizados, chamado de momento angular orbital. Esta descoberta levou a discussões sobre a definição das partes do momento angular orbital e de spin da luz e sobre a independência destas quantidades. Estudos recentes indicaram que, em determinadas circunstâncias, o momento angular de spin é convertido em momento angular orbital, evidenciando o acoplamento spin-órbita da luz. Um quadro teórico geral está sendo desenvolvido para descrever as interações spin-órbita da luz, trazendo uma nova perspectiva sobre as propriedades geométricas e topológicas da luz.

Esta tese visa fornecer uma visão geral da nossa compreensão atual das interações spin-orbitais da luz e apresenta alguns estudos originais para ilustrar alguns destes aspectos.

Primeiramente, irei discutir como o spin e a parte orbital da luz são definidos, usando tanto o método baseado no momento simétrico quanto a abordagem da invariância canônica de Gauge, destacando as diferenças e as semelhanças das duas abordagens. Uma breve descrição de feixes carregando momento angular de spin e momento angular orbital também será fornecida. Interações spin-orbitais da luz serão introduzidas estudando como os feixes de luz se transformam, tanto de uma perspectiva algébrica quanto geométrica. Será mostrado que transformações específicas fazem com que a função de onda adquira a chamada "fase geométrica". As fases geométricas serão definidas dentro da estrutura matemática da teoria de fibras que enfatiza o papel das propriedades do espaço subjacente e permite desenhar algumas analogias entre os sistemas óticos e outros sistemas físicos. Interações spin-orbitais da luz serão interpretadas em termos de fases geométricas. Serão revistas as interações spin-órbita causadas i) pela evolução dos parâmetros que descrevem o sistema ótico, ii) pela evolução dos estados iii) e pela introdução de termos de correção na equação de movimento da centroide de feixe.

Dois estudos originais serão apresentados. O primeiro evidencia interações órbita-órbita em um par de feixes assimétricos complementares, obtido na divisão da frente de onda de um feixe de Laguerre-Gauss cilíndrico por um Biprisma de Fresnel. Os resultados revelaram desvios angulares dependentes da carga topológica quando comparado com as expectativas geométricas. O segundo estudo está dedicado à transformação do momento angular orbital de um feixe ótico propagando em um gradiente vertical de índice de refração. Resultados preliminares indicam uma inversão da carga topológica do feixe propagado e mudanças astigmáticas. Além desses trabalhos, alguns breves estudos serão apresentados, tais como conversão spin-órbita em uma nano anel de ar em um substrato metálico, um estudo da condição de ortogonalidade em modos vetoriais e um estudo da interação de um par de vórtices em um feixe difratado.

ACKNOWLEDGEMENTS

I would like to express my sincere gratitude to my advisor Prof. Dr. Ricardo R. B. Correia, for his continuous support and for giving me the chance to pursue a career in optics, he has truly been an outstanding mentor. I will also be forever grateful to Prof. J. M. Hickmann for introducing me to the world of structured light. I would like to thank J. R. Schoffen, Prof. Dr. C. Bonatto, Prof. Dr. S. D. Prado and Prof. Dr. G. G. Martinez Pino for our insightful discussions and for your support. I am also thankful to the committee members, for dedicating some of their time and effort in evaluating this work.

To my high school teachers Mrs Canet for sharing your passion for physics and to Mrs Such for pushing me to improve my English when all hope seemed lost, I am deeply grateful.

To my friends and colleagues from the laboratory, Vinicius, Amanda, Klester, Hemmerson, Eliasibe, Janine, Guilherme, Magnus, Gabriel, Henrique, Wesley and Erico, for sharing our experimental misadventures and celebrating our victories, I wish you a bright future in academia and happiness in your lives, you have made those years exceptional. To Boris and Marion, my friends from France, thank you for always being there for me despite the distance.

To my french family, for their love and encouragements, for travelling such a long distance to visit me, sending care packages and for buying a lot of cheese when I visited them. To my grandfathers, who would have been proud to see me going this far in academia. To my new Brazilian family, who welcomed me with warmth. To my husband Henrique, this thesis would not exist without you, I cannot say how fortunate I am to have you by my side.

CONTENTS

LIST OF FIGURES

LIST OF ABBREVIATIONS

CV	Cylindrical Vector
EOAM	Extrinsic Orbital Angular Momentum
HG	Hermite-Gaussian
LG	Laguerre-Gaussian
LH	Left-Handed
OAM	Orbital Angular Momentum
OHE	Orbital Hall Effect
OV	Optical Vortex
PB	Pancharatnam-Berry
PBOE	Pancharatnam–Berry Optical Elements
RH	Right-Handed
SAM	Spin Angular Momentum
SHE	Spin Hall Effect
SLM	Spatial Light Modulator
SOI	Spin Orbit Interactions
TIR	Total Internal Reflection
VGRIN	Vertical Gradient of Refractive Index

MOMENTUM IN ELECTROMAGNETISM, FOUR-HUNDRED YEARS ON

In 1619, J. Kepler, in his work *De cometis libelli tres*, argued that light corpuscles can exert pressure causing the tail of comets to point away from the sun [1]. This event marked the beginning of four-hundred years of research dedicated to the momentum of light. Formulated during the corpuscular and wave controversy, Kepler's interpretation in terms of corpuscles was challenged by many [2] until J. C. Maxwell established that light is an electromagnetic wave [3]. J. H. Poynting [4], J. J. Thomson [5] and H. Poincaré [6] further developed Maxwell's work by adding the notions of energy fluxes and momentum densities, hereby evidencing that the linear momentum of electromagnetic waves is at the origin of radiation pressure. Radiation pressure being significantly weak, it is only in the early 1900s that the theory was validated by the experimental works of P. Lebedev, E.F. Nichols and G.F. Hull [7, 8].

Shortly after the existence of the linear momentum of light was established, J. H. Poynting, relying on mechanical analogies, argued that electromagnetic waves could also carry angular momentum in an amount of $\sigma\hbar$ per photon, with $\hbar$ being Plank's constant and σ being the photon's helicity [9]. Helicity being the projection of the spin pseudo vector onto the momentum vector, this momentum is known as Spin Angular Momentum (SAM). SAM can be associated with the polarization state of light beams and was measured by R. Beth in 1936 [10]. In 1932, C. Darwin, the grandson of the famous naturalist, speculated on the existence of another type of electromagnetic angular momentum, independent of SAM [11]. However, it is only recently, in the 1990s, that light was shed on the orbital angular momentum (OAM) of light, through the works of E. Abramochkin and V. Volostnikov [12] and L. Allen et al. [13]. Their experimental works showed that Laguerre-Gauss (LG) modes can be obtained from Hermitte-Gauss modes and that beams possessing helical wavefronts, like LG beams, do carry OAM.

While experimental works in the field of micro-manipulation indicate that SAM and OAM can manifest independently [14], it appears that both quantities can become coupled in the non-paraxial regime [15] and in the paraxial regime under specific circumstances [16]. From a macroscopic perspective, spin-orbit interactions (SOI) of light encompass interactions between SAM, OAM and extrinsic orbital angular momentum (EOAM), the later being related to the beam trajectory. Spin-orbit interactions of light is a recent research topic, a theoretical framework is being developed, and some fundamental aspects such as the separation of angular momentum into a spin and orbital part are being debated [17–19].

Throughout history, successive discoveries have disclosed new levels of complexity regarding the momentum of light. SOI appear to be the most recent feature to explore.

This thesis aims at providing an overview of our current understanding of SOI of light and presents two original experimental works dedicated to these phenomena.

Prior to studying the interactions between SAM, OAM and EOAM, it is necessary to define these quantities. This task is of paramount importance to establish a solid background to our study and is particularly relevant since many aspects regarding the spin and orbital parts of light are being actively discussed. Two main approaches have been proposed to define physically meaningful SAM and OAM, thus, it is essential to establish under which circumstances these approaches are equivalent, what are their limitations and what are the implications of choosing one approach over the other. Given the richness of the subject, the first chapter of this thesis will entirely be dedicated to answering these questions. A few practical aspects regarding beams carrying SAM, OAM and EOAM will also be reviewed, intended to readers unfamiliar with structured light.

Once SAM, OAM and EOAM have been defined, I will introduce SOI of light by studying the transformation of light beams, both from an algebraic and a geometric perspective. This will naturally lead to the introduction of geometric phases, which, as it will be demonstrated, can be used to interpret SOI of light. In this thesis, I chose to highlight the geometric nature of SOI of light by complementing the review of K. Bliokh et al. [16] with an overview of fibre bundle theory, in order to provide some insight on the nature of geometric phases and clarify the role of the connection and its curvature, both concepts being issued from the formalism of fibre bundle theory and now encountered in the optics literature [20, 21]. This approach is particularly interesting in order to draw analogies with other physical systems [22].

Having provided a general framework for SOI of light, two original studies dedicated to interactions between OAM and EOAM will be presented. Orbit-orbit interactions have been significantly less studied than their spin-orbit counterparts and present unique features notably because, unlike spin angular momentum, the amount of orbital angular momentum carried by a beam is not restricted to $\pm\hbar$. So far, orbit-orbit interactions have been studied mainly upon symmetry breaking of a beam carrying OAM arising at the sharp interface between two media [23], in a smooth inhomogeneous isotropic medium [21], and by considering a tilted observation plane with respect to the beam propagation direction [24]. In this thesis, we propose, for the first time, to investigate orbit-orbit interactions induced by symmetry breaking using a Fresnel biprism and upon propagation in a vertical gradient of refractive index, respectively. Both experimental and numerical results will be presented for each study.

Unlike experimental set-ups using a mask or a screen to break the symmetry of an incident beam, a Fresnel biprism carries out wavefront division without losing information contained in the screened beam part, as two complementary beam parts are available for analysis. This opens new perspectives regarding the study of beams carrying orbital angular momentum, notably, this configuration increases the precision of orbit-dependent deflection measurements.

Regarding orbit-orbit interactions in an inhomogeneous media, so far, beams carrying OAM have mainly been studied in inhomogeneous media preserving a form of cylindrical

symmetry. It is the first time, to my knowledge, that the transformation of OAM-carrying beams in a vertical gradient of refractive index is investigated. Our study is based on a cost-effective, versatile experimental set-up consisting of a binary solution of distilled water and ethanol, allowing to explore different distributions of refractive index and opening the possibility to introduce optically active particles for future experiments. While at sharp interfaces, total internal reflection occurs abruptly, here, this phenomenon occurs smoothly, which is particularly interesting to study topological inversion of OAM-carrying beams.

THE SPIN AND ORBITAL PARTS OF LIGHT, SOME FUNDAMENTALS

Behind the definition of photonic spin-orbit interactions lays a fundamental question, of apparent simplicity, namely, *what are the spin part and orbital part of light?* This is question deserves special attention and will be addressed in this chapter. It will be shown that despite their straightforward derivation, the spin and orbital parts of light issued from Noether's theorem present some unexpected features challenging their interpretation as physical, observable quantities. Two main approaches are currently used to obtain physically meaningful quantities, one defining a new angular momentum density, which is then split into new spin and orbital densities, and the second one offering either to modify or to reinterpret Noether's spin and orbital densities. Both approaches will be reviewed. A few aspects of practical interest regarding light beams carrying SAM and OAM will also be presented at the end of the chapter.

1.1 DEFINING ANGULAR MOMENTUM THROUGH ROTATIONS

A natural approach for determining the spin and orbital part of light consists of studying field transformations and seeking entities that rotate the directions of the vector field for the spin part, and rotate the field spatial distribution for the orbit part. This is possible by examining Noether's theorem, as demonstrated in what follows.

1.1.1 Field transformations and Noether's theorem

In 1918, E. Noether changed the face of algebra by establishing that the symmetries of a physical system provide conservation laws for fundamental physical quantities [25]. For instance, in point mechanics, the invariance of the action of the system under time translations, spatial translations and spatial rotations provides a conservation law for energy, linear momentum and angular momentum, respectively. Similarly, for free electromagnetic fields, assuming a Minkowski space-time, space-time translations define a canonical energy-momentum tensor $\Theta^{\alpha\beta}$ and rotations define a rank-3 angular momentum tensor $\mathrm{J}^{\alpha\beta\gamma}$, with α and β being spatiotemporal coordinates. The energy-momentum tensor defines the familiar canonical 4-vector momentum density $\mathrm{P}^{\alpha} = \Theta^{0\alpha} = (\mathrm{W}, \mathbf{P}^{i})$, with W and $\mathbf{P}^{i}$ being the field energy density and canonical linear momentum density, respectively, with i denoting spatial coordinates [26].

In the framework of wave optics, where light is described by a scalar wave, the energy-momentum tensor is symmetric and angular momentum consists solely of orbital angular momentum (OAM). Accounting for the vectorial nature of electromagnetic waves causes the canonical energy-momentum tensor to become asymmetric [26], which appears inconsistent with Einstein's symmetric curvature tensor. The angular momentum tensor of a vector field comprises a spin angular momentum (SAM) part in addition to the OAM part such that $\mathrm{J}^{\alpha\beta\gamma} = \mathrm{S}^{\alpha\beta\gamma} + \mathrm{L}^{\alpha\beta\gamma}$, where the orbital part is obtained from the canonical energy momentum tensor

$\mathrm{L}^{\alpha\beta\gamma} = \mathrm{r}^{\alpha}\Theta^{\beta\gamma} - \mathrm{r}^{\beta}\Theta^{\alpha\gamma}$ and where the spin part reflects the vectorial nature of the field [26]. The SAM and OAM spatial densities **S** and **L** of a vector field are given by the pseudo-vectors $\mathbf{S}_i = (\mathcal{E}_{ijk}\mathrm{S}^{jk0})/2$ and $\mathbf{L}_i = (\mathcal{E}_{ijk}\mathrm{L}^{jk0})/2$ with $\mathcal{E}_{aij}$ being the Levi-Civita pseudo-tensor. In what follows, the index i is omitted for clarity. For fields of finite spatial extension, the angular momentum densities can be spatially integrated to give macroscopic (total) SAM and OAM. The canonical spin and orbital densities of a free electromagnetic field can be expressed as [27]:

$$\mathbf{S} = \mathbf{E} \times \mathbf{A}, \quad \text{and} \quad \mathbf{L} = \mathbf{r} \times \mathbf{P} = \mathbf{E} \cdot (\mathbf{r} \times \nabla)\mathbf{A} \tag{1.1}$$

Where $\epsilon_0 = \mu_0 = c = 1$ has been assumed for clarity and the spatial part of the canonical linear momentum density is $\mathbf{P} = \mathbf{E} \cdot (\nabla)\mathbf{A}$. Here, **A** is the magnetic vector potential and **E** is the electric field. The curl of the magnetic vector potential is equal to the magnetic field vector and defines the transverse [1] component of **A**. The longitudinal component of **A** is unspecified and can be set to zero using the Coulomb gauge. This is an important aspect and we shall come back to it later.

In equation (1.1), **L** and **S** have an explicitly dependence on **A**, indicating they are gauge-dependent, i.e, non-observable. This feature, in addition to the fact that the canonical energy momentum tensor is non-symmetrical, cause the canonical spin and orbital momentum densities issued from Noether's theorem to appear non-physical. Experimental works however, have evidenced qualitatively different transfers of SAM and OAM from electromagnetic fields to small trapped particles, OAM causing a particle to orbit about the beam axis and SAM causing the particle to spin about its centre of mass [14]. Thus, a theoretical framework in which the SAM and OAM densities correspond to separate, physical entities should, in principle, exist.

Difficulties to provide a theoretical framework for the spin and orbital parts of light issued from Noether's theorem go beyond the classical framework, as it will now be demonstrated.

1.1.2 The operator formalism

In the first quantization, dynamical variables acting on the classical electromagnetic fields are expressed as operators acting on the photon wavefunction, represented in momentum space [2] [28]. Following Noether's theorem, momentum operators are defined as generators of the Poincaré group and must obey the commutation relations proper to that group. The total canonical angular momentum operator is written as [29]:

$$\hat{\mathbf{J}} = \hat{\mathbf{L}} + \hat{\mathbf{S}} \tag{1.2}$$

With $\hat{\mathbf{L}}$ and $\hat{\mathbf{S}}$ being the canonical OAM and SAM operator, respectively, acting on the classical field modes, and can be expressed as [29] [3]:

$$\hat{\mathbf{L}} = \hat{\mathbf{r}} \times \hat{\mathbf{P}}, \quad \text{and} \quad (\hat{\mathrm{S}}_a)_{i,j} = -\mathrm{i}\mathcal{E}_{aij} \tag{1.3}$$

[1] The adjectives "transverse" and "longitudinal" are defined in relation to the mean wavevector.

[2] The momentum-space representation avoids ambiguities related to the non-locality of the position operator in the coordinate representation.

[3] In reciprocal (Fourier) space.

With $\mathcal{E}_{ijk}$ being the Levi-Civita pseudo-tensor, $\hat{\mathbf{r}}$ being the position operator $\hat{\mathbf{r}} = \mathrm{i}\,\partial_{\mathbf{k}}$ and $\hat{\mathbf{P}}$ being the linear momentum operator with $\hat{\mathbf{P}} = \mathbf{k}$ where $\mathbf{k}$ represents the wavevector [15] [4]. Macroscopic linear momentum and angular momentum are obtained from the expectation values of the respective operators in the state associated with the field. The angular momentum operator $\hat{\mathbf{J}}$ generates rotations of the whole field in agreement with Maxwell's transversality condition for freely propagating beams $\nabla \cdot \mathbf{E} = \nabla \cdot \mathbf{B} = 0$ and $\partial_{\mathrm{t}}\mathbf{E} = \nabla \times \mathbf{B}$, i.e, the field Fourier-components are orthogonal to the wavevector. The operators $\hat{\mathbf{L}}$ and $\hat{\mathbf{S}}$ satisfy the $\mathrm{SO}(3)$ algebra and obey the commutation relations of the Poincaré group. As expected, the operator $\hat{\mathbf{S}}$ for a spin 1 particle generates rotations of directions of the vector fields whereas $\hat{\mathbf{L}}$ generates rotations of the field spatial distribution. However, in general, $\hat{\mathbf{S}}$ and $\hat{\mathbf{L}}$ do not preserve the field transversality [29].

The transversality condition is nevertheless respected in the case of paraxial beams. The paraxial approximation establishes that, for a beam propagating in the z direction with complex amplitude $\mathbf{U(r)} = \mathbf{u(r)}\exp(\mathrm{i}\mathbf{k}\mathrm{z})$, the z-derivative of the complex envelope $\mathbf{u(r)}$, being a slowly-varying function of z, is such that $|\frac{\partial^2 \mathbf{u(r)}}{\partial \mathrm{z}^2}| << |\mathbf{k}\frac{\partial \mathbf{u(r)}}{\partial \mathrm{z}}|, |\frac{\partial^2 \mathbf{u(r)}}{\partial \mathrm{x}^2}|, |\frac{\partial^2 \mathbf{u(r)}}{\partial \mathrm{y}^2}|$. The paraxial Helmholtz equation can be written as:

$$(\nabla_{\perp}^2 + 2\mathrm{ik}\frac{\partial}{\partial \mathrm{z}})\mathbf{u(r)} \approx 0 \tag{1.4}$$

With $\nabla_{\perp}^2$ being the transverse part of the Laplacian. Remarkably, equation (1.4) is analogous to the Schrödinger equation of a two-dimensional harmonic oscillator, the z coordinate replacing the time variable [30]. In paraxial beams, $\hat{\mathbf{L}}$ and $\hat{\mathbf{S}}$ yield OAM and SAM, respectively. A circularly polarized, paraxial beam with a helical phase distribution, propagating in the z-direction, carries both OAM and SAM and is an approximate eigenmode of the operators $\hat{\mathrm{P}}_{\mathrm{z}}, \hat{\mathrm{L}}_{\mathrm{z}}, \hat{\mathrm{S}}_{\mathrm{z}}$ with eigenvalues k, ℓ, σ. Here, σ is the beam helicity and takes values ± 1, it is a pseudoscalar corresponding to the projection of the spin pseudovector upon the propagation direction, the sign discriminating parallel from anti-parallel projections. ℓ is an integer accounting for the number of twists the wave-front performs per unit wavelength [19, 31] [5].

The major issue encountered in the quantum description of SAM and OAM described above is thus the non-respect of Maxwell's transversality condition in the case of general fields.

1.2 Alternative theoretical frameworks

In the literature, two main approaches propose to define physically meaningful spin and orbital parts of light. The first one redefines linear momentum, departing from a symmetric energy momentum tensor and deduces a spin an orbital part from this new quantity. The second approach directly modifies Noether's canonical spin and orbital quantities.

[4] Where $\hbar = 1$ has been assumed

[5] Fractional values of ℓ do not correspond to eigenvalues, it is argued that they contain discontinuities destroying the rotational symmetry [32]

1.2.1 Momentum issued from a symmetric energy-momentum tensor

To obtain physically meaningful spin and orbital momentum densities, one approach consists of constructing a symmetric energy–momentum tensor, hereby redefining a new linear momentum density and new spin and orbital momentum densities. This approach, known as the Belinfante-Rosenfeld approach, is largely taught [33, 34].

The symmetric energy–momentum tensor is constructed from the canonical energy-momentum tensor according to $\mathrm{T}^{\alpha,\beta} = \Theta^{\alpha,\beta} + \partial_\gamma \mathrm{K}^{\alpha\beta\gamma}$ where $\mathrm{K}^{\alpha\beta\gamma}$ is built from the spin tensor $\mathrm{S}^{\alpha\beta\gamma}$ [27]. This defines a 4-vector momentum density, different from the canonical one, which can be expressed as $\mathcal{P}^\alpha = \mathrm{T}^{0\alpha} = (\mathrm{W}, \mathbf{P}_{\mathrm{Poy}})$ where the field linear momentum is defined as $\mathbf{P}_{\mathrm{Poy}} = \boldsymbol{\pi}$. Here, $\boldsymbol{\pi}$ is the well-known, gauge-invariant, Poynting vector $\boldsymbol{\pi} = (\mathbf{E} \times \mathbf{B})$ [6]. In the following, quantities issued from the symmetric energy–momentum tensor are labelled with the subscript $_{\mathrm{Poy}}$. The new linear momentum and angular momentum densities can be expressed as:

$$\mathbf{P}_{\mathrm{Poy}} = \mathbf{E} \times \mathbf{B} \quad \text{and} \quad \mathbf{J}_{\mathrm{Poy}} = \mathbf{r} \times \mathbf{P}_{\mathrm{Poy}} = \mathbf{r} \times (\mathbf{E} \times \mathbf{B}) \tag{1.5}$$

With $\mathbf{E}$ and $\mathbf{B}$ being the electric field and the magnetic field vector, $\mathbf{E}(\mathbf{r}, \mathrm{t})$ and $\mathbf{B}(\mathbf{r}, \mathrm{t})$. $\mathbf{r}$ is the particle position, defined in relation to the origin. An apparent issue with equation (1.5) is that, for purely transverse plane waves, the linear momentum density $\mathbf{P}_{\mathrm{Poy}}$ is longitudinal, turning the angular momentum density null. In reality, optical fields have a finite spatial extent, causing the linear momentum density to acquire a transverse component and to have non null momentum density, i.e, the wave can carry angular momentum.

Now let us examine how the separation into a spin and orbital part is carried out in this case. Let be a monochromatic field of frequency ω propagating in the z-direction. The linear momentum density, averaged over an oscillation period $2\pi/\omega$ is $\mathbf{P}_{\mathrm{Poy}} = \mathrm{Re}(\mathbf{E}^* \times \mathbf{B})$. Using Maxwell's condition $\mathrm{i}\omega\mathbf{B} = \nabla \times \mathbf{E}$, the total linear momentum of the field, averaged over an oscillation period can be written as [35]:

$$\mathbf{P}_{\mathrm{Poy,tot}} = \frac{1}{2\mathrm{i}\omega} \int \mathrm{d}^3\mathrm{r}\, \mathrm{Im}(\mathbf{E}^* \times (\nabla \times \mathbf{E})) \tag{1.6}$$

The corresponding total angular momentum can be expressed as:

$$\mathbf{J}_{\mathrm{Poy,tot}} = \frac{1}{2\mathrm{i}\omega} \int \mathrm{d}^3\mathrm{r}\, \mathrm{Im}(\mathbf{r} \times (\mathbf{E}^* \times (\nabla \times \mathbf{E}))) \tag{1.7}$$

For a field vanishing quickly at $|\,\mathbf{r}\,| \to \infty$:

$$\mathbf{P}_{\mathrm{Poy,tot}} = \frac{1}{2\mathrm{i}\omega} \int \mathrm{d}^3\mathrm{r} \sum_{j=x,y,z} \mathrm{E}_j^* \nabla \mathrm{E}_j \tag{1.8}$$

The total angular momentum of a field of finite spatial extension is, respectively:

$$\mathbf{J}_{\mathrm{Poy,tot}} = \frac{1}{2\mathrm{i}\omega} \int \mathrm{d}^3\mathrm{r} \sum_{j=x,y,z} \mathrm{E}_j^* (\boldsymbol{r} \times \nabla) \mathrm{E}_j + \frac{1}{2\mathrm{i}\omega} \int \mathrm{d}^3\mathrm{r}\, \mathbf{E}^* \times \mathbf{E} \tag{1.9}$$

[6] Once more, $\epsilon_0 = \mu_0 = \mathrm{c} = 1$ has been assumed

Finally, the longitudinal component of the total angular momentum can be expressed as [35]:

$$\begin{aligned}\mathbf{J}_{\mathrm{Poy,tot,z}} &= \frac{1}{2\mathrm{i}\omega}\iint \mathrm{dxdy}\,\mathbf{r}\times(\mathbf{E}^*\times(\nabla\times\mathbf{E})) \\ &= \frac{1}{2\mathrm{i}\omega}\iint \mathrm{dxdy}\sum_{j=x,y,z}\mathrm{E}_j^*\frac{\partial}{\partial\phi}\mathrm{E}_j + (\mathrm{E}_x^*\mathrm{E}_y - \mathrm{E}_y^*\mathrm{E}_x) - \sum_{j=x,y,z}\mathrm{E}_j^*\frac{\partial}{\partial \mathrm{x}_j}(\mathrm{xE}_y - \mathrm{yE}_x)\end{aligned} \tag{1.10}$$

For a paraxial, circularly polarized, helical beam propagating in the z-direction, OAM and SAM are associated with the first and second term of equation (1.10) as the first term exhibits a dependence on ℓ and the second on σ. In this approach, the OAM and SAM densities can be thought as the angular momentum densities issued from an "orbit" part and a "spin" part of the linear momentum density, $\mathbf{P}_{\mathrm{Poy,o}}$ and $\mathbf{P}_{\mathrm{Poy,s}}$, according to $\mathbf{J}_{\mathrm{Poy,o(s)}} = \mathbf{r}\times\mathbf{P}_{\mathrm{Poy,o(s)}}$.

The Poynting vector representing a directional energy flow, it is natural that, in this framework, the spin and orbital parts of the linear momentum density are often interpreted in terms of energy flows. The spin part of the linear momentum density arises from "the optical-frequency rotation of the instant field vectors at every location in the beam cross section" [36] and is related to the spatial distribution of the third Stokes parameter [7] while the orbit part arises from the "rotational behaviour of the instant field distribution around the beam axis" and orbital flow lines are orthogonal to the contours of constant phase [36].

In the nonparaxial limit, the clear separation between OAM and SAM in equation (1.10) no longer holds, the first term depending on both ℓ and σ [35]. S. M. Barnett et. al. proposed to re-establish a clear separation relying on optical and AM flux formulation [37]. However, K. Bliokh et al. [15], relying on the Fourier decomposition of the fields, argued that, for non-paraxial fields, AM cannot be split into a spin part, related to polarization, and an orbital part, related to the wave phase distribution, as spin-orbit coupling terms prevent this separation.

The symmetric energy-momentum-based approach is not the only approach that has been proposed to obtain physically meaningful SAM and OAM densities in the paraxial limit. Another approach proposes to further examine the canonical densities and will now be reviewed.

1.2.2 The canonical spin and orbital densities, re-visited

To address the gauge-invariance issue of E. Noether's canonical SAM and OAM densities, the vector potential can be decomposed as $\mathbf{A} = \mathbf{A}_\parallel + \mathbf{A}_\perp$ according to Helmholz' decomposition, with $\nabla\times\mathbf{A}_\parallel = 0$ and $\nabla\cdot\mathbf{A}_\perp = 0$. Gauge transformations only affect the longitudinal part [38], therefore, gauge-invariant quantities can be obtained by using only the transverse part of the vector potential to define the SAM and OAM densities [39]:

$$\mathbf{S}_{\mathrm{gic}} = \mathbf{E}\times\mathbf{A}_\perp \quad \text{and} \quad \mathbf{L}_{\mathrm{gic}} = \sum_i \mathrm{E}^i(\mathbf{r}\times\nabla)\mathrm{A}_\perp^i \tag{1.11}$$

This approach is equivalent to an another approach, which consists of choosing to use the Coulomb gauge. The $_{\mathrm{gic}}$ subscript labels gauge-invariant canonical quantities.

[7] The spin flow was represented by a cell model in the transverse plane by A. Bekshaev et al. [36]

While the gauge-invariance issue is apparently solved, the SAM and OAM densities in equation (1.11) are now Lorentz-covariant, which also appears non-physical. However, it has been argued that Lorentz-covariance may not be essential [40]. Indeed, in practice, measuring momentum densities implies choosing a reference frame, where the probe performing the measure is at rest. Also, the majority of optical applications involves monochromatic electromagnetic waves, which also require to single out a reference frame to be well-defined. Note that the total SAM and OAM obtained upon spatial integration of $\mathbf{S}_{\mathrm{gic}}$ and $\mathbf{L}_{\mathrm{gic}}$ are well-defined, separately conserved, and can be calculated in any reference frame.

Let us further examine the corresponding spin and canonical densities. For a monochromatic field in the Coulomb gauge, $\mathbf{A}(\mathbf{r}) = -\mathrm{i}\omega^{-1}\mathbf{E}(\mathbf{r})$. The SAM, linear momentum and OAM densities, averaged over an oscillation period, are defined as [27]

$$\mathbf{S}_{\mathrm{gic}} = \frac{1}{2\omega}\mathrm{Im}(\mathbf{E}^* \times \mathbf{E}), \quad \mathbf{P}_{\mathrm{gic}} = \frac{1}{2\omega}\mathrm{Im}(\mathbf{E}^* \cdot (\nabla)\mathbf{E}), \quad \text{and} \quad \mathbf{L}_{\mathrm{gic}} = \mathbf{r} \times \mathbf{P}_{\mathrm{gic}} \tag{1.12}$$

For a paraxial, circularly polarized, helical vortex beam propagating in the z-direction, both the linear momentum density $\mathbf{P}_{\mathrm{gic}}$ and OAM density $\mathbf{L}_{\mathrm{gic}}$ have an azimuthal and a longitudinal component [41]. The spin density is longitudinal and depends on the beam helicity [41]. The OAM density is extrinsic and the spin density intrinsic. The adjectives extrinsic and intrinsic indicate that a quantity is dependent, or independent, from the definition of the origin, respectively. Note that a transverse, helicity independent SAM density has been reported in structured optical fields, such as evanescent waves or focused beams [41].

The total linear momentum, OAM and SAM of a paraxial beam, are obtained by spatial integration of the respective densities over the beam transverse cross-section. Upon spatial integration, we find that the total OAM has become intrinsic and longitudinal. The total linear momentum, OAM and SAM of the field can be expressed as $\mathbf{P}_{\mathrm{gic,tot}} \propto \mathbf{k}_{\mathrm{av}}$, $\mathbf{L}_{\mathrm{gic,tot}} \propto \ell(\mathbf{k}_{\mathrm{av}}/\mathrm{k})$ and $\mathbf{S}_{\mathrm{gic,tot}} \propto \sigma(\mathbf{k}_{\mathrm{av}}/\mathrm{k})$ with $\mathbf{k}_{\mathrm{av}} \propto \mathrm{k}\vec{z}$ being the mean wavevector. The subscript av labels mean quantities. Consequently, for paraxials fields, we recover the correspondence of helicity and the beam topological charge with SAM and OAM, respectively.

Intrinsic OAM, as defined above, corresponds to the amount of OAM calculated with respect to the field centroid. A transverse, macroscopic, extrinsic orbital angular momentum (EOAM) can be imparted to the beam by considering a shift of the beam centroid [8] in the transverse plane. In this case, EOAM is expressed as $\mathbf{L}_{\mathrm{tot,ext}} = \mathbf{r}_{\mathrm{av}} \times \mathbf{P}_{\mathrm{tot}}$ where $\mathbf{r}_{\mathrm{av}}$ is the beam mean position [41]. EOAM is determined by the beam position and direction of propagation, which is why EOAM is related to the beam trajectory.

Similar results are obtained within the symmetric energy-momentum tensor approach, namely, intrinsic, longitudinal SAM and intrinsic, longitudinal OAM for paraxial beams. Also,

[8] The field centroid may be defined considering coordinates weighted with either the energy density, the energy-flux density, or the photon-number density. All coincide for paraxial monochromatic beams [41].

IOAM can be introduced in a similar way that the one described directly above.

Like in the symmetric energy-tensor approach, the proportionality of the longitudinal components of total SAM and OAM to the polarization helicity and the vortex charge, respectively, is valid in the paraxial approximation only. In non-paraxial beams, the OAM term presents and additional helicity-dependent term [15].

From a quantum perspective, S. J. Van Enk and G. Nienhuis applied the second quantization, where the fields are represented by quantum operators acting on the photons Fock states, on $\mathbf{S}_{\mathrm{gic}}$ and $\mathbf{L}_{\mathrm{gic}}$ [29]. They obtained operators consistent with the transversality condition, however, the operators possess commutation relations different from the $\mathrm{SO}(3)$ algebra, indicating that they do not correspond to genuine SAM and OAM operators. The eigenvalues of $\hat{\mathbf{S}}_{\mathrm{gic,z}}$ and $\hat{\mathbf{L}}_{\mathrm{gic,z}}$ are, in general, continuous but become approximately integers multiples of $\hbar$ for paraxial fields [31]. In the first quantization, K. Bliokh et al. added spin-orbit correction terms to the gauge-dependent canonical operators $\hat{\mathbf{S}}$ and $\hat{\mathbf{L}}$ [15]. The so-obtained operators are in agreement with the transversality condition, however, they also do not satisfy the $\mathrm{SO}(3)$ algebra and present the same commutation relations as the ones of S. J. Van Enk and G. Nienhuis.

The gauge-invariant canonical and the symmetric energy-momentum tensor approach appear to be equivalent regarding various aspects. The symmetric energy-momentum tensor being built from the spin tensor, it is natural that, in the scalar approximation, $\mathbf{P}_{\mathrm{Poy}} = \mathbf{P}_{\mathrm{gic}}$. Also, generally, the macroscopic quantities $\mathbf{J}_{\mathrm{Poy,tot}}$ and $\mathbf{J}_{\mathrm{gic,tot}}$ differ by surface terms at infinity and are equal for fields vanishing at infinity, which is often the case experimentally [17].

The major difference between the two approaches is that locally, the densities $\mathbf{S}_{\mathrm{Poy,z}}$ and $\mathbf{S}_{\mathrm{gic,z}}$ remain dramatically different and cannot be both simultaneously correct. E. Leader argued that the correct density could be determined experimentally by using tiny probe particles and showed that numerical results seem to favour the $\mathbf{S}_{\mathrm{gic,z}}$ version [42]. In another work, E. Leader pointed out that, for a paraxial, circularly polarized optical vortex beam, the cycle averaged density $\mathbf{J}_{\mathrm{Poy,z}}$ per photon does not give $\hbar(\ell + \sigma)$ while $\mathbf{J}_{\mathrm{gic,z}}$ does [17]. Of course, integrating over the beam cross section results in $\hbar(\ell+\sigma)$ per photon for $\mathbf{J}_{\mathrm{Poy,z}}$. In an unpublished work of 2012, X. B. Chen and X. S. Chen [43] argued that the experiment of D. P. Ghai et al. [44], in which ℓ and σ_z dependent shifts are observed in the diffraction fringes issued from single slit diffraction of beams with a phase singularity, does favour the $\mathbf{J}_{\mathrm{gic}}$ version. Some works such as the one of V. Garcés-Chávez et. al. [14] evidenced that rotations issued from SAM and OAM transfer to a trapped particle in a "Bessel" beam are in agreement with the symmetric energy-momentum version. However, others studies claim that it is the interaction of $\mathbf{S}_{\mathrm{gic}}$ that is witnessed in AM transfer to trapped particles [41]. E. Leader argued that it would be incorrect to interpret the results of V. Garcés-Chávez et. al. in favour of the symmetric energy-momentum expression as the same functional dependence applies to the gauge-invariant canonical counterparts. E. Leader also added that this equivalence holds as long as the beam

complex amplitude follows a simple power law behaviour $|\,\mathrm{u}\,|^2 \propto \rho^{-\beta}$, with ρ being the radial distance to the beam axis [17]. As for linear momentum, measurements of the optical forces in evanescent waves exerted on ultra-sensitive nano-cantilevers seem to indicate that it is the canonical version that produces radiation pressure [45]. Other arguments in favour of the gauge-invariant canonical version can be found in the review of K. Bliokh and F. Nori [41]. The canonical momentum density also seems to appear in quantum weak measurements [46, 47]. Finally, the canonical version allows to account for superluminal momentum $|\,\mathbf{P}\,|/\mathrm{W} > c$, with W being the energy density, witnessed in super-momentum transfer per photon, as observed near optical-vortex cores [48].

1.2.3 Complementary remarks

Separate conservation of SAM and OAM should entail the existence of continuity equations describing the local transport of SAM and OAM [29]. This aspect is often left untreated, therefore no consensus has, to my knowledge, yet been reached on that subject.

Continuity equations for SAM and OAM have been proposed for complex fields [37, 49, 50], which are valid for monochromatic fields with time-independent complex amplitudes.

R. P. Cameron et al. have proposed continuity equation for SAM in the dual-symmetrized spin representation [51]. It is true that Maxwell's equations for free electromagnetic field presents a dual-symmetry, in a sense that the electric and magnetic fields are treated on the same footing. In the dual-symmetric representation, **P**, **L** and **S** can be written as the sum of an electric and a magnetic contribution. Practical applications however, often involve light-matter interactions, generally revealing the electric component only. For this reason, electric-biased description, also known as "standard" description is also commonly used.

K. Bliokh et al. provided continuity equations in the standard representation for SAM and OAM relying on spin-orbit corrected tensors $\tilde{\mathrm{S}}^{\alpha\beta\gamma} = \mathrm{S}^{\alpha\beta\gamma} - \Delta^{\alpha\beta\gamma}$ and $\tilde{\mathrm{L}}^{\alpha\beta\gamma} = \mathrm{L}^{\alpha\beta\gamma} + \Delta^{\alpha\beta\gamma}$ such that $\partial_\gamma \tilde{\mathrm{S}}^{\alpha\beta\gamma} = \partial_\gamma \mathrm{L}^{\alpha\beta\gamma} = 0$ [27]. The corresponding SAM and OAM densities coincide with the canonical densities **S** and **L** and the respective fluxes introduce SOI-correction terms describing nonparaxial beams. In the dual-symmetric representation, the spin-orbit correction terms are modified and the spin conservation law coincide with the one of R. P. Cameron et al.. In the same work, K. Bliokh et al. showed that Maxwell's equations allow conservations of SAM and OAM in both the standard and dual-symmetric representation, i.e, the 'electric' and 'magnetic' parts of the spin and orbital AM densities are separately-conserved.

K. Bliokh et al. [27] also showed that, for nonparaxial monochromatic beams, the ratio of spin and orbital AM fluxes to the energy flux is given by $\sigma \cos\theta_0/\mathrm{k}$ and $(\ell + \sigma(1-\cos\theta_0))/\mathrm{k}$ respectively such that the total AM is equal to $(\sigma + \ell)/\mathrm{k}$. The separation into a spin and orbital part is nontrivial because of the spin-to-orbital AM conversion term $\sigma(1-\cos\theta_0)/\mathrm{k}$.

As a final note on the spin and orbit part of light, presented from a theoretical perspective, it should be emphasised that in all of the above only freely propagating beams have been considered, very few works have treated optical SAM and OAM in matter [52]. It was also assumed that the beams are axially-symmetric.

Now that we have discussed how the spin and orbital parts of light can be defined, a few practical aspects regarding beams carrying SAM, OAM and EOAM can be reviewed. For a clearer description, only paraxial beams will be considered. Readers familiar with beams carrying SAM and OAM may skip this section and continue to Chapter 2.

1.3 Practical considerations

1.3.1 Beams with helical wavefronts and polarized light

In both the symmetric energy-momentum energy tensor and the gauge-invariant canonical approaches, total AM can be separated into a SAM and OAM in paraxial beams.

A paraxial, circularly polarized beam carries longitudinal, intrinsic, SAM, as illustrated on figure (1.a). Each photon carries SAM in an amount of $\sigma\hbar$, with $\sigma = \pm 1$ being the beam helicity, the projection of the spin upon the propagation direction. The sign discriminates beams of opposite polarization handedness. A paraxial beam with an helical phase distribution carries longitudinal, intrinsic OAM (IOAM), as illustrated on figure (1.b). In this case, each photon carries OAM in an amount of $\ell\hbar$, with ℓ being an integer accounting for the number of twists the wave-front performs per unit wavelength. Finally, EOAM can be imparted to the beam by considering a transverse shift of the beam centroid, as illustrated on figure (1.c) [16].

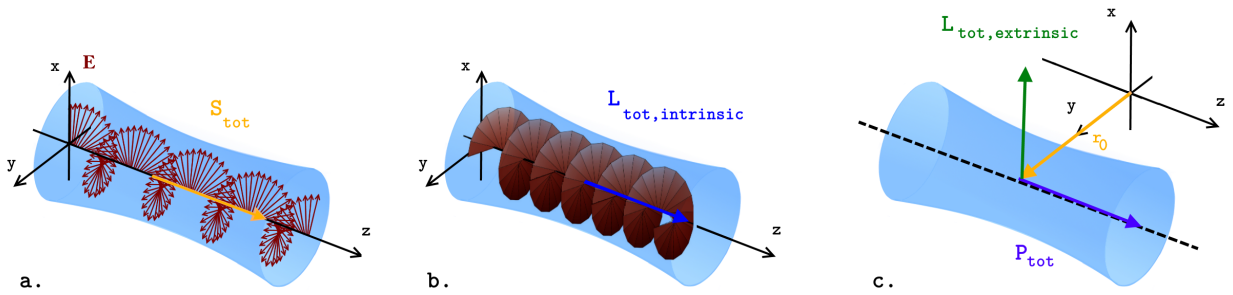

Figure 1 – Angular momentum in a paraxial optical beams. a. A circularly polarized beam carries longitudinal, intrinsic, SAM. b. A paraxial beam with a helical wavefront caries longitudinal, intrinsic OAM. c. A transverse displacement of beam centroid $\mathbf{r}_0$ produces a transverse, extrinsic OAM. Figure adapted from the work of K. Y. Bliokh et al. [16]

A paraxial, circularly polarized, helical beam with a transverse displacement of its centroid with respect to the origin carries SAM, IOAM and EOAM simultaneously. In paraxial beams, SAM, IOAM and EOAM are associated with the beam polarization state, its phase distribution and its trajectory, respectively.

Let us now further describe polarized beams and beams with helical phase distribution. The latter being less known then the former, it will benefit from a more elaborated description.

Polarization characterises electromagnetic oscillations upon propagation. The adjectives "Elliptical", "Linear" and "Circular" refer to the projection of the electric field vector locus in the transverse plane. Fully polarized light beams often refer to paraxial light beams that are homogeneously polarized, meaning that the photons in the beam transverse plane are in the same polarization state. Birefringent elements such as waveplates are useful tools to control the beam polarization state. In short, when entering a birefringent medium, the electric field can be decomposed into two components, one aligned with the material fast axis, for which light encounters a lower index of refraction and travels faster than the other component, aligned with the material slow axis. A birefringent element introduces a retardation, or phase shift, between the polarization components along the fast and slow axis, causing the wave polarization state to change. In addition to retarders, polarizers can also act on the polarization state, behaving like optical filters or absorbers, only letting light in a specific polarization state pass through. Homogeneously polarized light has been extensively studied and has found applications in various areas such as imaging, sensing and communications [53].

The adjective "helical" in "helical beam" refers to the beam helical wavefront, i.e., equiphase point surface. Helical beams are described by scalar fields, which complex amplitude can be written, in Cartesian coordinates, as [54]

$$\mathrm{u}(\mathrm{x},\mathrm{y}) = \mathrm{Re}(\mathrm{x},\mathrm{y}) + \mathrm{iIm}(\mathrm{x},\mathrm{y}) \tag{1.13}$$

Helical beams generally possess a central scalar singularity, also known as optical vortex due to its mathematical similarity with superfluid vortices [55]. Scalar singularities are located where the complex scalar field is null, i.e., where both its real part and its imaginary part are null, or, in other words, where the amplitude is null and the phase undefined. In cylindrical coordinates, the complex amplitude presents a characteristic azimuthal phase dependence [54]:

$$\mathrm{u}(\mathrm{r},\phi) = \mathrm{r}^{\ell}\mathrm{exp}(\mathrm{i}\ell\phi) \tag{1.14}$$

Where ϕ is the azimuthal angle. Around the singularity, the phase circulates by $2\ell\pi$ in one complete circuit, with ℓ being the vortex topological charge. The vortex topological charge corresponds to the scalar product of the vortex order with its sign, the latter distinguishing clockwise from counter-clockwise phase circulation. The net topological charge in a bounded region is a conserved quantity provided no charge enters nor leave the region [54]. Figure (2) illustrates different wavefronts, phase and intensity distributions, namely, the ones of a plane wave and of two helical beams carrying optical vortices of different topological charge.

It is the helical phase distribution around the singularity that carries IOAM, not the singularity itself. Vortices of unit topological charge embedded in non-diffracting beam form threads in the 3D representation, i.e, singular points in the 2D representation. The angle formed by the zeroes of the field real and imaginary parts determines the vortex type, which can be canonical in the case of a right angle or non-canonical for a general angle. Unlike canonical vortices, the phase increment around non-canonical vortices is not linearly proportional to the

azimuthal angle and the intensity pattern presents a radial asymmetry [54, 56].

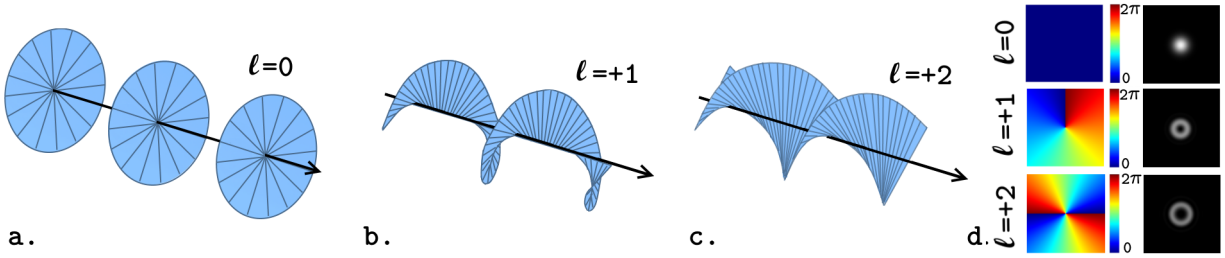

Figure 2 – Wavefront (a, b, c), phase (left column) and intensity (right column) distributions (d) of a Gaussian beam and of an helical beam carrying an optical vortex of topological charge $\ell = +1$ and $\ell = +2$.

Vortices of topological charge $|\ell| > 1$ tend to be unstable upon propagation, and decay into first-order vortices, which sign can differ from the original vortex. Non-integer topological are also unstable as they do not represent eigenmodes of the paraxial wave equation [57]. Their stability can be improved by mode superposition [58]. Optical fields can carry several optical vortices, such is the case of fields issued from random scattering or multiple (at least three) beam interference [59–61]. Historically, it is in this type of beams that phase singularities were studied for the first time [62]. In this case, the field total OAM issued from multiple singularities generally cancels out. Superposing paraxial optical vortex beams can produce knots in the line that follows the phase singularity in 3D [63]. Additional information about optical vortices can be found in the works of I. Freund, F. S. Roux and in the book of D. L. Andrews and M. Babiker [54, 56, 64].

Helical beams encompass modes that are exact and orthogonal solution of the paraxial wave equation such as high-order ($\ell \neq 0$) Laguerre-Gaussian (LG), Hermite-Gaussian and Ince–Gaussian modes. Bessel beams, and Mathieu beams also present an helical wavefront [65]. LG modes, in particular, are easy to obtain. They were first produced by converting higher-order HG modes in laser cavities [66, 67]. Mode conversion is achieved by introducing a phase shift between orthogonal modes of the same order and has been performed using pairs of cylindrical lenses or in stressed fibres [68, 69]. Helical beams can also be obtained by direct wavefront shaping using spiral phase plates [70]. Spiral phase plates possess an azimuthal refractive index gradient imparting a space-variant phase retardation upon transmission and are designed for a specific wavelength. In the optical domain, pure modes can be difficult to obtain using a spiral phase plate due to manufacturing challenges.

In practice, helical beams are often generated using Holography. Holograms are complex far-field diffraction patterns obtained by interfering a reference wave with the wave one wishes to generate. They can be dynamically displayed on Spatial light modulators (SLM). A blazed grating modulated with a helical phase form a fork hologram, which dislocation indicates the phase singularity [71]. A fork hologram generates, in its first diffraction order, a beam carrying a topological charge matching the one of the hologram when the incident beam is normal and centred on the hologram bifurcation [72]. Helical beams with dominant radial order

$\mathrm{p} = 0$ can be obtained from phase holograms [73], however, for a better definition of p, holograms of intensity and phase are required [74, 75].

As it will be discussed in the next chapter, devices relying on spin to orbit conversion are ideal methods to perform wavefront shaping. Finally, direct emission of photons carrying OAM has also been reported using nanoscale chromophores [76].

Helical wavefronts can be characterized using a Shack-Hartmann wavefront sensor [77], by examining intensity distributions issued from interference [78], diffraction [44, 79, 80], free propagation of partially blocked fields [81], distortions induced from an astigmatic lens [82]. Also, fork diffraction gratings can be used in reverse to identify single OAM modes [44]. Mode sorters relying on transforming the azimuthal position of the input beam into a transverse position in the output beam have also been proposed [83]. Finally, quantum Zeno interrogators have been proposed as non-destructive filters to measure OAM modes [84].

The recent interest in beams carrying OAM is due to their wide range of applications [85]. To cite a few, they have been used in the field of micro-manipulation [86], nano-fabrication [87, 88] and imaging [89–92]. They are also promising information carriers as mutually orthogonal states can be multiplexed and the OAM states are defined in an unbounded Hilbert space [93]. Practical limitations however exist due to the carrier beam's finite radius and the aperture of the transmission and receiving optics, indeed, the beam OAM distribution and its azimuthal span are related by an uncertainty condition [94]. Finally, OAM-carrying beams also present interesting properties when propagating in non-linear media [95–97] and have been used as annular waveguides [98].

Recently, a new category of optical beams possessing inhomogeneous polarization and phase distributions, has received significant interest, namely, inhomogeneously polarized beams.

1.3.2 The special case of inhomogeneously polarized beams

Beams with inhomogeneous polarization distribution encompass full-Poincaré beams [99] and cylindrical vector beams [100]. As illustrated on figure (3), cylindrical vector beams present a spatial distribution of linearly polarized photons of varying orientation, whereas full-Poincaré beams exhibit a polarization distribution where circular, elliptical and linear polarization states coexist. Inhomogeneous polarization distributions can be encountered in the beam transverse plane of paraxial beams and in the full three-dimensional spatial distribution of non-paraxial beams [101, 102].

Non paraxial inhomogeneously polarized beams can contain polarization singularities such as C^{T} lines, along which the field is circularly polarized and where the orientation of the ellipse of vibration of the field vector is undetermined. On L^{T} lines the polarization state is linear, i.e, the handedness of the elliptical vibration is undetermined. Finally, along D lines the magnitude of the field vector vanishes.

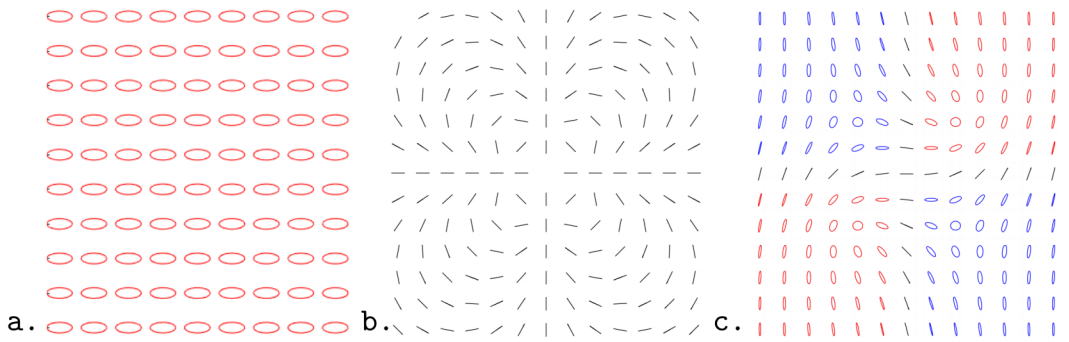

Figure 3 – Examples of polarization distributions in the transverse plane of a a. Homogeneously, elliptically polarized beam, b. Vector beam, c. Poincaré beam. The red and blue colour distinguish right handed from left handed polarized states.

In paraxial fields, similar structures are present in the transverse plane, on C lines the transverse field is circular while on L the transverse fields are linear. Polarization singularities are not related to significant features of angular momentum [103]. The number of lines where the semimajor axes of the ellipses are radially orientated originating from C-point define the category of the C-points which include "lemons", "stars" and "monstars" [104] [9]. Polarization singularities are unstable under perturbations such as external fields [106] or inhomogeneities [107]. Optical vortices unfolding through a birefringent crystal can create complicated networks of C lines and L surfaces, evidencing the existence of interplay between optical vortices, C lines and L surfaces [108].

Cylindrical vector (CV) beams can be generated inside a laser cavity by inserting axial birefringent or axial dichroic components [109, 110]. CV beams can also be obtained with intracavity interferometric methods combining Hermite Gauss modes [111]. In free space, devices with spatially variant polarization properties [112] or capable of rotating an incident polarization state [113] can produce CV beams from homogeneously polarized beams. CV beams have also been generated in multimode fibers by exciting TE_{01} and TM_{01} modes without exciting the HE_{11} fundamental mode by using misalignment methods [114] or by pre-determining the exciting mode phase or polarization [115].

The recent interest in CV beams can partially be attributed to their remarkable focusing properties. Indeed, radially polarized CV beams can be more tightly focused than homogeneously polarized beams [116] and present a strong longitudinal component. This lead to applications in high resolution imaging [117] optical trapping [118] and laser machining [119]. Radially polarized beams are also excellent candidates for surface plasmon excitation in axially symmetric geometries [120].

An excellent review of CV beams, presenting some fundamental and practical aspects, can be found in the work of Q. Zhan [100].

[9] Please refer to the book of D. Andrews for a complete description [105].

To sum up Chapter 1, it has been shown that defining the spin and orbital part of light is not a straightforward task and that two main approaches are competing to define the spin and orbital angular momentum densities. Both approaches however reach similar qualitative results. Notably, in the paraxial approximation, total AM can be divided into SAM, IOAM and EOAM, which can be associated with polarization, phase distribution and the beam trajectory, respectively. In the non-paraxial approximation, the appearance of spin-orbit coupling terms turns the separation of AM into a spin and orbit part difficult. A few practical aspects regarding paraxial beams carrying SAM and IOAM have been reviewed, inhomogeneously polarized beams have also been introduced.

Now that SAM, OAM and EOAM have been defined for paraxial beams, their mutual interactions can be studied. This will be the subject of interest of Chapter 2.

SPIN-ORBIT INTERACTIONS OF LIGHT

From a macroscopic perspective, spin-orbit interactions (SOI) of light encompass mutual conversions between SAM, OAM and EOAM, as defined in paraxial beams. To describe how these conversions take place, I will adopt a semi-classical approach. First, I will describe a light beam in terms of its quantum states and study their transformations from both an algebraic and a geometric perspective. This will allow to introduce the concept of geometric phase. It will be shown that specific variations of the wavevector or (and) the state of the beam, lead, according to Maxwell's equations, to a distribution of geometric phase associated with macroscopic SOI of light. Continuing with a geometric interpretation of SOI of light, it will be shown that the curvature of the quantum fibre bundle associated with the geometric phase causes dynamical effects, leading to spin, or orbital, -dependent trajectory changes.

2.1 REPRESENTATION AND TRANSFORMATION OF LIGHT BEAMS

In order to describe SOI of light, I will first consider a beam of light as a quantum system and study how the corresponding quantum states transform, both from an algebraic and a geometric perspective. Unlike the algebraic approach, the geometric representation is limited to the description of simple systems but provides a more intuitive understanding of the evolution of the physical system. The concept of geometric phase will then be introduced, within the mathematical framework of fibre bundle theory. Fibre bundle theory is an elegant mathematical framework which provides a unified background to study physical systems, ranging from classical and molecular dynamics, quantum dynamics, solid states physics and optics [22].

2.1.1 Quantum states of light

Let us first recall a few fundamental concepts of quantum mechanics. In quantum theory, a physical system is described in terms of its quantum states. From an algebraic perspective, a pure quantum state is represented by a column vector denoted by a ket $|\psi\rangle$. According to the superposition principle, a linear combination of pure quantum states yields another pure quantum state of the system in the following manner:

$$|\psi\rangle = \sum_{n} c_n |\psi_n\rangle \tag{2.1}$$

Where $|\psi_n\rangle$ constitute an orthonormal basis set and c_n are complex numbers. Operators act as linear functions on quantum states. Hermitian operators $\hat{A}^\dagger = \hat{A}$ are particularly important in physics as they are related to observables. Their eigenvalues λ_n are real and obey the eigenvalue equation $\hat{A}|\lambda_n\rangle = \lambda_n |\lambda_n\rangle$ where $|\lambda_n\rangle$ are orthonormal eigenstates. When measured, the observable associated with $\hat{A}$ yields one of the real eigenvalues of $\hat{A}$. For a non-degenerate normalized state $|\psi\rangle = \sum_n c_n |\lambda_n\rangle$, the probability of the outcome λ_n of a measurement is $|c_n|^2$.

The mean value of the observable A found from measurements on an ensemble identically prepared system is the expectation value of the corresponding operator $<\hat{\mathrm{A}}>$. Naturally, this is an extremely simplified description of quantum systems, but it will suffice for what follows, a detailed description of quantum systems can be found in the book of S. M. Barnett [121]. Also, in what follows, when possible, only pure quantum states will be considered for clarity, mixed quantum states also exist and should be treated with special considerations.

The simplest quantum system is the two-state quantum system, also known as qubit. In this case, a pure state is defined within a two-dimensional complex Hilbert space as [122]:

$$|\psi\rangle = \mathrm{c}_1 |0\rangle + \mathrm{c}_2 |1\rangle = \mathrm{c}_1 \begin{pmatrix} 1 \\ 0 \end{pmatrix} + \mathrm{c}_2 \begin{pmatrix} 0 \\ 1 \end{pmatrix} = \begin{pmatrix} \mathrm{c}_1 \\ \mathrm{c}_2 \end{pmatrix} \tag{2.2}$$

Where $\mathrm{c}_1, \mathrm{c}_2$ are complex numbers and where the vectors $|0\rangle, |1\rangle$ are orthogonal base states.

Equation (2.2) can be used to represents pure states of systems of non-relativistic spin $\frac{1}{2}$ particles, in which case $|0\rangle$ and $|1\rangle$ correspond to the eigenstates of the operator σ_z, associated with eigenvalues $+1$ and -1. Here, σ_z is one of the three 2×2 Pauli matrices, the later being related to the spin angular momentum operator of the particle via $\hat{\mathbf{S}} = \frac{\hbar}{2}\boldsymbol{\sigma}$. If $|\psi\rangle$ is normalized then $|\mathrm{c}_1|^2$ and $|\mathrm{c}_2|^2$ give the probability of obtaining $+\frac{\hbar}{2}$ and $-\frac{\hbar}{2}$, respectively, when measuring the spin component along the z direction. States having a spin in an arbitrary direction **a** will be expressed in terms of the two eigenstates of $\boldsymbol{\sigma} \cdot \mathbf{a}$, the projection of the spin operator in the direction of **a**, with eigenvalues $+1$ and -1. The average spin direction corresponds to the expectation value of the Pauli operator. For an optical beam, i.e., a system of spin $\frac{1}{2}$ particles, polarization is defined by $\Lambda = <\boldsymbol{\sigma}> / <\sigma_0>$ where $<\sigma_0>$ corresponds to the beam intensity and σ_0 is the 2×2 unity matrix. Altogether, the quantities $<\sigma_{i=0,1,2,3}>$ form the Stokes parameters.

From a geometric perspective, quantum states are represented as projective rays within the Hilbert space $\mathcal{H}$. In this representation, two states $\psi \in \mathcal{H}$ and $\psi' \in \mathcal{H}$ differing by $\lambda \in \mathbb{C}$ such that $\psi = \lambda\psi$ share the same representation. This can be understood by having the transformation $\psi \to \lambda\psi$ leaving the expectation values of all observables invariant. The state space, also known as projective Hilbert space $\mathcal{HP}$, is the set of all projective rays. The projective Hilbert space of a finite Hilbert space $\mathbb{H} = \mathbb{C}^{\mathrm{n}+1}$ is the complex projective group $\mathbb{C}\mathrm{P}^{\mathrm{n}}$ [123].

The subset of normalized states vectors in $\mathcal{H}$ is of particular interest. In the state space representation, two normalized state vectors ψ and ψ', related by $\psi' = \lambda\psi$, are represented by the same state when λ corresponds to the action of the unitary group $\mathrm{U}(1)$ which preserves the norm of the vector. In other words, ψ and ψ' only differ by an overall *phase factor*. The projective Hilbert space $\mathbb{C}\mathrm{P}^{\mathrm{n}}$ of normalized states vectors is diffeomorphic to $\mathbb{S}^{2\mathrm{n}+1}/\mathbb{S}^1$ [1]. Consequently, for 2-state systems, the state space of normalized vectors can be visualized as a sphere of unit radius $\mathbb{S}^2$ also known as "Bloch sphere", as introduced by F. Bloch in 1946 [124].

[1] A detailed description of projective spaces can be found in the work of Lyre [123]

From an algebraic perspective, the Bloch sphere is obtained from the parametrization of the amplitude coefficients c_1 and c_2 of a pure, normalized state of a two-state system such that:

$$|\psi\rangle = \cos(\theta/2)\,|0\rangle + \exp(i\varphi)\sin(\theta/2)\,|1\rangle \tag{2.3}$$

Where $0 \geq \theta \geq \pi$ and $0 \geq \varphi \geq 2\pi$ are real, arbitrary parameters. This corresponds to the parametrization of a sphere in terms of a polar and a azimuthal angle. A pure state of a two-state system is represented by a point on the surface of the Bloch sphere (see figure (4)). Mutually orthogonal states, such as $|0\rangle$ and $|1\rangle$, correspond to diametrically opposite points on the sphere. The half angle in equation (2.3) is a consequence of having orthogonal states being separated by $\theta = 180°$, not $90°$, on the Bloch sphere.

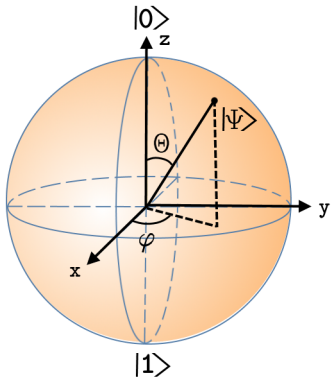

Figure 4 – The Bloch sphere representation of a qubit system. A pure state ψ is represented by a point of polar angle θ and azimuthal angle φ on the surface of the Bloch sphere.

In two-states systems, a unitary operator acting on ψ corresponds to a 2×2 unitary matrix U of the group U(2) and can be written as [121]:

$$\hat{U} = \exp(i\alpha\hat{\mathbf{1}} + i\beta\mathbf{a}\cdot\hat{\boldsymbol{\sigma}}) \tag{2.4}$$

Where α and β are real, $\mathbf{a}$ is a unit vector and $\hat{\boldsymbol{\sigma}}$ is the vector operator formed by the three Pauli matrices. Equation (2.4) can also be expressed as $\hat{U} = \exp(i\alpha)(\cos(\beta)\mathbf{1} + i\sin(\beta)\mathbf{a}\cdot\boldsymbol{\sigma})$ where it appears that α only introduces an arbitrary phase that does not affect the state vector. From a geometric perspective, the vector $\mathbf{a}$ corresponds to an axis passing through the center of the Bloch sphere and 2β describes a *rotation* of the vector representing ψ about that axis.

In physics, pure states typically transform via a temporal evolution, according to the following linear Schrödinger equation:

$$i\hbar\frac{\partial}{\partial t}\,|\psi(t)\rangle = \hat{H}\,|\psi(t)\rangle \tag{2.5}$$

Where $\hat{H}$ is the Hamiltonian of the system. The formal solution to equation (2.5) is $|\psi(t)\rangle = \hat{U}(t)\,|\psi(0)\rangle$ where $\hat{U}$ is a unitary operator, transforming a pure state into a pure state. If the Hamiltonian is time-independent then $\hat{U}(t) = \exp(-iHt/\hbar)$ and the transformation described in equation (2.4) is recovered provided $H \propto \mathbf{a}\cdot\boldsymbol{\sigma}$. Equation (2.4) can also describe a sequence of transformations induced by external elements [121].

So far, we have examined a system of non-relativistic spin $\frac{1}{2}$ particles, let us now examine systems of relativistic spin-1 particles, i.e., photons. Polarized light can be assimilated to a qubit system based on the following observations. In classical physics, the polarization of a monochromatic, paraxial, plane wave propagating in the z-direction is, by convention, defined by the locus of the electric field in the transverse plane. The electric field can be written as the real part of the following 2-component complex electric field vector:

$$\begin{pmatrix} \mathrm{E_x(t)} \\ \mathrm{E_y(t)} \end{pmatrix} = \begin{pmatrix} \mathrm{a} \\ \mathrm{b} \end{pmatrix} \exp(\mathrm{i}\omega_0 \mathrm{t}) \tag{2.6}$$

Where a and b are complex coefficients and where ω_0 is the frequency of the electromagnetic wave. The two-vector (a, b) is known as the Jones vector and $\mathrm{a}{=}|\mathrm{E}_{0x}|\exp(\mathrm{i}\phi_\mathrm{x})$ and $\mathrm{b}{=}|\mathrm{E}_{0x}|\exp(\mathrm{i}\phi_\mathrm{y})$. If the electric field oscillates in the x(y)-direction, the wave is said to be linearly polarized in x (y). When normalized by $|\mathrm{E}_0|$, the Jones vector corresponding to linearly polarized beams in x and y becomes $\left(\begin{smallmatrix} 1 \\ 0 \end{smallmatrix}\right)$ and $\left(\begin{smallmatrix} 0 \\ 1 \end{smallmatrix}\right)$, respectively, which appears to be analogous to the qubit basis vectors $|0\rangle, |1\rangle$. The normalized Jones vectors representing left circular and right circular polarized light are $\frac{1}{\sqrt{2}}\left(\begin{smallmatrix} 1 \\ -i \end{smallmatrix}\right)$ and $\frac{1}{\sqrt{2}}\left(\begin{smallmatrix} 1 \\ i \end{smallmatrix}\right)$, respectively. Still in analogy to qubit systems, an overall phase factor does not affect the polarization of a normalized the Jones vector, i.e., Jones vectors differing only by a global phase are "equivalent". Finally, a superposition of Jones vector yields a Jones vector describing another allowed polarization state.

Assuming fully polarized light, polarization transformations are implemented by 2×2 matrices, known as Jones matrices, acting on the normalized Jones vector [2].

From a geometric perspective, the polarization states of homogeneous electromagnetic waves are represented on the Poincaré sphere (see figure 5). On the surface of the Poincaré sphere, each point represents a polarization state, up to an overall phase factor. In analogy to the Bloch sphere representation, two polarization are defined as orthogonal when they lie on opposite sides on the sphere [121]. By convention, the north pole represents right handed (RH) circularly polarized light and the south pole represents left handed (LH) circularly polarized light, and its equatorial plane represents linearly polarized states. Linearly polarized states correspond to a superposition of equal intensities of LH and RH circularly polarized states. Along the equator, the orientation of the linear polarization state varies accordingly to the relative phase between the LH and RH constituents. The hemisphere surfaces represent elliptically polarized states.

Instead of the Jones vector, the Stokes parameters $\mathrm{S}_1, \mathrm{S}_2, \mathrm{S}_3$ can also be used to map the polarization of a fully polarized electromagnetic wave on the Poincaré sphere [3] [121].

A single x (or y) polarized photon can be associated with the qubit state $|0\rangle$ ($|1\rangle$), turning the Bloch sphere and Poincare spheres equivalent. However, note that both spheres have a different physical interpretation. As highlighted by S. Barnett [121], for two-level quantum

[2] The transformation of coherent, partially polarized or unpolarized light is treated using Mueller matrices.

[3] The Stoke parameter S_0 describes the beam intensity.

systems of spin $\frac{1}{2}$ particles, points on the Bloch sphere represent directions of spin in three dimensional space, i.e, each point on the Bloch sphere is an eigenstate of some (spin) angular momentum operator. Theoretically, spin-1 particles like photons, can have a spin of 1, 0, or -1, however, the transversality condition forbids the zero spin outcome, only the 1 and -1 spin states are allowed. In sum, contrary to the Bloch sphere, only two points on the Poincare sphere represent eigenstates of some spin angular momentum operator, namely, the poles, representing RH and LH circularly polarized light, respectively.

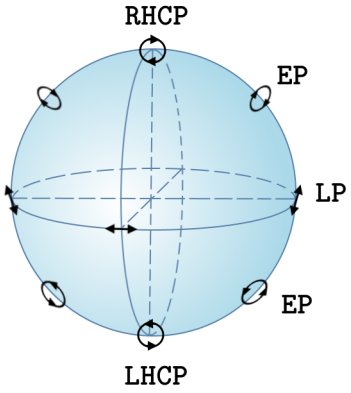

Figure 5 – The Poincaré sphere representation for polarization states. The poles represent right-handed circularly polarized (RHCP) states and left-handed circularly polarized (LHCP) states, respectively. The equator consists of linearly polarized states (LP) of varying orientation and the hemispheres represent elliptically polarized (EP) states.

A sphere analogous to the Bloch sphere has also been proposed to represent orbital angular momentum (OAM) states (see figure 6.a) [125]. In this geometric representation, the poles account for optical vortex modes of opposite, unit topological charge, describing Higher order Laguerre Gauss beams of radial index 0 and azimuthal index $\ell{=}\pm1$. Equally weighted superposition of $\mathrm{LG}_{1,0}$ and $\mathrm{LG}_{-1,0}$ modes, i.e , HG modes, are located at the equator [4]. The relative phase between the LG modes determines the orientation of the HG mode. The mode order of a $\mathrm{LG}_{\mathrm{p}}^{\ell}$ mode, where ℓ is the azimuthal index and p is the radial index, and an $\mathrm{HG}_{\mathrm{nm}}$ mode is $\mathrm{N}{=}2\mathrm{p}{+}|\,\ell|{=}\mathrm{n}+\mathrm{m}$, respectively [126].

Note that the Bloch sphere representation is limited to two-state systems. OAM states can be described by higher order systems, which require higher-order representations [125, 127, 128]. In this case, an algebraic description is preferred.

Similarly, a Bloch sphere has been proposed to represent monochromatic, paraxial, inhomogeneously polarized light beams (see figure 6.b) [129]. In this case, the poles represent circularly polarized vortex beams, which carry both SAM and OAM. The equator represents vector beams which are inhomogeneously linearly polarized and the hemisphere represent elliptically polarized vector vortex beams. For $\ell{=}0$ the Poincaré representation is recovered. For $\ell{\geq}1$ two Bloch sphere, one where the poles represent circularly polarized beams with same handedness and another representing circularly polarized beams of opposite handedness are used to describe inhomogeneously polarized beams. Note that a SO(3) sphere representation, less

[4] HG modes do not carry OAM

known than the one described above but very promising as it allows to represent more general modes, has also be proposed to represent more vector modes [130, 131].

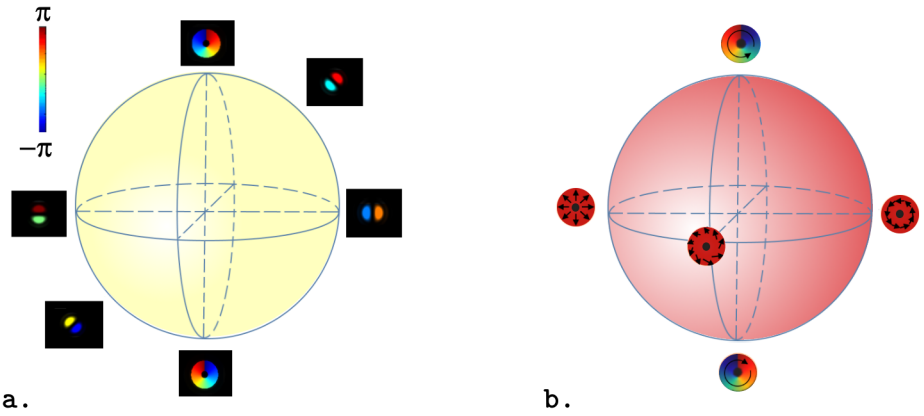

Figure 6 – a. The Bloch sphere representation of OAM states. The poles represent LG beams of opposite unit topological charge and the equator represents HG modes. b. One of the two possible Bloch sphere representation for inhomogeneously polarized beams. The poles represent circularly polarized optical vortex beams of opposite unit topological charge and the equator represents vector beams, from left to right: radially polarized vector beams, a general vector beam and an azimuthally polarized vector beam.

In all of the above, paraxial fields propagating a in a fixed direction were considered. The electric field therefore essentially lies in the wave transverse plane (2D field).

In the last decades, macroscopic SOI of light have been increasingly interpreted in terms of geometric phases, which are acquired by the wave function upon specific transformations of the beam parameters or (and) its inner states. For this reason, prior to reviewing major SOI phenomena, one final concept, namely, the one of geometric phase, needs to be introduced.

2.1.2 Introduction to geometric phases

The concept of geometric phase was anticipated as early as 1956 [132] but it is M. Berry, in 1984, who gave a complete description of the phenomenon by showing that a quantum system undergoing a cyclic evolution acquires a so-called geometric phase, which can be seen as a "memory" of the evolution of the system [133]. M. Berry's work was soon generalized to other systems [134–136] and was given a mathematical interpretation by Simon, in 1983, who identified a geometric phase as the anholonomy [5] of a fibre bundle [137].

Fibre bundle theory is an elegant mathematical framework which underlines the geometrical and topological nature of geometric phases. It not only applicable to Optical systems but also to a large variety of physical systems such as classical and molecular dynamics, quantum dynamics and solid state physics. A few technical terms issued from fibre bundle theory are now frequently used in the context of Optics, such as the connection and its curvature. For these reasons, I will introduce geometric phases within the fibre bundle formalism. Due to the complexity of the topic, an informal description will be used. A more rigorous description of

[5] The term holonomy is also often used, however, it does not emphasize the non-integrability property of a given constrain. M. Berry commented on this terminology as "a reversal of usage I consider a barbarism." [132].

fibre bundle theory can be found in the works of E. Malek [138], A. Wilczek and F. Shapere [22], T. D. Stanescu [139] and N. Mukunda and R. Simon [140].

In mathematics, a smooth fibre bundle consists of the following elements $(\mathrm{E}, \Pi, \mathrm{B}, \mathrm{F}, \mathcal{G})$. E and B are two differentiable manifolds called the *total space* and the *base space*, respectively. $\Pi{:}\mathrm{E}\to\mathrm{B}$ is the *projection*, a map relating the total space to the base space. The inverse image of a point p in the base space defines a differentiable manifold called a *fibre* $\mathrm{F}_\mathrm{p}=\Pi^{-1}(\mathrm{p})$. $\mathcal{G}$ is a group of diffeomorphisms of F called the *structure group*. In physics, particularly relevant fibre bundles include *vector fibre bundles*, whose fibre is a vector space and $\mathcal{G}$ acts as a linear map, and *principal bundles*, whose fibre is the structure group $\mathcal{G}$ [138]. Fibre bundles can be "*trivial*" or "*non-trivial*". A trivial fibre bundle is globally diffeomorphic to $\mathrm{B}\times\mathrm{F}$ whereas a non-trivial fibre bundle only locally appear like a product of two manifolds (see figure (7)). Non-trivial fibre bundles are defined using several local products $\{\mathrm{U}_\alpha\times\mathrm{F}\}$, with $\{\mathrm{U}_\alpha\}$ being open coverings of B, i.e, small neighbourhoods of p.

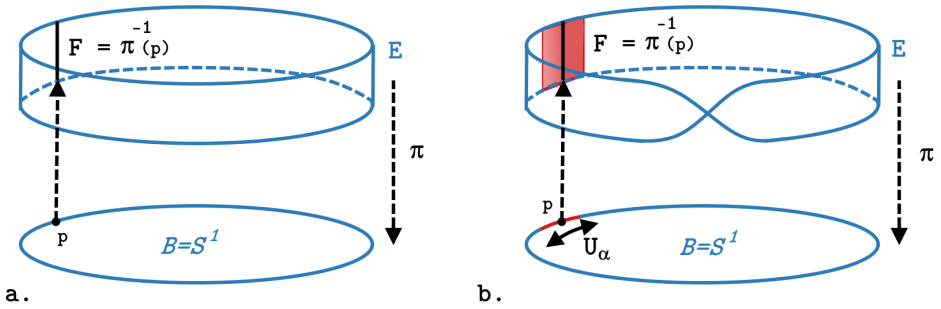

Figure 7 – Examples of trivial and non-trivial fibre bundles: a. A cylinder fibre bundle and b. A Möbius strip fibre bundle. Both fibre bundles possess a circle base space $\mathrm{B}=\mathrm{S}^1$ and fibres consisting of line segments (0,1). The cylinder fibre bundle is trivial: its total space E can be written as $\mathrm{B}\times\mathrm{F}$. The Möbius strip is non-trivial, the twist prevents $\mathrm{B}\times\mathrm{F}$ to be defined globally.

Continuing with some terminology, a *section* is a continuous map $\sigma{:}\mathrm{B}\to\mathrm{E}$ which can be viewed as the "inverse" of the projection map. The pair $(\mathrm{U}_\alpha, \phi_\alpha)$ with $\phi_\alpha=\Pi^{-1}(\mathrm{U}_\alpha)\to\mathrm{U}_\alpha\times\mathrm{F}$ is called a *local trivialization* of E over U_α. Local trivializations are "glued" together by continuous maps called *transition functions* such that $\mathrm{t}_{\alpha,\beta}{:}\mathrm{U}_\alpha\cap\mathrm{U}_\beta\to\mathcal{G}$ [138].

Returning to the definition of geometric phase as the anholonomy of a fibre bundle, the concept of anholonomy can be introduced rather intuitively by considering an example of S. Ganguli, namely, a deformable body constrained to rotate about some point [141].

In this case, the base space B is defined by parametrizing all possible body shapes with coordinates. A point $\mathrm{p}\in\mathrm{B}$ thus labels a specific shape. For each shape, the orientation of the object is specified using three orthogonal axes fixed to the object. The axis are mapped via a 3×3 rotation matrix to a frame in which the body is constrained to rotate. The set of all orientations presents a one to one correspondence with the points of the Lie group $\mathrm{SO}(3)$. Considering all possible shapes, the total space of all configurations E is a principal $\mathrm{SO}(3)$ fibre bundle. Locally, choosing a set of axis for p is subject to gauge freedom and corresponds to

choosing a section of E. Globally, the section cannot always be chosen continuously, in which case gauge transformations are used to relate different gauges.

If the body undergoes a cycle of deformations, successive deformations trace a closed path γ in the base space B. This path is *lifted* to form a path in the total space E, which projects back to γ. This lift is specified by the *connection* on the principal fibre bundle, which assigns to each tangent vector indicating the direction of an infinitesimal displacement on γ for each $\mathrm{p}\in\mathrm{B}$, an element of the Lie algebra $\mathfrak{g}$ in a linear fashion. In other words, the connection relates each infinitesimal displacement (shape change) in B to an infinitesimal displacement in the fibre coordinate Lie group G, i.e., an infinitesimal rotation (see figure 8). At the end of a cycle of deformation, the body recovers its initial shape but does not necessarily recovers its initial orientation, i.e., a net rotation (translation of the fibre coordinate) is observed. Generally, the initial and final points of the lifted path lies in the same fibre and are related by an element of G: the *anholonomy* of the connection around the loop γ. This result is independent of the choice of gauge. The net rotation is calculated via a path-ordered integration of all infinitesimal rotations.

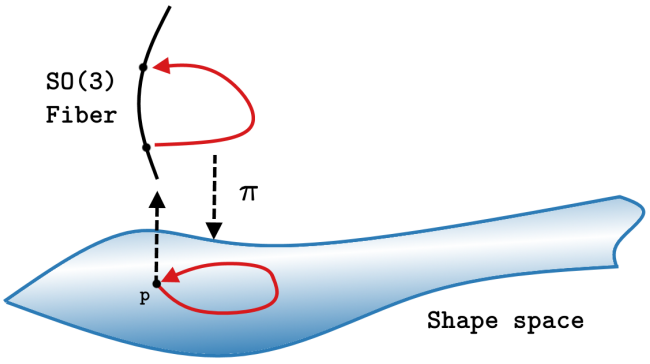

Figure 8 – The path corresponding to a cycle of deformations is lifted to a path in the total space of the fibre bundle, which can be projected back to the base space. While in the base space the closed path starts and end at the same point p, the lifted path ends on the same fibre above p but does not return to its initial point. The translation in the fibre defines an anholonomy, i.e., net rotation. Figure adapted from the work of S. Ganguli [141]

From a practical perspective, the anholonomy described above allows cats falling from an upside down position, to rotate and land on their paws after a sequence of deformations [6].

Anholonomies of connections giving a rule to parallel-transport vectors tangent to the base space are particularly relevant in physics. Continuing from a classical perspective, we shall now distinguish anholonomies issued from parallel transport of vectors on a curved space from anholonomies issued from parallel transport on a space with non-trivial topology.

Let be an orthogonal triad $\mathbf{r}$, $\mathbf{e}$, $\mathbf{e}^{'}=\mathbf{r}\times\mathbf{e}$, as illustrated on figure (9), with the vectors $\mathbf{e}$ and $\mathbf{e}^{'}$ forming a basis to define the complex unit vector $\psi=(\mathbf{e}+\mathrm{i}\mathbf{e}^{'})/\sqrt{2}$. The connection defines the parallel transport law determining how vectors tangent to the sphere of unit radius vector $\mathbf{r}$ are moved to other points on the sphere. For the unit vector $\mathbf{e}$, parallel transport implies

[6] Rigorously, the cat should be considered as a pair of rolling cylinders, a more detailed description can be found in the work of R. Montgomery [142].

that, upon varying the unit radius vector $\mathbf{r}$, $\mathbf{e}\cdot\mathbf{r}=0$ and the orthogonal triad containing $\mathbf{e}$ and $\mathbf{r}$ does not twist. For ψ, this is equivalent to requiring $\mathrm{Im}\psi^*\cdot\psi=0\equiv\mathrm{Im}\psi^*\cdot d\psi=0$ with $d\psi$ being a variation of ψ resulting from a variation $d\mathbf{r}$. After a cyclic variation of the parameter $\mathbf{r}$ driving the evolution of ψ on the sphere surface, the vector ψ has traced a closed path on the sphere surface like the one illustrated on figure (10). While $\mathbf{r}$ recovers its initial orientation, ψ may not. The net rotation corresponds to the anholonomy of the connection around the circuit C.

The net rotation angle $\alpha(C)$ of ψ is determined by choosing a local basis of unit vectors $\mathbf{u}(\mathbf{r}),\mathbf{v}(\mathbf{r})$. The choice of local basis is subject to gauge freedom. This basis defines a complex unit vector $\mathbf{n}(\mathbf{r})\equiv(u(r)+iv(r))/\sqrt{2}$ at each position on the sphere such that $\psi=\exp(-i\alpha)\mathbf{n}$. The net rotation corresponds to the line integral of the connection [22]

$$\alpha(C)=\oint d\alpha=\mathrm{Im}\oint n^*\times dn=\mathrm{Im}\iint_{\partial S=C} dn^*\cdot dn \tag{2.7}$$

This result is independent of the choice of gauge. Stokes' theorem has been applied to obtain the last term of equation (2.7), allowing the anholonomy to be expressed as an integral over the area on the sphere bounded by the circuit C followed by ψ. For arbitrary parameters X_1, X_2 labelling the position on the sphere we can write [22]:

$$\alpha(C)=\mathrm{Im}\iint_{\partial S=C} dX_1 dX_2(\partial_1 n^*\cdot\partial_2 n-\partial_2 n^*\cdot\partial_1 n) \tag{2.8}$$

If $\mathbf{u}(\mathbf{r})$ and $\mathbf{v}(\mathbf{r})$ lie along the parallel of latitude θ and meridian of longitude ϕ at $\mathbf{r}=(\sin\theta\cos\phi,-\cos\theta\sin\phi,\sin\theta)$ and for $X_1=\theta$ and $X_2=\phi$, the integrand reduces to $d\theta d\phi\sin\theta$. In other words, $\alpha(C)$ is equal to the solid angle subtended by C at the sphere center.

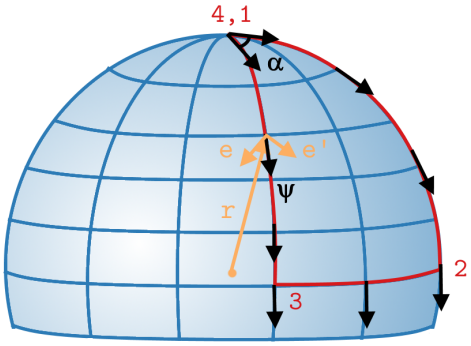

Figure 9 – Geometrical anholonomy (net rotation α) of the complex unit vector ψ, represented by a black arrow, formed upon parallel transport on the sphere of unit radius $\mathbf{r}$, following a path represented in red in the order 1,2,3,4.

The anholonomy described by equation (2.7) is path dependent and does not depend on the time the vector took to follow that path. Circuits subtended by the same solid angle $\Omega(C)$ will yield the same geometric phase [7].

The covariant derivative described in equation (2.8) corresponds to the curvature of the connection, which better illustrates the relation of the connection with the underlying space properties. In the case described above, the connection is non flat, reflecting the fact that the underlying space is curved. Because the connection reflects the geometric properties

[7] A discussion on circuits yielding the same geometric phase can be found in the work of J. W. Zwanziger [143].

of the underlying space, the associated net rotation acquired by ψ is a geometric anholonomy. Connections with a non-zero curvature describe non-trivial fibre bundles [123].

In their review, A. Shapere and F. Wilczek evidence how anholonomies are related to the spatial properties by showing how, in general relativity, the anholonomy observed when an initial frame is parallel transported around a closed loop in space-time fails to coincide with the final frame, is related to the local curvature of spacetime, i.e, to the Riemann tensor [22].

An example of net rotation acquired upon parallel transport on a sphere can be observed in the Pantheon in Paris, where a Foucault pendulum is installed. After following a closed path on the surface of an imaginary sphere, formed as the Earth performs one revolution, the pendulum oscillation direction is rotated with respect to its initial oscillation direction [144]. Note, however, that if the pendulum were located at a lower latitude, following a path on the equator of the imaginary sphere, no net rotation would be observed. Indeed, this special path is a geodesic. Geodesics are formed at the intersection of a plane passing by the sphere center and the sphere surface. Geometric phases cannot be acquired along a *single* geodesic. The path formed along a parallel and the path illustrated on figure (9) consists of a concatenation of several geodesics and are associated a non-zero solid angle at the sphere center leading to the formation of an anholonomy.

Let us now consider a fibre bundle which underlying space is flat but possess non-trivial topological features. Let be a vector, tangent to the surface of a Möbius strip, transported along the strip surface, as illustrated on figure (10)).

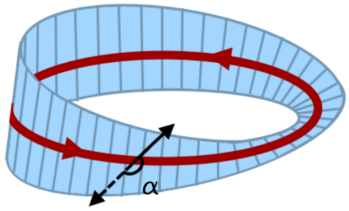

Figure 10 – Topological anholonomy (net rotation α) of the complex unit vector ψ, represented by a black arrow, formed upon parallel transport on the surface a Möbius strip, following a path represented in red.

After one circuit, the vector direction is inverted, and recovers its initial direction afters another circuit, i.e, two discrete anholonomies are possible, depending on the number of turns [123]. In this case the anholonomy is of topological nature, reflecting the properties of the underlying space and the fibre bundle is also non-trivial.

In sum, anholonomies are determined by the line integral of the connection along the path traced in the base space. It is from the connection, which gives a rule to relate each infinitesimal displacement in the fibre bundle base space to a displacement in the corresponding fibre coordinate, that the anholonomy acquires its geometric or topological nature, as the connection reflects the geometric properties of the underlying space.

So far, we have studied classical geometric phases. We shall now consider physical

quantum systems. In analogy to parallel transport of the unit vector ψ on the sphere of unit radius described on figure (9), parallel transport of a state $|\psi\rangle$ can be carried out by considering that the Hamiltonian of the system depends on some parameters X which vary adiabatically.

In the *parameter space*, at each position $\mathrm{X}=(\mathrm{X}_1, \mathrm{X}_2, ...)$, a quantum state $|\psi\rangle$ is represented, modulo a phase factor. Adiabaticity is a sufficient but not necessary condition to ensure that when tracing a circuit in the parameter space, a state, initially in an eigenstate of $\hat{\mathrm{H}}(\mathrm{X}(\mathrm{t}))$, remains in an eigenstate of $\hat{\mathrm{H}}(\mathrm{X}(\mathrm{t}))$ during the whole evolution. In other words, at each position X, a unique state, solution of the non-degenerate eigenstate equation $\hat{\mathrm{H}}(\mathrm{X})\,|\psi_{\mathrm{n,X}}\rangle = \mathrm{E_n}(\mathrm{X})\,|\psi_{\mathrm{n,X}}\rangle$, is assigned, in relation to which the phase of the quantum state can be defined [133]. This is analogous to choosing **n(r)** in the classical case. The initial state $|\psi_{\mathrm{n,X}}\rangle\,(0)$ and a later state $\exp(\mathrm{i}\gamma_{\mathrm{n(t)}})\,|\psi_{\mathrm{n,X}}\rangle\,(t)$ will only differ by a phase factor, i.e, a complex number of unit modulus which is also an element of the unitary group $\mathrm{U}(1)$. The total phase γ acquired upon a cyclic, adiabatic evolution of X can be evaluated by using $\left|\psi'_{n,\mathrm{X}}\right\rangle(t) = e^{i\gamma_n(\mathrm{t})}\,|\psi_{\mathrm{n,X}}\rangle\,(\mathrm{t})$ in the time-dependent Schrödinger equation and projecting into $\left|\psi'_{\mathrm{n,X}}\right\rangle(\mathrm{t})$ such that [123]:

$$\frac{\mathrm{d}}{\mathrm{dt}}\gamma_{\mathrm{n}}(\mathrm{t}) = \mathrm{i}\,\langle\psi_{\mathrm{n,X}}|\nabla_{\mathrm{X}}\psi_{\mathrm{n,X}}\rangle\,\frac{\mathrm{d}}{\mathrm{dt}}\mathrm{X}(\mathrm{t}) - \frac{1}{\hbar}\mathrm{E_n} \tag{2.9}$$

After integrating over t, γ_{n} comprises a dynamic and a geometric contribution [123]:

$$\gamma_{\mathrm{n,d}}(\mathrm{t}) = -\frac{1}{\hbar}\int \mathrm{E_n}(\mathrm{t})\mathrm{dt} \quad \gamma_{\mathrm{n,g}}(\mathrm{C}) = \mathrm{i}\oint_{\mathrm{C}}\langle\psi_{\mathrm{n,X}}|\nabla_{\mathrm{X}}\psi_{\mathrm{n,X}}\rangle\,\mathrm{dX} \tag{2.10}$$

This is the result obtained by Berry for a cyclic, adiabatic, evolution of non-degenerate, pure quantum states [133]. The geometric phase corresponds to the line integral of the connection along the path formed in the parameter space. A normalized eigenstate ensures that $\gamma(C)$ is real.

In Berry's approach, X parametrized a part of the projective Hilbert space corresponding to the $\mathrm{n^{th}}$ eigenstate of the family of Hamiltonians $\mathrm{H}(\mathrm{X})$[22]. Parallel transport can be achieved using the parameters X to label the state, not the Hamiltonian, in the projective Hilbert space accounting for all quantum states. This refers to state spaces such as the ones described at the beginning of this chapter. This is the approach Aharonov and Anandan undertook to provide a more general interpretation of the geometric phase without having to rely on the adiabatic condition [145]. In this case, the geometric phase depends on the path traced in the *state space*.

In the state space, states differing by an overall phase share the same representation. A fibre-bundle structure allows to track the geometric phase acquired upon the state transformation. The quantum bundle consists of a principal U(1)-fibre bundle over the projective Hilbert Space. In this representation, two Hilbert space vectors differing by a phase belong to the same fibre. The horizontal lift of a closed curve in the projective Hilbert space such that $|\phi(0)\rangle = |\phi(\mathrm{T})\rangle$ and $|\varphi\rangle = \exp(\mathrm{ig(t)})\,|\phi\rangle$ yields, according the condition given by the connection $\langle\varphi|\dot{\varphi}\rangle = 0$, where

$|\dot{\varphi}\rangle$ represents a vector tangent to the corresponding curve, upon temporal integration [8][123]:

$$\gamma = \mathrm{g(T)} - \mathrm{g(0)} = \mathrm{i} \oint_0^T \left\langle \phi \middle| \dot{\phi} \right\rangle \mathrm{dt} \tag{2.11}$$

This anholonomy corresponds to Berry's geometric phase. The phase is independent of the rate at which the evolution has occurred and origins from the curvature of the quantum bundle.

The notion of geometric phase was subsequently extended to non-cyclic evolutions by J. Samuel and R. Bhandari [134]. Geometric phases were also evidenced in the context of mixed states [135, 147] and F. Wilczek and A. Zee investigated geometric phases issued from the adiabatic transport of a degenerate set of quantum states [136].

For degenerate quantum states, the system does not need to return to the original eigenstate via the same degenerate state while retaining the same state space. The accumulated phase factor of an N-fold degenerate level is described by a U(N) matrix. In this case, the connection is "non-Abelian" and path ordering is necessary when integrating over infinitesimal phase changes, as the integrands for the geometric phase in equation (2.10) does not commute with itself at different points on the circuit. Also, note that, in this case, it is generally not possible to use Stoke's theorem to express the anholonomy in terms of a simple gauge invariant quantity such as the solid angle subtended by the circuit [143].

Now that the concept of geometric phase has been introduced for general quantum systems, optical systems can be studied and the role of geometric phase in SOI of light described.

2.2 Angular momentum conversion, a geometric perspective

In the above, it was shown that geometric phases only depend on the path traced on the space describing the transformation, i.e., parameter space or state space. In what follows I will demonstrate how geometric phases and their respective fibre bundle are involved in SOI of light. Following Berry's approach, geometric phases issued from path traced in the parameter space of light will first be studied, followed by a more general description of geometric phases issued from paths formed in the state space describing the fundamental properties of light. Dynamical effects attributed to the connection of the corresponding fibre bundle will be reviewed last.

2.2.1 An optical counterpart for the Berry phase

Historically, Berry's findings were first applied to describe the behaviour of a spin $\frac{1}{2}$ particle in an eigenstate of a magnetic field **B** of constant magnitude in a direction **a** with spin eigenvalue s as the direction of the magnetic field is adiabatically cycled [133]. The parameter space under consideration is a sphere forming the space of directions of the magnetic field. The Hamiltonian of the system can be written as a function of $\mathbf{a} \cdot \boldsymbol{\sigma}$, which, from a geometric perspective, can be associated with a rotation transformation of the type of equation (2.4). The

[8] Further demonstrations and discussions can be found in the work of A. Bohm [146] and Lyre [123].

geometric phase associated with this evolution corresponds to the line integral of the connection A determining the parallel transport rule along the circuit C traced in the parameter space and is equal to $-\mathrm{s}\Omega(\mathrm{C})$. Where $\Omega(\mathrm{C})$ is the solid angle subtended at the sphere center $\mathbf{a}=0$ and s is the spin component along B. Here and in what follows the solid angle is taken positive for a clockwise path and negative for a counter-clockwise path.

From a physical perspective, the connection in this case plays the role of a magnetic vector potential acting in real space and its curvature is analogous to a magnetic field originating from a magnetic monopole [9] of strength "$-\mathrm{s}$" located at the origin of the parameter space, where $\mathbf{a}=0$. From a mathematical perspective, a monopole is the result of a degeneracy of the eigenvalues of a Hermitian 2×2 matrix [143].

A vector potential is not only a convenient mathematical tool to define the electric and magnetic fields in classical physics but also leads to physical effects, namely the apparition of a phase factor, in quantum physics. A collection of papers giving examples of geometric phases found in physical quantum systems is presented in the book of A. Shapere and F. Wilczek [22].

The optical counterpart of the system described above is obtained by considering a circularly polarized light beam, of spin eigenvalue ± 1 along the propagation direction, and adiabatically varying the beam wavevector **k**. This was realized by R. Y Chiao and Y. S. Wu [148] and by A. Tomita and R. Y. Chiao [149] for a light beam in a linearly polarized state, i.e., a superposition of left and right handed circular states, propagating in a helical monomode fibre. The left and right circularly polarized components acquire a spin-dependent geometric phase $-\mathrm{s}\Omega(\mathrm{C})$, determined by the solid angle subtended by the circuit C in the parameter space, i.e., in the sphere of directions. The phase difference between the two circularly polarized states leads to a rotation of the linearly polarized state orientation while maintaining the beam eccentricity. This evolution can be described as a product of rotations in the parameter space [150].

The experiments of R. Y. Chiao and Y. S. Wu and A. Tomita and R. Y. Chiao followed from the discoveries by V. V. Vladimirskii and S. M. Rytov. S. M. Rytov investigated how the vectorial nature of electromagnetic waves could be accounted for when light is refracted in an inhomogeneous media. He showed, using a semi-classical formalism, that the transport law for the directions **e** and **h** of the electric and magnetic fields, respectively, consists of a parallel transport law of the orthogonal triad **e**, **h**, **k**, where **k** is the ray direction [151]. V. V. Vladimirskii showed that S. M. Rytov's law is nonintegrable, i.e., leads to the apparition of a geometric phase, and he showed that the rotation angle observed when polarized light wave follows a curved trajectory in a inhomogeneous media is related to the solid angle formed in the parameter space [152] [10]. For these reasons, the spin-dependent geometric phase acquired upon variations of the

[9] The magnetic monopole, called Hopf fibre bundle by mathematicians, is an interesting case study, which brings discussions about the discontinuity of the gauge potential and the quantization of Berry's curvature [22].

[10] This analysis cannot be directly applied to the experiments of R. Y. Chiao and Y. S. Wu and A. Tomita and R. Y Chiao, which featured thin monomode fibres. Geometrical optics are not suited to describe such problem but

beam wavevector direction is also known as Rytov-Vladimirskii phase.

Let us consider the triad **w**, **v** and **k**, where **w**, **v** form local basis defining the 2-dimensional electric vector **e** of a paraxial field. Maxwell's tranversality condition for free electromagnetic fields couples the field electric vector to the beam wavevector **k**. Variations of the beam wavevector thus lead to the parallel transport of the 2-dimensional vector **e**, tangent to the sphere of directions (**k**-sphere). The anholonomy caused by parallel transport of **e** has a classical origin in the sense that it arises from the coupling between the wavevector and its polarization, defined in the beam transverse plane, according to Maxwell's equations [153].

Adiabatic, cyclic variations of the beam mean wavevector can be obtained upon propagation in a gradient-index medium, as described in the work of K. Bliokh [20]. In this case, the phase acquired by the field electric vector, tangent to the local mean wavevector direction **k**, is determined using the local basis **v**, **w** in the tangent plane (see figure (11) a.). The author consider the evolution of the polarization vector along a curved beam trajectory. Figure (11 b.) illustrates this evolution in momentum space [11]. A connection, defining the parallel transport of the transverse electric vector **e** upon adiabatic variations of the momentum vector on the unit **k**-sphere, is defined, yielding, upon line integration, the geometric phase associated with the rotation of the electric field vector.

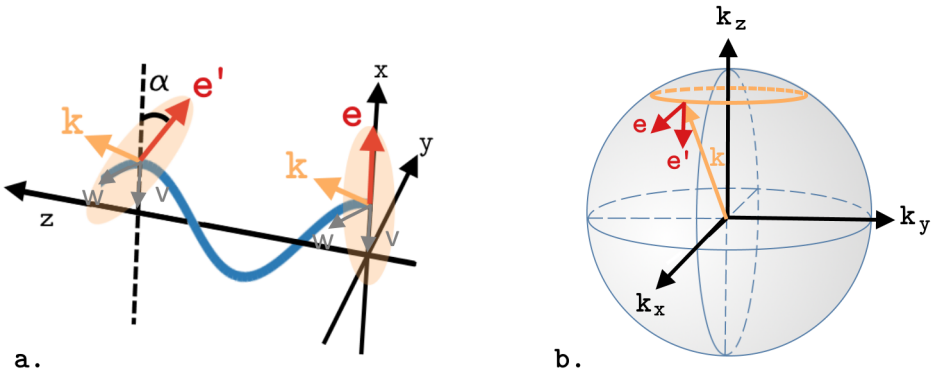

Figure 11 – a. Rotation of the beam polarization vector **e** defined in the plane transverse to the local wavevector as the beam follows a helical trajectory b. As the beam follows a helical trajectory, the beam wavevector traces a closed path on the parameter space (**k**-sphere). The solid angle associated with the closed path in parameter space is equal to α. Figure adapted from the work of K. Y. Bliokh [20]

The connection can also be interpreted as a gauge field and its curvature as the field strength, playing the role of an effective 'magnetic field' issued from a monopole located at the origin of the momentum space, with helicity playing the role of the monopole charge [20]. This interpretation has dynamical consequences that we shall further discuss at the end of this chapter.

In 2006, K. Bliokh introduced the connection associated with the eigenvalue ℓ, which gives a rule to parallel transport the structure of a monochromatic, paraxial beam propagating

rather "the full Maxwell equations, either in a modal analysis or, when recast as a Schrodinger-type spinor equation, to enable immediate application of the spin-1 geometric phase formula" [132]

[11] The projection on a unit sphere is possible as the polarization only depends on the direction of the momentum vector $\mathbf{k}/\mathrm{k}$ [20].

in a smoothly inhomogeneous isotropic medium along a curved trajectory [21]. Neglecting diffraction effects, he derived the connection driving the parallel transport of a field carrying both SAM and OAM. He found that, in addition to the spin-related Abelian connection, a second connection, related to the beam topological charge ℓ, could be identified. The total geometric phase $\oint_{\mathrm{C}} \mathrm{A}^{'}\mathrm{d}\mathbf{k}$, for a cyclic evolution of the beam wavevector forming a closed path in the $\mathbf{k}$-sphere, is equal to $-(\mathrm{s}+\ell)\Omega$ where Ω is the solid angle subtended by the circuit C. K. Bliokh concluded that, similarly to the parallel transport of the polarization vector, the so-called orbital Berry phase causes the rotation of the field transverse intensity distribution. This phenomenon should entail the rotation of a Hermite-Gaussian mode, i.e., a combination of Laguerre Gauss modes, upon propagation following a helical trajectory [21].

As a side note, when it comes to polarization and image rotation, one distinguishes pure rotators from pseudo-rotators. Following the definition of E. J. Galvez et al. [154], a pure rotator "rotates by an amount that is independent of the orientation of the input" whereas the rotation, for pseudo-rotator does depend on the input orientation.

Continuing with wavevector variations, a geometric phase can also be attributed to abrupt (non-adiabatic) variations of the beam wavevector. Such variations are typically caused upon reflections such as mirror reflections or total internal reflections. A RH circularly polarized paraxial beam, propagating along the z-direction, reflected by a perfect electric mirror at normal incidence, sees both its $\mathrm{E_x}$ and $\mathrm{E_y}$ field components undergo a π phase shift. The wavevector propagation direction is reverted and the spin pseudo-vector conserved. The helicity (projection of the spin pseudo-vector upon the propagation direction), is inverted and the beam becomes LH circularly polarized [155]. To study the geometric phase introduced by mirror reflection, M. Kitano et al. introduced modified $\mathbf{k}$ vectors $\tilde{\mathbf{k}}=(-1)^i\,\mathbf{k}_i$, according to which the photon helicity is conserved [156]. In this case, points on the $\tilde{\mathbf{k}}$-sphere describing successive reflections are connected by geodesics to form a closed path, which can be associated with a geometric phase similar to the adiabatic case. Optical systems featuring an even (odd) number of reflections where the input and the output beams are parallel (anti-parallel) can be considered as pure rotators [157]. In the case of polarization rotation, the beam ellipticity must be conserved. Therefore, when designing a polarization rotator, care must be taken for the s and p polarization components of light, the component perpendicular and parallel to the plane of incidence, respectively, not to acquire different phase shifts, which would modify the beam ellipticity.

A beam carrying OAM can be rotated using an image rotator such as a Dove prism, or any optical element carrying out a phase-shifting operation. This transformation will also be associated with a geometric phase traced on the parameter space [157, 158].

So far, I have described evolutions of the beam mean wavevector in the parameter space, which maintain the weight of the corresponding mode superposition, i.e., the mode ellipticity for polarization and the overall phase distribution for OAM modes. A geometric

phase was associated with the closed path formed in parameter space, which can be s or ℓ dependent. This introduces a phase difference between the RH and LG circularly polarized states and between Laguerre-Gauss modes of topological charge $\ell{=}{+}1$ and $\ell{=}{-}1$, leading to the rotation of the linearly polarized beam and of the Hermite-Gauss profile, respectively.

Such transformation can also be described in the corresponding state space, i.e., the Poincaré sphere and Bloch sphere for polarization and for OAM. For an elliptically polarized beam following a helical trajectory, such that the phase difference between the circular polarization components cause the polarization ellipse to undergo a full rotation, the polarization transformation will form a closed path on the Poincaré sphere as illustrated on figure (12) [20].

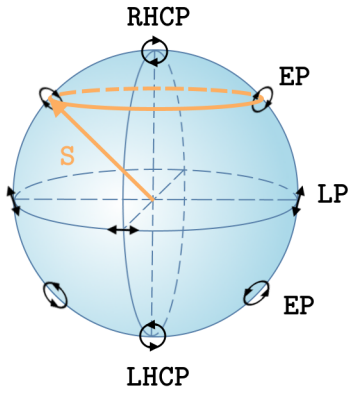

Figure 12 – Variations of the beam Stokes vector **S** tracing a closed path on the Poincaré sphere due to the introduction of a phase difference between orthogonal polarization states as the beam follows an helical trajectory. In this case, the solid angle formed in the state space is equal to 2α, where α is the rotation of the electric vector after one cycle, as illustrated on figure (11). Figure adapted from the work of K. Bliokh [20]

Alternatively, mode rotation can be achieved without varying the beam mean wavevector by using optical elements slowly transforming the beam polarization state, such as optically active materials or half waveplates. These elements are examples of pure and pseudo rotators, respectively. Of course, optical elements can achieve more general transformations than simply rotating the beam polarization state. In what follows, geometric phases acquired upon general state transformations, described within the state space, will be presented. Their role in SOI of light will also be evidenced. At first, the beam mean wavevector is assumed to be fixed. More complex transformations, combining variations of the beam wavevector and general transformations of the beam polarization state will also be described.

2.2.2 State space transformations of light

In 1956, S. Pancharatnam studied geometric phases associated with transformations of polarization states of light. On the Poincaré sphere, a closed path can be associated with a geometric phase, called Pancharatnam-Berry phase, equal to $-\frac{1}{2}\mathrm{s}\Omega(C)$, where $\mathrm{s}{=}{\pm}1$ and where $\Omega(\mathrm{C})$ is the solid angle subtended at the sphere center [159]. The $\frac{1}{2}$ factor is due to the difference in representation of orthogonality condition in the Poincaré sphere and in real space. Naturally, a different geometric phase will be attributed to closed path forming different solid angles.

A closed path can be formed on the Poincaré sphere by making an optical beam go through a succession of optical elements transforming the polarization state via unitary transformations, bringing a point A, representing the initial polarization state, to other points on the sphere and back to A along a concatenations of geodesics.

In the case a state A does not return to its original state on the Poincaré sphere, i.e., for an open path, a rule is needed to compare the initial and final state. This rule was given by S. Pancharatnam, who provided a criterion to determine the total (geometric+dynamical) phase carried by a beam of light, without the overall phase ambiguity. He defined two light waves in different polarization states as "in phase" when their superposition yields a maximum intensity [160]. From a quantum perspective, the intensity resulting from the superposition of two monochromatic waves in polarization state $|\psi_1\rangle$ and $|\psi_2\rangle$, respectively, is given by [134]:

$$||\psi_1\rangle + |\psi_2\rangle|^2 = \langle\psi_1|\psi_1\rangle + \langle\psi_2|\psi_2\rangle + 2\mathrm{Re}(\langle\psi_1|\psi_2\rangle) \tag{2.12}$$

Which modulus is maximum when $\langle\psi_1|\psi_2\rangle$ is real and positive. In the polar form, $\langle\psi_1|\psi_2\rangle$ becomes $\rho\exp(i\alpha)$ with $\rho > 0$ and where α is the phase difference between the two waves. The interference pattern of two polarized waves allows to measure the relative phase difference between the two waves, except when the two polarization states are orthogonal. Two waves in orthogonal polarization states do not interfere as the phase difference is undefined [161]. Optics being the playground of quantum mechanics, note that a classical system can be described by a quantum system, in virtue of coherence and orthogonality between degrees of freedom of light [162]. In terms of geometric phases of light, both classical and quantum perspective have been explored, as discussed in the work of N. Mukunda et al. [163] and C. E. R. Souza, et al. [131].

Pancharatnam's criterion implies the existence of a "Pancharatnam connection", which provides a rule to compare phases between any states, provided they are not orthogonal. J. Samuel and R. Bhandari argued that this connection can be seen as a generalization of Berry's connection, which only relates neighbour states and that, in the case the two states $|1\rangle$ and $|2\rangle$ being neighbouring rays, the Pancharatnam connection reduces to the usual bundle connection [134]. Using the Pancharatnam connection, J. Samuel and R. Bhandari studied how to associate a geometric phase to an open path on the Poincaré sphere, when the initial and final states are not orthogonal. They found that, assuming no dynamical phase is involved, the phase difference between the initial state A and the final state B, is the geometric phase given by half of the solid angle enclosed by the path taking A to B, then B back to A along a geodesic [134].

On the Poincaré sphere, an opened path can be formed when a circularly polarized beam is transmitted by a retarder, i.e., a birefringent linear waveplate of retardation δ, which fast axis forms an angle β with the x axis, as illustrated on figure(13). From an algebraic perspective, the action of the wave plate on the polarization state is represented by a 2×2 unitary matrix $U(\beta)$. From a geometric perspective, a waveplate brings, on the Poincaré sphere, the point A, representing the initial polarization state, via a rotation about a fixed axis passing through

the sphere center and a point Q of azimuth 2β on the equator, to another polarization state, represented by a point P, through the angle δ. This transformation is illustrated on figure (14) for a half-wave plate ($\delta = \pi$) for a waveplate orientation axis of $\beta = 0$ (path A,B,C,D,P) and of β (path A, B', C', D', P) [164].

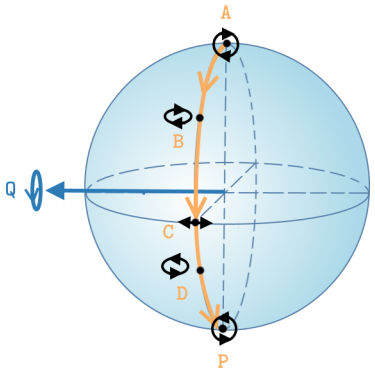

Figure 13 – An opened path on the Poincaré sphere, issued from polarization transformations of a circularly polarized beam transmitted by a retarder, here a half-waveplate of optical axis orientations β. On the Poincaré sphere, such polarization transformation can be described by a rotation around the axis denoted by Q on the figure.

As stated above, a closed path can be formed if we interfere the final state B with a reference state, linearly polarized along x. The relative phase between these two waves is the phase of the complex number $\langle x|\, U(\beta)\, |x\rangle$. From a geometric perspective, interfering the two waves consists of bringing P back to A along the shorter geodesic on the Poincaré sphere. This transformation is analogous to the action of a polarizer, blocking the state orthogonal to A [165]. Indeed, in equation (2.12), α can be seen as the phase difference between a wave in an initial state $|\psi_2\rangle$ which has passed through on optical element letting only $|\psi\rangle_2$ pass, with a reference wave in state $|\psi_2\rangle$. Generally, the phase acquired by a system undergoing several projections bringing an initial state $|\psi_1\rangle$ back to itself consists of the phase of $\langle\psi_1|\psi_n\rangle\,\langle\psi_n|\psi_{n-1}\rangle\,...\,\langle\psi_3|\psi_2\rangle\,\langle\psi_2|\psi_1\rangle$[165]. The relative phase difference between the wave in the final state P and the reference wave in a polarization state A, if the dynamical phase cancels out, consists of the geometric phase associated with the so-formed closed path.

The difference between retarders, such as waveplates (or media with optical activity) and polarizers, is that the former introduces unitary transformations of the polarization state while the later causes non-unitary transformations. Ideal absorbing polarizers do not introduce geometric phase, i.e., they project one polarization state onto another following a geodesic [12].

As a small digression, note that, in the above, polarization operators have been described in terms of rotation operators $\exp(-i\delta/2\mathbf{p}\cdot\boldsymbol{\sigma})$. In a review of J. Lages et al., such rotation operators appear as a special case of the $\mathrm{SL}(2,\mathbb{C})$ group operator $\exp((\gamma\mathbf{p}_1 - i\delta\mathbf{p}_2)\cdot\boldsymbol{\sigma}/2)$ where γ and δ are real and $\mathbf{p}_1, \mathbf{p}_2$ are unit vectors associated with the two polarization states in

[12] Total reflection based polarizers or realistic polarizers, such as dichroic polarizers can introduce non-trivial geometric phases [166]

consideration. Another particular case of this general operator is the boost operator $\exp(\gamma/2\mathbf{p}\cdot\boldsymbol{\sigma})$ [166]. Consequently, geometric phases issued from boost transformation have also been studied, evidencing non-trivial SAM to OAM conversion [167, 168].

Coming back to our study of an open path on the Poincaré sphere, a very interesting case, described by J. Samuel and R. Bhandari, is what happens to the geometric phase when interfering nearly orthogonal states. In the parameter space spanned by δ and β, as the waveplate retardation and its fast axis orientation get close to the $\delta=180°, \beta=45°$ point, the shortest geodesic curve linking A to P switches abruptly. This corresponds to a sweeping of area equal to 2π on the Poincaré sphere, causing an abrupt phase change of $|\pi|$ in real space [165]. In the parameter space, the singular point $(\delta=180°, \beta=45°)$ corresponds to where $\langle x|\,\mathrm{U}\,|x\rangle=0$. In the case of two-states systems, the singularity is a point, around which the total phase change for a circuit enclosing the singular point is $\pm2\pi$ (singularity strength ±1), which corresponds to a real phase shift of $\pm\pi$ as the state space is a sphere. N-state systems evolving under $\mathrm{SU(N)}$ transformations can feature singularities of higher strength.

Appendix 1 presents a short numerical study on the orthogonality condition in inhomogeneously polarized paraxial optical beams. The study is carried out by accompanying the visibility of the corresponding interference fringes. As expected, orthogonal states, defined in agreement with the state geometric representation illustrated on figure (6), do not interfere.

It is possible to dynamically track the phase difference between two waves by recording changes in the interference pattern as the phase, the geometric phase in our interest, of one beam is varied through optical elements. If the fast axis of the half waveplate rotates at a uniform angular velocity, the waveplate will impose a linear phase shift in time, i.e., a frequency shift equal to twice the angular frequency of the half waveplate rotation. This effect has been experimentally demonstrated by B. A. Garetz and S. Arnold [169].

Through polarization transformations, a gradient of Pancharatnam-Berry (PB) phases can be used to impart a helical phase distribution to a beam of light. This was notably achieved by Z. Bomzon et al. in 2001, who, inspired by the work of R. Bhandari [165], produced a space-variant PB phase distribution using a metallic subwavelength grating [170]. Due to manufacturing limitations, the device only operated in the mid-infrared regime. In 2006, L. Marrucci et al. proposed to generate a spatial gradient of Pancharatnam-Berry phases using an anisotropic inhomogeneous media. They developed an optical element which could operate in the visible regime, namely a "q-plate", using patterned liquid crystal cells [171].

A q-plate is a slab of birefringent material of uniform phase retardation δ, behaving like a half-wave plate. What allows a q-plate to impart a gradient of geometric phase is its optical axis, varying linearly with the azimuthal coordinate in the transverse plane. Together, the local polarization transformations form several geodesics sharing the same initial and final states, associated with a varying solid angle, as illustrated on figure (14) for two optical axis

orientations of the q-plate. The plate possess a central directional singularity, of topological charge q, indicating the number of rotations that the optical axis performs in a path circling the singularity. If we define the plate azimuthally varying optical axis as $\beta = \beta_0 + q\varphi$, where β_0 is a reference angle, the phase gradient is such that an helical wavefront is imparted, with a central phase singularity of topological charge $\ell = 2\sigma q$ [172].

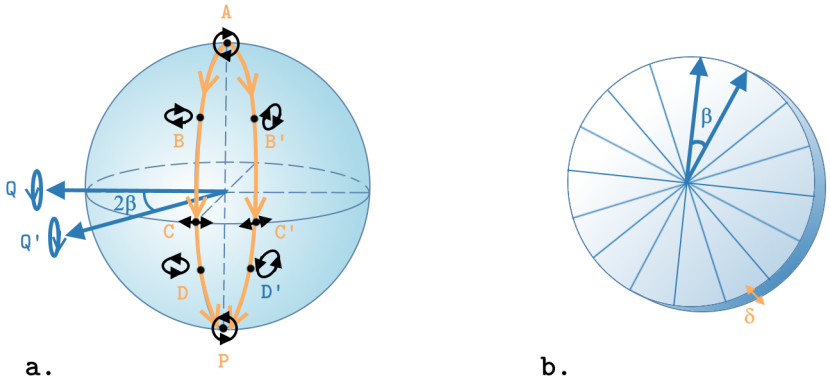

Figure 14 – Polarization transformations for two different optical axis orientations β in the transverse plane of a q-plate of retardation δ, represented on the Poincaré sphere. a. A solid angle, i.e., a Pancharatnam Berry phase, can be associated with a pair of geodesic corresponding the polarization transformation for two different optical axis and the same retardation b. Simplistic representation of a q-plate, of azimuthally varying optical axis and uniform retardation. Two optical axis of different orientation separated by an angle β, corresponding to the polarization transformations represented in a. are emphasized.

Assuming a z-propagating beam and a q-plate which rotational symmetry axis is the z-axis, the z-component of the total AM is conserved, i.e., there is no net transfer of angular momentum to matter, and SAM is efficiently converted into IOAM. This corresponds to SOI of light, interpreted in terms of a gradient of PB phases.

The development of metasurfaces has allowed to create highly compact space-variant PB elements for SAM to IOAM conversion. Optical elements manipulating the beam polarization to introduce a space-variant Pancharatnam–Berry phase are also known as Pancharatnam–Berry optical elements (PBOE). A large variety of PBOE elements exist and cannot be all reviewed here, and excellent description of PBOE elements, which also discuss more general applications for PB phase can be found in the review of E. J. Galvez [173].

Appendix 2 presents a short numerical study on SAM to IOAM conversion based on a PB phase gradient produced by a circular air nanoslit embedded in thin metal film on a glass substrate, which acts as an optical retarder with variable orientation axis. Our results are in agreement with the work of P. Chimento et al. [174].

Instead of using birefringent elements to modify the beam polarization state, total internal reflection (TIR) can also be used to create a gradient of PB phases. Upon TIR, the components of the electric fields lying in the plane parallel and perpendicular to the plane of incidence, known as p and s components, can acquire different phase shifts, causing a transformation of the beam polarization state.

In 2012, M. Mansuripur et al. studied SOI of light in retro-reflective elements involving two reflections [175]. In this work, numerical simulations show that a circularly polarized beam undergoing two consecutive reflections in a perfect electric conductor cone of 90° apex angle retains its helicity, reverses its SAM and picks up twice as much IOAM to conserve total angular momentum along the cone symmetry axis. The same cone made of transparent material can be designed to impart different mixture of SAM and OAM. The reason the beam acquires a gradient of PB phase is the twist in the s-p orientation around the cone, which is similar to the rotation of the birefringent axis in q-plate. This was notably experimentally verified in 2016 by N. Radwell et al, who confirmed that retro-reflection from a glass cone of apex angle 90° does generate a gradient of PB phase leading to SAM to IOAM conversion. Interestingly, the authors also showed that using linearly polarized light as the incident beam lead to the formation of a beam with inhomogeneous polarization distribution, carrying polarization singularities [176].

Another device based on TIR to obtain a gradient of PB phases was realized by F. Bouchard et al. in 2014, using a pair of Fresnel rhombs of revolution, i.e., two hollow axicons glued together [177]. Fresnel rhombs rely on two successive TIR to introduce a $\pi/2$ phase difference between orthogonal polarization components. An incident linearly polarized beam, oriented at 45° will thus become circularly polarized. A combination of two Fresnel rhomb therefore behaves as a half-wave plate and, similarly to the case of the cone, the cylindrical geometry will lead to the generation of a gradient of PB phases. This entails SAM to IOAM conversion, the amount of IOAM acquired being $|\ell|=2$. This is yet another example of SOI of light. If instead of a circularly polarized beam, a linearly polarized beam is incident upon the glued axicons, a vector beam, i.e., a beam which transverse distribution consist of linearly polarized light with varying orientation, is generated [177].

So far we have considered only geometric phases issued from polarization state transformations, described on the Poincaré sphere. In 1993, S. J. Van Enk proposed that a geometric phase could also arise from cyclic mode transformations of paraxial optical beams carrying orbital angular momentum [178]. This type of geometric phases was measured by E. J. Galvez et al. in 2003 for first-order modes, in the visible [179]. In this paper, OAM modes were transformed using pairs of cylindrical lenses. A $\pi/2$ mode converter based on a pair cylindrical lens can convert a $\mathrm{LG}_{0,1}$ mode into a $\mathrm{HG}_{1,0}$ mode and vice versa, while a π mode converter based on a pair of cylindrical lens can convert a $\mathrm{LG}_{0,1}$ mode to a $\mathrm{LG}_{0,-1}$ mode and vice versa. Consequently, the $\pi/2$ and the π cylindrical lens mode converters are analogous to the quarter-wave and half-wave plates used to transform polarization states. By using a succession of two π mode converters, a $\mathrm{LG}_{0,1}$ beam of unit topological charge can be brought along a closed path on the Bloch sphere of OAM states of unit topological charge. Similarly to the PB geometric phase, the geometric phase described by transformation of the OAM mode is proportional to minus half the solid angle subtended at the center of the Bloch sphere representing OAM states. Transformations of higher-than-one modes have, to my knowledge, yet to be investigated. In this

case, an algebraic description is preferable.

Similarly to the case of a rotating waveplate, if the π-mode converter rotates the OAM mode at a uniform angular velocity, the mode converter will impose a linear phase shift in time, i.e., a frequency shift. This was notably evidenced by J. Courtial et al. in 1998 [158].

Regarding beams with inhomogeneous polarization distribution, G. Milione et al. argued that higher-order PB phases could also be generated from transformations carried out on the higher order Poincaré spheres. The authors argued that a circularly polarized optical vortex beams could be carried along a geodesic from north to the south pole of the sphere and back, using half wave plates in combination with cylindrical lens mode converter [180].

A Matrix formulation accounting for both SAM and OAM general transformations have been proposed by L. Allen, J. Courtial and M. J. Padgett in 1999 [181].

In all of the above, only transformations of paraxial beams have been considered. In an unpublished work dated from March 2019, K. Y. Bliokh, M. A. Alonso and M. R. Dennis proposed to study geometric phases in generic non-paraxial beams [182]. They also emphasised the role of polarization singularities in PB geometric phases in paraxial beams. The authors first define the geometric phase as the difference between the total phase and the dynamical phase for general vector fields. Then, for two-dimensional fields, the authors distinguish paths enclosing the C point polarization singularity in real space, i.e., enclosing the S_3 axis on the Poincaré sphere, from the ones which do not. Path that do not enclose the singularity will have a uniquely defined PB phase, equal to half of the solid angle on the Poincaré sphere. However, if the closed path encloses a C-point, the singularity causes the geometric phase to experience a $\pm\pi$ jump in real space. This complements the observations of R. Bhandari [165]. K. Y. Bliokh, M. A. Alonso and M. R. Dennis propose a modified expression for the geometric phase to evidence the role of the singularity. This formulation allows to account for the presence of several polarization singularities in inhomogeneously polarized field when examining the PB phase.

Regarding three-dimensional fields, K. Y. Bliokh, M. A. Alonso and M. R. Dennis argue that such field should exhibit properties corresponding to spin-1 waves with three component wavefunctions [182]. So far, very few studies have explored geometric phases in general three-level and spin-1 quantum systems [183, 184]. As pointed out by the authors, attempts to unify the PB phase and the Rytov-Vladimirskii phase are sparse [185] and have mostly relied on the geometric Majorana sphere representation developed by Hannay [186, 187] or have relied on a Coriolis effect interpretation for waves carrying SAM [188]. However, neither approach clearly identifies the geometric and dynamical phase acquired along a given spatial contour in a generic 3D complex vector field. The authors further argue that while the Majorana sphere does unify the redirectionng phase and the PB phases, it does not incorporate the notion of normalization of the polarization ellipse. K. Y. Bliokh, M. A. Alonso and M. R. Dennis therefore propose to solve this issue using a so-called "Poincarana sphere" describing 3D polarized fields. The author then

characterize the geometric associated with a path on the Poincarana sphere, taking into account polarization singularities in 3D polarized fields [182].

Continuing with recent investigations on geometric phases of light, a work of 2018 by A. Karnieli and A. Arie proposed to obtain an adiabatic geometric phase for light via nonlinear interactions. Instead of considering light polarization through its two complex amplitudes at two orthogonal directions, they consider an additional degree of freedom, which they call "the spectral polarization". In this case, one would consider the complex amplitudes at two different optical frequencies, coupled by the medium nonlinearity [189].

Prior to studying the dynamical consequences associated with the connection and its curvature, I would like to highlight a few more works concerned with non-trivial transformations of light combining both wavevector variations and polarization transformations.

In 2016, L. B. Ma et al. numerically studied the evolution of linearly polarized light in asymmetric micro-cavities [190]. The authors first studied the geometric phase acquired in a Möbius strip geometry, leading to mode rotation. This configuration is particularly interesting as the electric field evolution is lead by the geometry topological properties. Variations of this geometry allow the passage from an adiabatic to a non-adiabatic transport of the electric field, as evidenced by J. Kreismann and M. Hentschel in a numerical study from 2018 [191]. L. B. Ma et al. then designed a cone-shaped microtube resonator and added anisotropy effects. In this case, the combined effect of the wavevector evolution and anisotropy cause the electric field vector to change in orientation and eccentricity.

In 2011, K. Bliokh et al. [192] studied the transformation of a paraxial field to a non-paraxial field. The author consider variations of the individual wavevectors constituting the field Fourier spectrum. A paraxial, circularly polarized, helical, monochromatic electromagnetic field of topological charge ℓ propagating in the z direction is focused by a high-numerical aperture lens. Initially, the beam carries a total angular momentum of $\sigma + \ell$ along the longitudinal (z) direction. The non-paraxial beam obtained upon focusing can be seen as a Fourier-spectrum, made of circularly polarized plane waves, which wavevectors form a cone with an opening angle θ in the **k**-sphere representation. A geometric phase can be attributed to the azimuthal distribution of wavevector in the beam spectrum. In short, the conical **k** distribution can be seen as the result of a rotation, imposed by the lens, of the wavevector of the incident beam in the meridional plane, as illustrated on figure (15). This evolution features rotations of the local polarization vector, issued from parallel transport on the **k**-sphere from the north pole $\theta = 0$ (incident field) to $\theta \neq 0$ (focused field) where θ corresponds to the lens aperture angle.

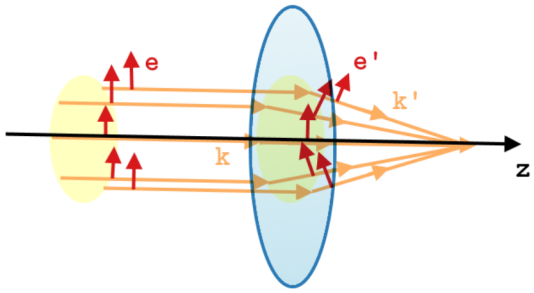

Figure 15 – Evolution of individual wavevector component of a paraxial electromagnetic field, when focused by a high aperture lens. The beam electric field acquires a non-negligible longitudinal component upon focusing, turning the beam non-paraxial. Figure adapted from the work of K. Bliokh et al.[192].

This transformation preserves the beam total angular momentum along the beam axis of symmetry (z). Upon focusing, SAM to IOAM conversion occur. The total SAM and IAOM along the longitudinal direction can be written as [192]

$$<\mathrm{L_z}>=\ell+\sigma\overline{\Phi}_\mathrm{B}, \quad \text{and} \quad <\mathrm{S_z}>=\sigma(1-\overline{\Phi_\mathrm{B}}) \quad \text{with} \quad \overline{\Phi}=(1-\cos\overline{\theta}) \tag{2.13}$$

The $\sigma\overline{\Phi}_\mathrm{B}$ component in $<\mathrm{L_z}>$ corresponds to the part of SAM that has been converted into IOAM. In equation (2.13), $\cos(\overline{\theta})$ characterizes the field directional spread. The Berry phase associated with the azimuthal distribution of partial rays with a fixed polar angle θ is $\gamma(\theta)=2\pi\Phi_\mathrm{B}=\oint_\mathrm{C}(1-\cos(\theta))\mathrm{d}\phi=2\pi(1-\cos(\theta))$, which is related to a circuit on the **k**-sphere. For an aperture angle $\theta=\pi/2$, SAM is fully converted to IOAM. SAM to IOAM conversion can be evidenced by studying the corresponding optical forces exerted on a small particle [193].

In the same work, non-paraxial beams obtained from strong scattering by a small particle is also studied [192]. The authors examine spherical redirectioning of partial plane waves and demonstrate SAM to OAM conversion. However, the geometric transformation used to obtain the scattered field is not entirely equivalent to the transformation describing focusing, as it involve projections rather than parallel transport [192].

The transformation of a paraxial beam into a non-paraxial beam therefore evidences SOI of light, as SAM is converted into IOAM. The geometric phase associated with this transformation is related to the distribution of local wavevectors in the parameter space. It would be interesting to further examine this transformation in terms of the Poincarana sphere.

Now that the role of geometric phases in SOI of light has been described, I will briefly discuss how the curvature of the connection of the fibre bundle associated with the geometric phase can also cause dynamical effects, namely, spin or orbital-dependent trajectory changes.

2.2.3 Dynamical effects associated with the quantum fibre bundle

In 1879, 18 years before the discovery of the electron and its spin, E. Hall noted that applying a magnetic field perpendicularly to an electrical conductor carrying an electric current leads to the apparition of a voltage difference across an electrical conductor [194]. This effect, known as Hall effect, describes charge-dependent trajectory deviations of electrons

attributed to the Lorentz force. A few years later, E. Hall noted that the effect could be amplified in ferromagnetic materials, where the voltage difference can be attributed to spin-dependent deflections of the electrons [195]. This phenomenon can interpreted in terms of the Berry phase and the Berry curvature in momentum-space, which introduce an anomalous contribution to the wave-packet group velocity, as described in the review of N. Nagaosa et al. [196]. These spin-dependent deflections are similarly observed in nonmagnetic materials, indicating that the corresponding Spin Hall effect exists without the necessity of applying a magnetic field. Further investigations have revealed a complete family of electronic Hall effects such as quantum Hall effects and the valley Hall effect [197].

The spin Hall effect (SHE) of light was predicted in 1992 by V. S. Liberman and B. Y. Zel'dovich [198], and was theoretically described by K. Bliokh and Y. Bliokh [199] and M. Onoda, S. Murakami and N. Nagaosa [200]. Optical Hall effects appear as a consequence of SOI of light and are deeply involved in angular momentum conservation processes.

SHE of light can be witnessed in a gradient-index media, in which case it is also known as optical Magnus effect [201]. This phenomenon is fully described in a review from 2008, K. Y. Bliokh, A. Niv and E. Hasman, in which the dynamic effect of Berry's curvature on the beam centroid is evidenced [20]. Assuming a smooth inhomogeneous medium, the authors examine the propagation of vector waves following an helical trajectory and derive the Lagrangian of the system, evidencing a "spin-orbit coupling Lagrangian" contribution. The coupling Lagrangian is considered as "the Coriolis term in a wave-accompanying non-inertial coordinate frame" and is expressed in terms of the Berry connection determining the parallel transport of the transverse electric field on the unit $\mathbf{k}$-sphere. The Euler-Lagrange equations then gives the equations of motion (ray equation) describing the evolution of the centroid of a polarized wave packet in an inhomogeneous medium, which are the first order approximation of geometrical optics. The equations of motions comprise a "force" equation $\partial_t \mathbf{k}$ and a velocity equation $\partial_t \mathbf{r}$. The author evidence a spin-dependent correction term in the velocity equation, which is absent in the zero-order approximation, forming a so-called "anomalous velocity equation". This contribution entails a polarization-dependent transverse deflection of the ray trajectory, orthogonal to both the wave momentum and the medium inhomogeneity gradient. Consequently, a linearly polarized beam propagating in an inhomogeneous medium along a helical trajectory, i.e., a superposition of RH and LH circularly polarised components, will experience beam splitting between its RH circularly polarized beam and a LH circularly polarized components, as illustrated on figure (16).

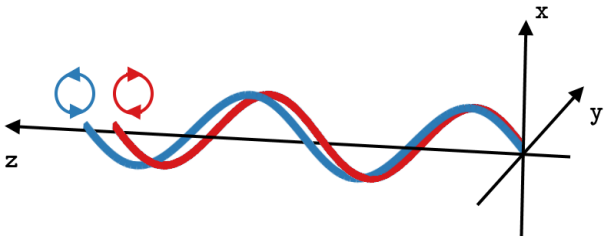

Figure 16 – Schematic spin splitting of an electromagnetic beam propagating along an helical trajectory in a smooth inhomogeneous media. Figure adapted from the work of K. Bliokh [20].

The anomalous velocity equation can be written in terms of the curvature of the Berry potential vector, which yields a "Lorentz force" originating from a topological (magnetic) monopole located at the origin of the parameter space (**k**-sphere). In a spherically symmetric medium, the spin-orbit term in the equations of motion also allows the wave total angular momentum to be conserved, as variations in the direction of SAM caused by refraction are compensated by the ray transverse shift, which changes the beam OAM.

In a theoretical study from 2006, K. Bliokh introduced Hall effects related to the "Orbital" Berry connection, manifesting as ℓ-dependent trajectory changes, when studying an OAM-carrying beam propagating in a smoothly inhomogeneous isotropic medium [21]. He showed that, similarly to the curvature of the spin Berry connection, the curvature associated with the orbital Berry connection introduces a correction term in the velocity equation in real space. In the same paper, it is showed that, in an inhomogeneous media, the velocity equation exhibits both spin and orbital-dependent corrections, giving rise to spin and ℓ dependent ray deflections. Hall deflections are generally small, of magnitude proportional to the wavelength but can grow with the ray length and are perpendicular to the medium inhomogeneity $\Delta \mathrm{n}$. Unlike the helicity, the topological charge ℓ is not bounded to $|1|$, thus, the orbital Hall effect (OHE) can be of higher magnitude than the SHE. In an inhomogeneous media, the orbital Hall effect manifests as deflections, or splitting of singularity lines for a superposition of optical vortices.

Optical Hall effects can also manifest at the sharp interface between two media of different refractive indices. In this case, the trajectory change cannot be directly interpreted in terms of the Berry phase, as it is a non-adiabatic case. A complete description of optical Hall effects at sharp interfaces was provided by V. G. Fedoseyev in 2011 [23] and in a review of K. Y. Bliokh, I. V. Shadrivov and Y. S. Kivshar from 2009 [202]. By considering a beam of finite spatial extend as a superposition of plane waves propagating at slightly different angles, it appears that each individual wave experiences different Snell and Fresnel equations, which describe the reflection and transmission laws. Consequently, the output beam experiences displacements from its geometric expectation, within and across the propagation plane, which describe the Goos-Hänchen (GH) [203] and transverse Imbert-Ferodov (IF) shifts [204, 205], respectively. From a geometric perspective, it can be argued that it is the geometric phase gradient formed in the **k**-space as the different wavevector components of the beam rotate to satisfy Maxwell's

transversality condition, which entails the real-space spin Hall shift of the beam centroid in real space [206, 207]. In this process, the amount of SAM in the normal direction change and is compensated by the beam shift which creates a nonzero EOAM. The spatial shift induced by the gradient of geometric phase can be accompanied by a transverse angular (momentum) shift, which increases with the propagation distance, i.e., it is a diffraction phenomenon [208].

V. G. Fedoseyev theoretically predicted vortex-dependent transverse shifts of the centroid at a sharp optical interface [23], the underlying phenomenon being orbit-orbit interactions. As the intrinsic OAM component in the normal direction changes at the interface, total angular momentum is conserved due to the apparition fo a transverse shift introducing EOAM [209–211]. This shift is accompanied by significant transverse deformation of the beam profiles [212–214].

Spin Hall effect of light is difficult to observe as the corresponding displacements occur on the wavelength scale. For this reason, techniques such as quantum weak measurement technology [215] are preferable to measure SHE. Also, SHE can be amplified via multiple reflections, as it is the case in a cylinder glass [20, 216]. For further information about SHE please refer to the review of from 2017 [197].

So far we have described Hall effects due to geometric phases described in the $\mathbf{k}$-space of parameters. In a paper from 2015, Z. Ling et al. have proposed a SHE due to a gradient of PB phase in a dielectric-based metamaterial [217]. In this case, the authors argue that the magnitude of the SHE is significantly bigger than the one observed at a sharp interface as the shift occurs in momentum space ($\Delta\mathbf{k}$), then entails a real space shift $\Delta\mathbf{r}$.

Optical Hall effects can also be introduced by breaking the axial symmetry of a beam when considering the beam distribution in a tilted plane with respect to the beam propagation direction. This effect has been described by A. Aiello et al. in 2009 [24]. Indeed, a beam carrying SAM or IOAM, sees, in a tilted cross section, its angular spectrum components acquire different effective polarization/orbital ‘rotations’ in the parameter space, leading to the apparition of a gradient of Rytov-Vladimirskii geometric phases phase causing a so-called "geometric Hall effects". It has been argued that the geometric SHE can be interpreted in terms of the relativistic Hall effect for relativistic objects [168, 218, 219]. The geometric Hall effect has recently been used to investigate Hall effects in inhomogeneously polarized beams [220], in which case the SHE is attributed to a varying Pancharatnam-Berry geometric phase.

In non-paraxial beams, the geometric phase gradient in the $\mathbf{k}$ space described by each plane waves constituents causes enhanced Hall effects [15]. Optical Hall effects of light have also been investigated in plasmon mediated light-matter interaction [188, 221, 222], and in various systems, such as in a left-handed material [223], and dipole radiation [224], to cite a few.

To sum up Chapter 2, it has been shown that specific transformations of light beams, lead by variations of the mean beam wavevector or (and) caused by variations described in the beam state space, such as the Poincaré sphere or Bloch sphere for OAM modes, can be associated with geometric phases of different nature, obtained from the transport law of the scalar or vector field. This transport laws are embedded in Maxwell's equations, which define the transversality condition between the beam local wavevector and the electric field. Geometric phases are examples of anholonomies of the connection of a specific fibre bundle, and are related to the underlying spatial and topological properties of the system. Macroscopic SOI of light can be interpreted in terms of geometric phases. The curvature of the connection associated with the corresponding fibre bundle has dynamical effects on the beam centroid equation of motion, leading to spin or orbit deflections, i.e., partial SAM or IOAM to EOAM conversion.

Now that a theoretical framework for SOI of light has been established, two original case studies will be presented, both are concerned with orbit-orbit interactions in asymmetric optical beams. In the first case, an azimuthally symmetric beam undergoes wavefront splitting when incident upon a Fresnel Biprism. In the second case, an azimuthally symmetric beam propagates in a medium with a vertical gradient of refractive index.

INVESTIGATING ORBIT-ORBIT INTERACTIONS UPON SYMMETRY BREAKING

The study of orbit-orbit interactions is quite recent in comparison to the study of spin-orbit interactions. May it be in the form of IOAM to IOAM conversion or IOAM to EOAM conversion, the study of orbit-orbit interactions is fundamental to improve our understanding of the scalar properties of light. A simple approach to disclose orbit-orbit interactions of light is to break the symmetry of an initial azimuthally symmetric beam of light. In what follows, two original studies dedicated to orbit-orbit interactions of light are presented, the first one performs symmetry breaking in a freely propagating beam based on a Fresnel biprism, the second one performs symmetry breaking by imposing a vertical gradient of refractive index to a beam propagating in a solution of distilled water and ethanol. In both cases, experimental and numerical results are presented.

3.1 Wavefront splitting based on a Fresnel Biprism

3.1.1 Motivation

Optical Hall effects have mainly been explored at sharp interfaces [209] and in smooth inhomogeneous media [20], in which case they manifest as spin or orbit-dependent transverse spatial shifts and transverse angular shifts [208]. Hall effects can also occur in freely propagating beams, an example being the geometric Hall effect, which is based on symmetry breaking, when observing a beam in a tilted plane with respect to the beam propagation direction [24]. Continuing with Hall effects observed in freely propagating beams, in 2010, K. Bliokh et al. reported optical spin and orbit-dependent transverse shifts in azimuthally truncated non-paraxial fields upon asymmetric focusing [15]. Other studies from 2014 and 2015 have taken interest in the apparition of spin Hall effects upon symmetry breaking of an incident, freely propagating, azimuthally symmetric CV beam [225, 226].

Few works have been dedicated to orbital Hall effects (OHEs) upon symmetry breaking for a freely propagating beam. In March 2017, A. Bekshaev et al. studied the behaviour of beams carrying optical vortices upon edge diffraction [227]. They evidenced some spectacular effects such as optical vortex (OV) migration in the transverse plane upon propagation, OV restoration and the asymmetric penetration of light energy into the screened region upon propagation, which was interpreted in terms of energy flows. This study showed that initial OV cores that are not 'screened' experience transverse trajectory shifts, also, an initial beam with topological charge ℓ is decomposed into a set of secondary single-charged vortices. Upon diffraction, the OV cores move along intricate spiral-like trajectories. Various topological reactions accompanying the OV cores migrations were reported, such as the apparition of new OVs or OVs annihilation.

In a second paper published in July 2017, A. Bekshaev continued his study on freely-propagating paraxial, edge-diffracted beams, this time investigating Hall effects [228]. In this case, the incident beam was circularly polarized and polarisation-dependent angular deviations, parallel to the screen edge, were reported [1]. In the same work, A. Y. Bekshaev argued that, in this case, orbital Hall effects in scalar diffracted beams can be evidenced similarly to SHE effects by considering the trajectory of the beam centre of gravity. He considered an incident Laguerre-Gaussian beam with radial index zero and topological charge ℓ and, in an analytical study, anticipated angular deviations of the diffracted beam trajectory parallel to the screen edge and proportional to the incident OV topological charge. The author considered several screening situations, ranging from weak diffraction perturbation to severe screening.

It is in this context that, in 2017, we decided to experimentally investigate OHE in an asymetric OV beam. Contrary to the edge-diffraction method where the information of the blocked beam is lost, we rely on a Fresnel-Biprism configuration, allowing to split the wave front of a beam incident on the Fresnel Biprism along the vertical direction. Two complementary beam parts of variable proportions are obtained, each having its own propagation direction. We analyse the behaviour of each beam part upon propagation. This work lead to a publication, attached in **Appendix 3**.

Orbit-orbit interactions of light were investigated both using an experimental and a numerical approach. Both are described in what follow.

3.1.2 Generation, characterization and splitting of a Laguerre-Gauss beam

Our light source is a GaN Fabry-Perot laser diode of wavelength 405 nm and typical power 6 mW, coupled to a monomode fibre. A linear polariser, placed after the fibre collimator, ensures that the so-obtained freely propagating beam is homogeneously polarized. A telescope is used to expand and collimate our beam. A collimated Gaussian beam of waist radius $\mathrm{w}_0{=}430\mu\mathrm{m}$ at half of its maximum intensity is obtained [2].

OAM is imparted to our Gaussian beam by using a phase-only spatial light modulator (SLM) (Cambridge Correlators, SDE1280) operating in reflective mode. The SLM relies on nematic liquid crystals to spatially modulate the incident beam in two dimensions. Liquid crystals are birefringent rod-like molecules, which have properties that correspond to both liquid and solid states of matter. An excellent review on phase-only liquid crystal on silicon devices can be found in the work of Z. Zhang, Z. You and D. Chu. [229]. Our SLM is electrically addressed. The addressing circuit is placed on top of a silicon backplane, which is mirror coated to improve the diffraction efficiency of the SLM. The pixels array possesses a resolution of 1280×720, pixel pitch $9.5\mu\mathrm{m}$, pixel $0.5''$ diagonal active area and response time $10\mathrm{ms} \pm 5\mathrm{ms}$. The response

[1] The author employs a paraxial description despite the paraxiality violation of the configuration as the paraxial approach provides "good qualitative and, in many cases, satisfactory quantitative description".

[2] The beam waist is measured with a CCD camera.

time is generally limited by the response time of the liquid crystal. A layer of liquid crystals is placed above the pixel array, on top of which a transparent glass substrate is positioned, as illustrated on figure (17. a.).

In the absence of electric potential, the liquid crystals are horizontally aligned, this corresponds to the off-state illustrated on (17. b). When an electric field is applied across the liquid crystal layer i.e., on-state, controlled pixel by pixel, the liquid crystals reorient themselves. SLMs based on liquid crystals are sensitive to polarization state of the incident beam. For the SLM not to modify the beam polarization state, the incident beam must be aligned with the crystal orientation in the off-state. If the polarization direction of the incident beam is not aligned with the direction of the liquid crystal molecules, the polarization state of the reflected beam will be modified in relation to the incident state.

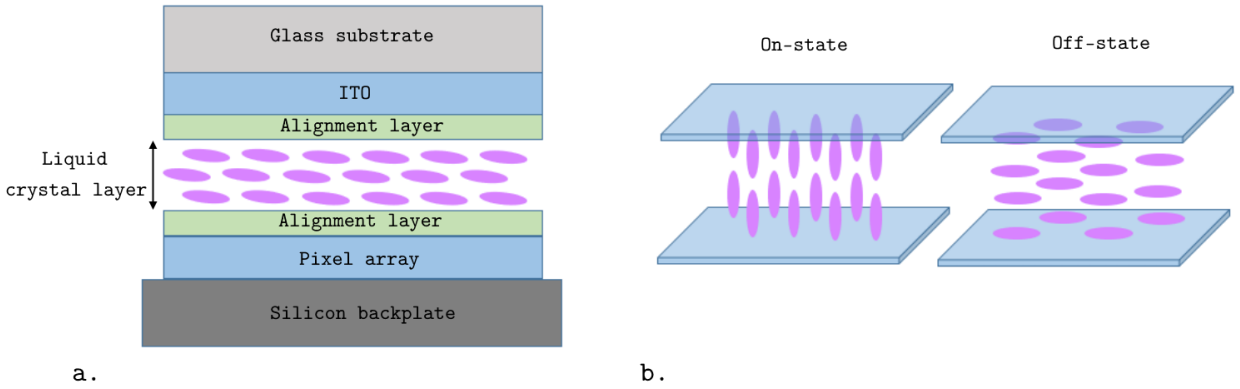

Figure 17 – a. Schematic description (simplified) of an electrically addressed reflective spatial light modulator based on liquid crystals. b. Orientation of the liquid crystals for an on and off state. Figure adapted from the work of Z. Zhang, Z. You and D. Chu [229]

Other SLMs rely on optical addressing schemes, in which case a liquid crystal display is used to project a pattern onto a photoconductive element [230]. It is difficult to achieve a precise linear phase control with optically addressed SLMs, however, electrically addressed SLMs may also present non exact pixel to pixel data mapping due to the sampling of the video data. Transmissive SLMs also exist, they are typically smaller and less complex than their reflective counterparts but have slower response time and lower zero-order diffraction efficiency. A good comparison between transmissive and reflective SLMs and between optically and electrically addressed SLMs can be found in the work of J. Harriman et al. [230].

Also, note that there are alternatives to liquid crystal based SLMs, such as magneto-optic based SLMs [231], deformable mirrors [232], which are excellent for incoherent light, and multiple quantum wells [233], ideal for fast optical switching.

Previous calibrations indicated that our SLM can produce relative phase difference up to $3\pi/2$ rad for a wavelength of 405 nm, for an incident linear polarization oriented at $45°$. The fact the SLM does not reach a full 2π phase modulation reduces its diffraction efficiency

[234, 235]. To improve the diffraction efficiency in a given order and overcome the phase modulation limitation of our SLM, a blazed phase grating can be used when designing the diffraction grid [236]. In our case, the diffraction efficiency is satisfactory for our experiments.

Using the principle of holography, it is possible to impart OAM to the beam reflected by the SLM. A computer-generated hologram is displayed on the SLM, allowing to dynamical control the reflected wave phase distribution. According to the principle of holography, the hologram displayed on the SLM corresponds to the interference pattern between a reference wave and the wave one wishes to generate. In order to spatially separate the desired beam, a small tilt angle is imparted to the reference wave, hereby forming a diffraction grid. When illuminated by the reference wave, the hologram will generate the desired wave in the chosen diffraction order. For OAM generation, we assume that the incident beam consists of a plane wave and the desired beam consists of a Laguerre Gaussian beam. The electric field of the reference field $\mathrm{E_G}$, tilted by a small angle θ, and the desired field $\mathrm{E_{LG}}$ read [237]:

$$\mathrm{E_G(x,y,z)}=\mathrm{u_G}\exp(\mathrm{i(kz-k\theta x)}) \quad \mathrm{E_{LG}(r,\phi,z)}=\mathrm{u_{LG}}\exp(\mathrm{i}\ell\phi+\mathrm{ikz}) \tag{3.1}$$

Where ℓ is the topological charge of the LG beam, which exhibits the characteristic azimuthal phase factor, where ϕ is the azimuthal angle. The intensity of the interference pattern is [237]:

$$\begin{aligned}\mathrm{I(r,\phi,z_0)}&=|\mathrm{E_{LG}}|^2+|\mathrm{E_G}|^2+\mathrm{E_{LG}E_G^*}+\mathrm{E_{LG}^*E_G}\\&=\mathrm{I_{LG}}+\mathrm{I_G}+2\mathrm{u_{LG}}\,\mathrm{u_G}\cos(\ell\phi+\mathrm{k\theta x})\end{aligned} \tag{3.2}$$

This forms a characteristic "fork"-shaped holographic grating, with spacing $2\pi/\mathrm{k}\theta$ in the x axis. The formation principle of the fork hologram is illustrated on figure (18). Our diffraction grating is generated via a Matlab routine, and displayed as an a 8-bit image, which corresponds to a range [0-255] of grey levels, scaled to the SLM phase retardation. The fork diffraction hologram obtained for an LG beam of topological charges $\ell=-1$ is given on figure (18). The line density, spacing, and blazing are adjusted to optimise the spatial resolution and intensity of the first-order diffracted beam.

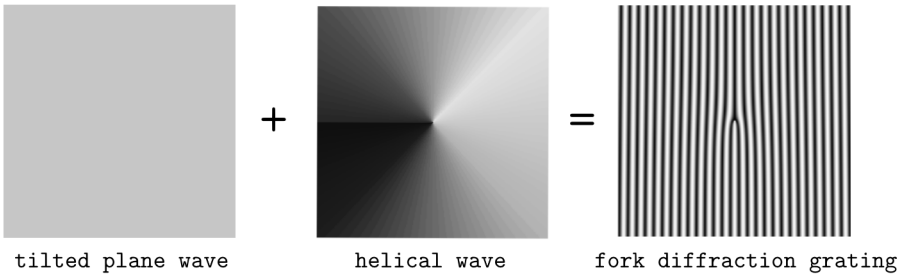

Figure 18 – Formation principle of a fork diffraction hologram for LG beams of topological charges $\ell=-1$. The fork diffraction grating corresponds to the interference pattern between a tilted wave of planar wavefront and a helical beam of topological charge $\ell=-1$, which phase evolution has been converted in gray intensity levels.

The diffracted beam diffracted in the n-order will carry an optical vortex of topological charge $\mathrm{q}n$, where q is the topological charge of the phase singularity embedded in the hologram, given by the difference in the number of diffraction lines on each side of the fork (upper and lower part in figure (18)). As highlighted by A. Bekshaev and S. Sviridova [238], ideally, a Gaussian beam incident on the SLM normal to the hologram plane and well centred on the hologram fork bifurcation produces a LG beam. In reality, a Kummer beam or hypergeometric Gaussian beam is often obtained, which corresponds to a superposition of LG modes with different radial indices [72]. Figure (19) illustrates how a fork diffraction grating, displayed on a reflection based phase only SLM can produce OAM-carrying beams from a Gaussian beam.

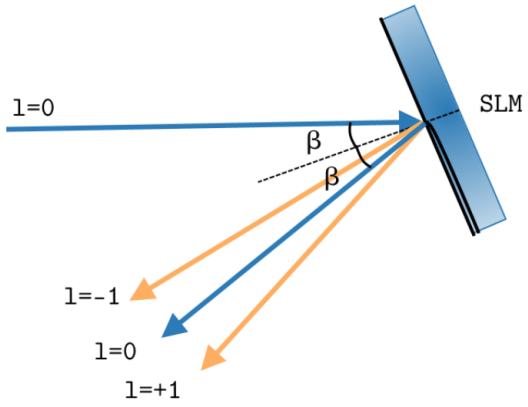

Figure 19 – Generation of OAM-carrying beam from a reflection SLM. The incident beam of topological ℓ=0 is diffracted by the fork hologram grid displayed on the SLM, generating a beam of topological charge ℓ=q, where q corresponds to the topological charge of the fork dislocation, here q=-1, in its first diffraction order.

The desired diffracted order can be spatially filtered using a screen placed after the SLM. A second linear polarizer is placed on the path of the selected diffracted beam to counter any spatial polarisation inhomogeneities, possibly introduced by the SLM.

The experimental intensity distributions of OAM-carrying beams generated in the first diffraction order of the diffraction grid, for a fork dislocation of topological charge $+1, +2, +3$ are presented on figure (20). As expected, the radius of the principal intensity ring increases with the beam topological charge. The ring intensity radius of pure LG modes of radial order 0 scales with the magnitude of the beam topological charge as $\ell^{1/2}$ [56].

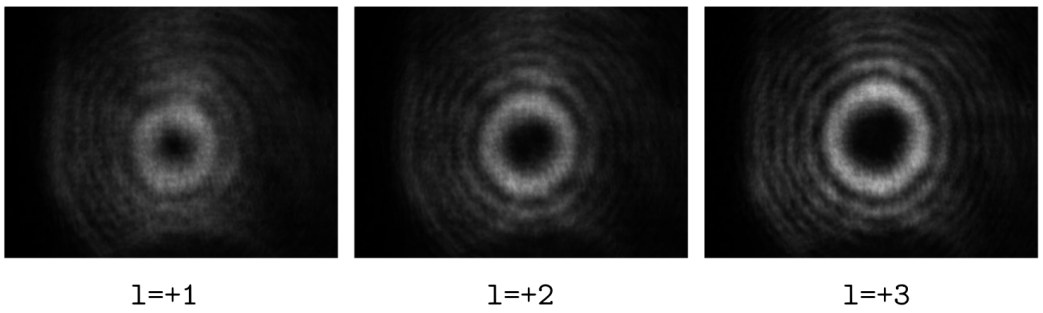

Figure 20 – Intensity distributions of the first-order diffracted beams for a fork grating dislocation of topological charge ℓ=$+1, +2, +3$.

Note that, on figure (20), non-zero radial modes are also observed, appearing as additional concentric rings. This is due to the fact that we are using a phase-only SLM [239]. Our SLM can generate LG-like beams up to a topological charge of magnitude $\ell{=}|5|$.

Several methods can be used to determine the topological charge of the first-order diffracted beam. An excellent review can be found in the book of D. Andrews and M. Babiker [56]. We have explored a few, which are listed bellow.

The triangular slit diffraction method, introduced by J. Hickmann et al. [240], consists of centring a cylindrically symmetric beam with unknown central topological charge on a small triangular slit aperture and examine the intensity distribution of the far field diffraction pattern. The far field distribution pattern results from the interference between edge waves and reveals the incident beam topological charge by counting the number of external points of the so-obtained triangular lattice. Changing the sign of the incident beam topological charge will cause the diffraction lattice to be mirrored. A square aperture has also been proposed, which is capable of measuring higher order topological charges than the triangular slit aperture but cannot distinguish between topological charge of opposite sign [241]. A few examples of far field diffraction patterns issued from a triangular slit and a square slit are given on figure (21).

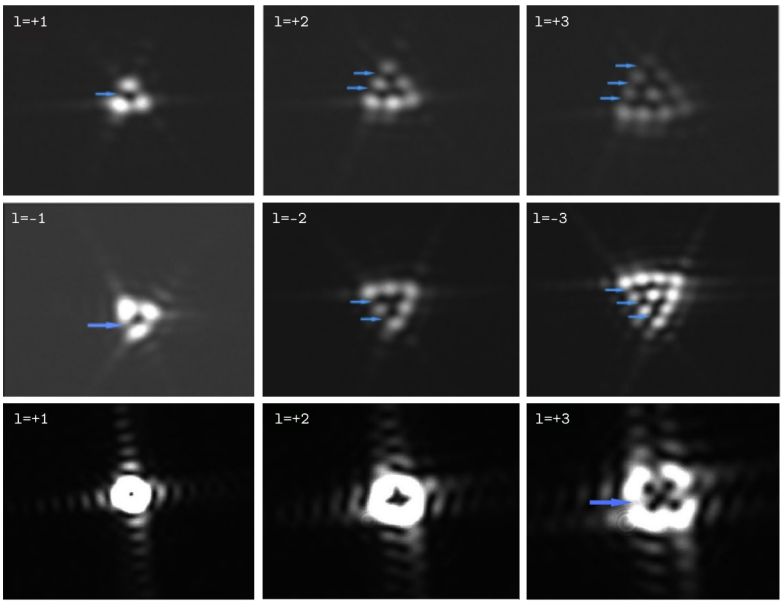

Figure 21 – Far field Intensity distributions of a beam carrying OAM by a triangular slit (2 first rows) and a rectangular slit, (third row) for incident beams of different topological charges ℓ. The blue arrows indicates intensity minima related to the beam topological charge. The far field of the triangular aperture is mirrored when the beam topological charge is inverted.

A single cylindrical lens or a tilted convex lens can also be used to determine the topological charge of a LG beam [82, 242]. The intensity distribution near the lens focal plane consists of the decomposition of the incident Laguerre Gaussian-like beam into an Hermite-Gaussian-like mode, the number of bright lobes observed corresponding to $\ell + 1$ and the tilt of the pattern discriminating positive from negative topological charges. A few examples of

intensity patterns obtained by the passage of an OAM-carrying beam through a tilted convex lens are given on figure (22).

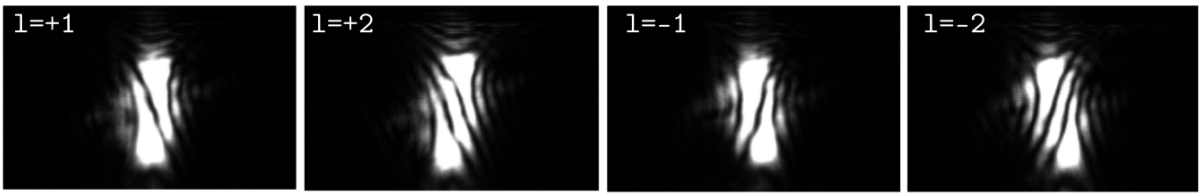

Figure 22 – Intensity distributions near the focal plane of a tilted convex lens, for incident beams of topological charges ℓ=+1, +2, −1, −1,.

Interferometry can be used to determine the beam topological charge and is particularly interesting to determine the position of the OV core. When interfering our Laguerre-Gaussian-like beam with a beam with a planar wavefront, we recover the "fork" interference pattern, where the dislocation indicates the position of the vortex core. The topological charge is given by the difference between the number of fringes above and under the fork. An example of such interference pattern is provided in figure (23), where this technique was used to determine the position and topological charge of a pair of OV cores embedded in a Gaussian beam.

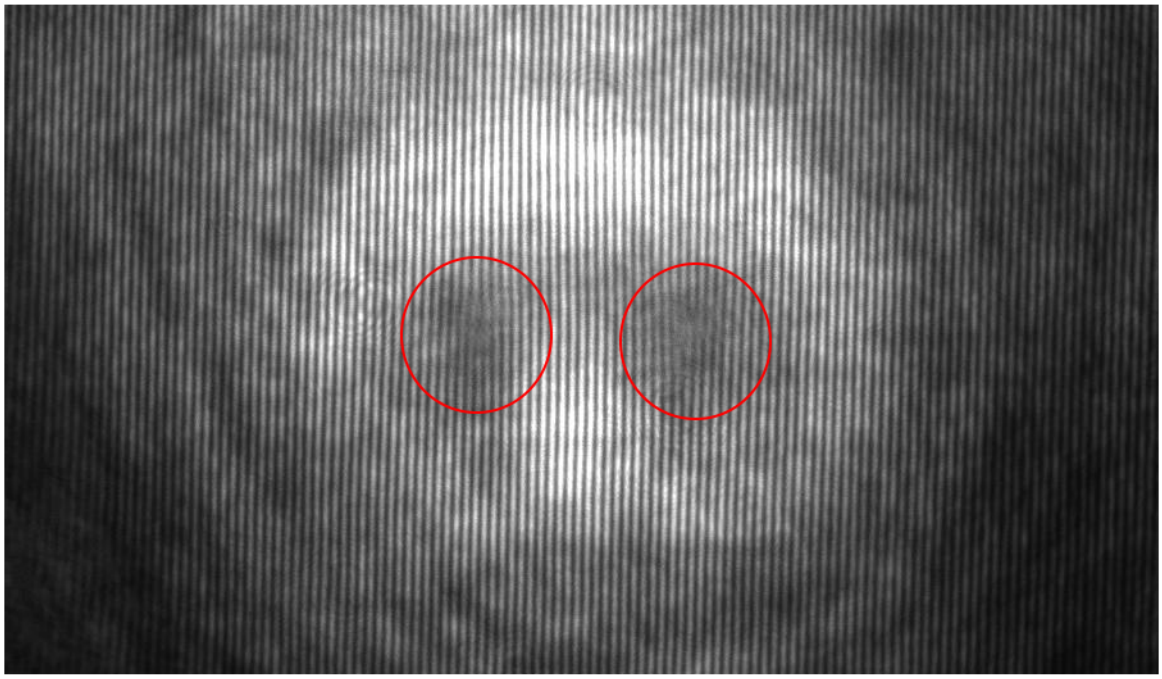

Figure 23 – Interference pattern of a plane wave and a Gaussian beam embedded with a pair of optical vortex cores of topological charge ℓ=−1 (left) and ℓ=+1 (right), as evidenced by the fork dislocations. (For a separation distance of 35 pixels between the OV cores, on the SLM). The red circles indicate the location of each fork.

In the case of edge diffraction or symmetry breaking, it is possible to determine the sign of the beam topological charge by observing in which direction the intensity penetrates the dark region in the far field [227]. Further details regarding the origin of this phenomena will be provided when discussing our results.

Note that the all of the methods described above give access to the average value of OAM carried by the beam, i.e., they are not indicated to perform a modal decomposition.

Now that I have described how an OV can be embedded in a Gaussian beam and how to characterize the mean OAM content of the beam, I will describe how the symmetry of the beam can be broken using a Fresnel biprism.

The Fresnel biprism was introduced in the 19th century by A. Fresnel, who proposed to join two thin prisms at their base [243]. The purpose of this device was to demonstrate the wave nature of light and corroborate Young's findings. At the time, some objections were raised regarding the origin of the fringes observed in Young's double slit experiment [244]. It was argued that the fringes could possibly not be attributed to interference between the two waves but rather arise due to "complicated modification of the light by the edges of the slits" [245]. Fresnel's biprism allows to observe interference fringes without edge effects.

When illuminated by a plane wave, a Fresnel's biprism performs wavefront splitting. For a configuration as illustrated on figure (24 a.), the part of the beam incident on the right part of the Fresnel biprism, defined in relation to the Biprism apex, is refracted to the left (L) whereas the beam part incident on the left part of the biprism is refracted to the right (R).

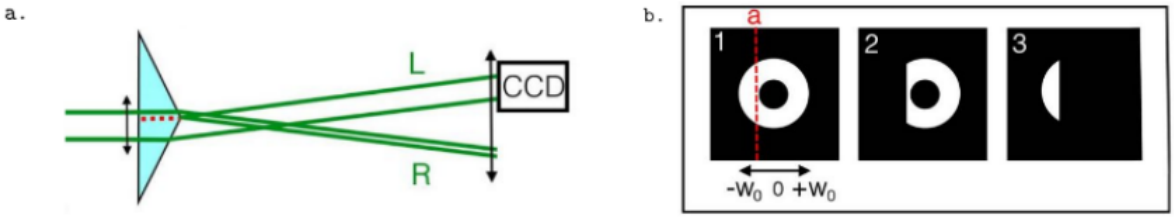

Figure 24 – Wavefront splitting by a Fresnel Biprism. a. An incident beam, delimited by two rays (in green), is incident on a Fresnel biprism. A ray located on the left side of the biprism's apex is refracted to the right whereas a beam located on the right side of the biprism's apex is refracted to the left. The biprism is mounted on a translation stage such that the relative position between the incident beam and the biprism apex (red dotted line) is varied. A CCD camera, positioned on a translation stage, can image both beam parts. b. An incident azimuthally symmetric beam (1) is split into two variable beam parts, depending on the relative position between the incident beam and the biprism apex (red doted line). The beam part refracted to the left and to the right, as defined in a., correspond to the intensity distribution (2) and (3), respectively.

The two beam parts interfere in a region near the biprism exit. The resulting interference pattern can be seen as the result of the interference between two virtual sources, in analogy to Young's double slit experiment. A Fresnel biprism can be seen as a truncated refractive axicon [246], the later being known notably for its capacity of generating Bessel-like beams [247].

Beyond the interference region, the two beam parts are spatially separated. We consider a biprism of diffraction angle $\beta = 6.46$ mrad and mounted on a millimetric stage such that the incident symmetric beam can be split into two complementary parts of variable width. The position of the biprism apex is denoted by a variable **a** and varies from $-w_0$ to w_0, where w_0 is the waist radius of the incident beam. Consequently, for $\mathbf{a} = 0$, the biprism splits the incident

beam in half. Figure (24 b.) illustrates the splitting of an incident azimuthally symmetric beam (1) into two beam parts, depending on the relative positioning of the biprism apex **a** and the incident beam. The beam parts reflected to the left and to the right, as defined in (24 a.), correspond to the schematic intensity distribution denoted (2) and (3), respectively.

A CCD Camera of resolution 1296×964 and pixel size $3.75\mu\mathrm{m}$ is placed at 600 mm after the biprism and is fixed on a millimetric stage such that it can record the intensity distribution of both complementary diffracted beam parts. Care is taken not to saturate the image. The recorded image is a 16-bit grayscale image, saved in a PNG format.

3.1.3 Orbit-orbit interactions: experimental and numerical studies

We aim at studying orbit-orbit interactions of light upon beam splitting by a Fresnel Biprism. To do so, we measure angular deviations induced by symmetry breaking, for each position of the biprism, i.e., for a specific beam splitting. For a position **a**, the CCD camera records the intensity distribution of the beam part refracted in the right direction, as defined on figure (24), as the beam topological charge is varied from $\ell{=}0$ to $\ell{=}{\pm}5$ on the SLM. The CCD camera is then translated to record the beam part refracted in the left direction, and records a second series of images, as the beam topological charge is varied from $\ell{=}0$ to $\ell{=}{\pm}5$ on the SLM. The process is repeated for various positions of the biprism **a**.

The intensity distributions are imported in Matlab and a black mask is numerically added to the image, such that the intensity distribution from higher radial modes can be discarded. A program then exports the coordinates of the center of gravity for each image by weighting the grayscale distribution over the image. The analytical expression for the center of gravity of each beam part in the transverse plane can be defined as:

$$\mathbf{g}_{\mathbf{R},(\mathbf{L})}(\ell,\mathbf{a}){=}\frac{1}{\mathrm{P}}\int \mathbf{r}\,|\mathrm{u}_{2,\mathrm{R(L)}}(\ell,\mathbf{a})|^2\mathrm{dxdy} \tag{3.3}$$

Where **r** is the transverse radius vector, P corresponds to $\mathrm{P}{=}\int|\mathrm{u}_{2,\mathrm{R(L)}(\ell,\mathbf{a})}|^2\mathrm{dxdy}$ and $\mathrm{u}_{2,\mathrm{R(L)}}(\ell,\mathbf{a})$ is the amplitude associated with the right (or left) beam part, for a position of the biprism **a** and incident topological charge ℓ. According to the work of A. Bekshaev, in edge diffraction, symmetry breaking of an incident cylindrically symmetric Laguerre Gauss beam with zero radial order should introduce angular deviations of the refracted beam, with respect to its geometric expectations, parallel to the screen edge and dependent on the incident beam topological charge [228]. Considering that the apex angle of our biprism is small, similar angular deviations are expected in our configuration. In this case, the angular deviations for each beam part occur along the y direction and can be written as:

$$\theta_{\mathrm{y}}{=}\mathrm{atan}[(\mathbf{g}_{\mathbf{R(L)}}(\ell,\mathbf{a}) - \mathbf{g}_{\mathbf{R(L)}}(\ell{=}0,\mathbf{a}))/\mathrm{z}_{12}] \tag{3.4}$$

Where $\mathbf{g}_{\mathbf{R(L)}}(\ell{=}0,\mathbf{a})$ is the center of gravity of a Gaussian beam, which corresponds to the geometric expectation of the beam centroid in the absence of OAM. In equation (3.4), z_{12} corresponds to the propagation distance of the respective beam part, from the biprism exit plane.

By numerically extracting the center of gravity of each beam part and using equation (3.4), the experimental angular deviations for topological charges ranging from $\ell{=}{-}5$ to $\ell{=}{+}5$ can be plotted as a function of the relative position between the incident beam and the biprism apex **a**. Our results are showed in figure (27) and will be further discussed in what follows.

The error of the measurement method described above for angular deviations induced by symmetry breaking is evaluated by considering a beam entirely refracted in one direction and comparing the center of gravity obtained for beams of topological charge ranging from $\ell{=}0$ to $\ell{=}{\pm}5$. The error, converted in angular deviations is 0.03 mrad.

Our experimental study is complemented with a numerical model. Let be a monochromatic, paraxial Laguerre-Gauss of azimuthal order ℓ and radial order 0, propagating in the z-direction. In the biprism exit plane ($z_{12}{=}0$), the field complex amplitude can be written as

$$\mathrm{u_1}(\ell, \mathbf{a}){=}\mathrm{LG_{0\ell}}(\ell)\mathrm{FB}(\mathbf{a}) \tag{3.5}$$

Where $\mathrm{FB}(\mathbf{a})$ accounts for the action of the biprism, namely

$$\mathrm{FB}(\mathbf{a}){=}\exp(-\mathrm{ik}(\beta/2)\mathrm{sgn}(\mathrm{x}-\mathbf{a}))(\mathrm{x}-\mathbf{a}) \tag{3.6}$$

Therefore, at the biprism exit plane, the beam is separated into two parts, determined by the relative position of the incidence beam and the biprism apex position **a**, and each part has a distinct propagation direction, forming an angle $|\beta/2|$ with the z-axis.

The total electric field complex amplitude at the biprism exit plane, denoted by the subscript 1, can thus be written as a sum of two electric fields propagating in different propagation directions, i.e. $\mathrm{u_1}{=}\mathrm{u_{1,R}}(\ell, \mathbf{a}) + \mathrm{u_{2,L}}(\ell, \mathbf{a})$.

The electric complex field at a propagation distance $\mathrm{z_{12}}$, denoted by the subscript 2, is obtained by applying the Rayleigh-Sommerfeld diffraction formula on the respective beam parts:

$$\mathrm{u_{2,R(L)}}(\ell, \mathbf{a}){=}\iint \mathrm{u_{1,R(L)}}(\ell, \mathbf{a})(\mathrm{z_{12}}/(\mathrm{i}\lambda\,\mathrm{r_{12}^2}))\exp(+\mathrm{ik}\,\mathrm{r_{12}})\mathrm{dx_1 dx_2} \tag{3.7}$$

The Rayleigh-Sommerfeld diffraction formula was introduced as an alternative to Kirchoff's diffraction theory. A detailed analytical description of the Rayleigh-Sommerfeld Diffraction formula and a comparison between the Rayleigh-Sommerfeld and the Kirchoff diffraction theories can be found in the book of J. W. Goodman [248]. Both the Rayleigh-Sommerfeld and the Kirchoff diffraction theory are concerned with scalar waves, and yield satisfactory results as long as the diffracting apertures is large in comparison to the wavelength and that the diffraction field under consideration is not too close to the aperture [3].

Numerically, the Rayleigh-Sommerfeld diffraction integral can be calculated by either angular spectrum method (ASM) or direct integration method [250, 251]. The former uses a Fourier transform to compute the light field in the spatial-frequency domain whereas the latter computes the diffraction integral in the spatial domain using numerical integration, which can be

[3] Note that vectorial generalizations of diffraction do exist [249]

treated as a linear convolution and relied on a fast Fourier Transform and an inverse fast Fourier Transform. We adopt the ASM method, which is suited for far field calculations and allows to calculate the diffracted field $\mathrm{u_2(x,y)}$ from the incident field $\mathrm{u_1(x,y)}$ as [251]:

$$\mathrm{u_2(x,y)}=\mathcal{F}^{-1}(\mathcal{F}(\mathrm{u_1(x,y)})\times\mathcal{H}(\mathrm{k_{x,k_y}})) \tag{3.8}$$

Where $\mathcal{H}(\mathrm{k_x,k_y})$ is the spatial frequency transfer function and $\mathcal{F}$ and $\mathcal{F}^{-1}$ refer to the Fourier transform and inverse Fourier transform, respectively. We define a 4096×4096 pixels grid and the sampling of the spatial and the frequency domains are optimised to avoids aliasing as well as large computational loads, as described in the book of T. Poon and J. Liu[251]. The transfer function is defined as follows;

$$\mathcal{H}[\mathrm{p,q}]=\exp(-\mathrm{ik_0z}\sqrt{1-\frac{(\mathrm{p}\Delta_{\mathrm{kx}})^2}{\mathrm{k_0^2}}-\frac{(\mathrm{q}\Delta_{\mathrm{qy}})^2}{\mathrm{k_0^2}}}) \tag{3.9}$$

Where $\delta_{\mathrm{kx(ky)}}$ is the sampling period in the frequency domain and $\mathrm{p,q}$ is the indices of the samples in the spatial domain.

The intensity distribution in the $\mathrm{z_{12}}$ plane is then calculated from the so-obtained electric field and is plotted as a greyscale image.

The coordinates of the beam centre of gravity of each beam part are then extracted using the same algorithm as the one described above to analyse our experimental intensity distributions. However, this time, no mask is applied, as our computed LG beam already has a radial order 0. The beam angular deviations from the $\ell=0$ LG beam for various **a** are calculated using equation (3.4). Our results are then plotted (see figure (27)) in order to compare our numerical and experimental results.

3.1.4 Results and discussion

For a position $\mathbf{a}=0$ of the biprism, i.e., when the incident is split in two complementary half beams, the intensity distributions issued from both the experimental and numerical evidence, at a propagation distance of 60 cm after the biprism, the migration of a part of the intensity profile beyond the screened region and the recession of part of the beam intensity profile into the non-screened region, as illustrated on figure (25) for an incident beam of topological charge ±5. This phenomena is observable in each beam part. If the beam topological charge is inverted, the recessing region becomes the migrating region and vice versa, as illustrated on figure (25). Also, the presence or absence of higher radial orders does not alters this result, at least from a qualitative perspective.

The rotation of the field transverse profile near the nominal propagation axis has been studied in detail in edge-diffracted LG beam by A. Bekshaev et al. in 2014 [252]. In this work, A. Bekshaev et al. show that as the propagation distance increases, the beam transverse intensity profile further rotates, enters the screened region and stabilises in the far field, where the beam intensity distribution is perpendicular to the screen edge. This observation is valid for severe or

partial screening of the incident beam. A. Bekshaev et al. interpreted their findings in terms of transverse energy circulation, by arguing that, introducing symmetry breaking cause the initially "hidden" vortex form of transverse energy circulation can be converted into a form of asymmetry transverse energy circulation. This study is based on irradiance moments.

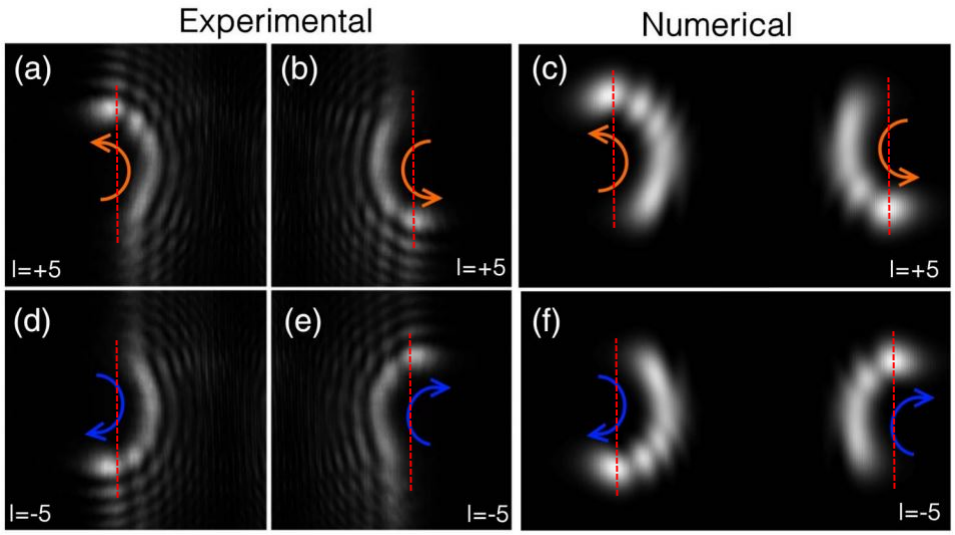

Figure 25 – Experimental (left row) and numerical (right row) intensity distributions of complementary beams parts, issued from an initial circular LG beam of topological charge $\ell{=}-5$ and $\ell{=}+5$, split by a Fresnel biprism, at a propagation distance $z_{12}{=}60\mathrm{cm}$. The arrows indicate the rotation direction of the intensity pattern and the dotted red line indicates the initial beam central axis.

Alternatively, the rotation of the field transverse profile can be understood in terms of the Gouy phase of the beam. In a paper from 2006, J. Hamazaki et al. studied the behaviour of a focused $p{=}0$, $\ell{=}\pm10$ LG beam while introducing an asymmetric defect (using a dark sector) [253]. As illustrated on figure (26), the authors experimentally show that the defect rotates upon propagation, in opposite directions for opposite topological charges, while intensity distributions, equidistant and in opposite direction of the focal plane form vertically mirrored images. While the later effect is observed in $\ell{=}0$ beams, the rotation is not. This behaviour can be attributed to the Gouy phase. The Gouy phase of a LG_{p}^{ℓ} can be expressed as:

$$\Phi_{\mathrm{Gouy}}(z){=}(2p{+}|\ell|{+}1)\arctan(z/z_{R}) \tag{3.10}$$

Where z_R is the Rayleigh length. Upon propagation, the intensity profile of an OAM-carrying beam rotates by an angle:

$$\Delta\theta{=}\mathrm{sng}(\ell)\arctan(z/z_{R}) \tag{3.11}$$

This also explains why the intensity distribution ceases to rotate in the far field in the study of A. Bekshaev et al., as for $z{\to}{\pm}\infty$, $\Phi_G{\to}{\pm}\pi/2$.

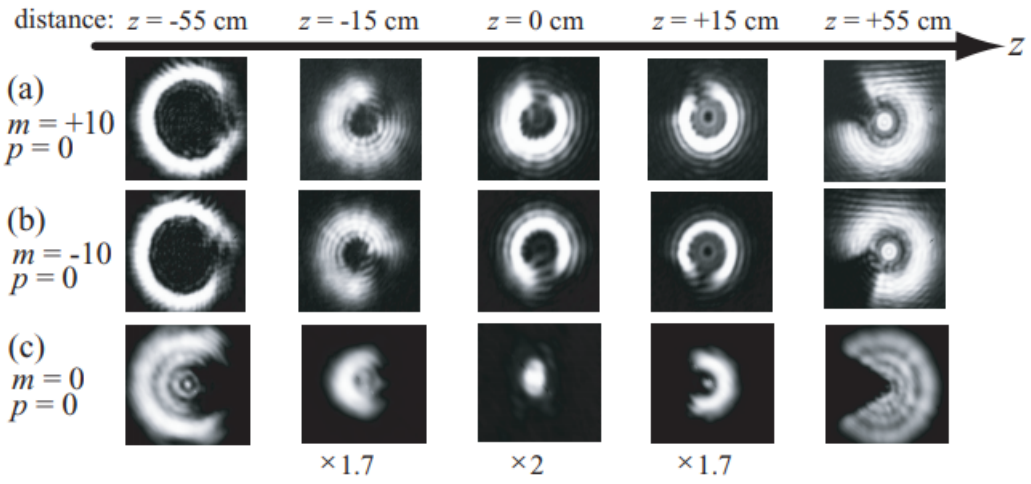

Figure 26 – Spatial evolution of modified LG beam with an asymmetric defect, figure from the work of [253]. Here, m is the LG beam topological charge and p its radial order and z indicates the distance before (negative) and after (positive) the focus plane (z=0).

In a complementary numerical study, J. Hamazaki et al. showed the evolution of the intensity distribution from z=$-\infty$ to z=$+\infty$ (z= being the focal plane) [253]. They evidenced that the defect rotates at a constant rate for all ℓ in a LG beam of radial index p=0 but that the phenomena is pronounced for larger $|\ell|$, because of the radial dependence for LG modes.

The authors also investigated a LG beam with radial order p=5 and topological charge ℓ=+10. They find that, while from $-\infty$ to $+\infty$, all rings undergo a full π rotation (two times $\pi/2$ on each side of the focus plane), the rotation rate of the individual rings is not the same. For a rotation angle $0<|\varphi_{\mathrm{rot}}|<\pi/2$, the inner rings rotate faster than the outer rings. This process reverses in the $\pi/2<|\varphi_{\mathrm{rot}}|<\pi$ part of the evolution [253]. Similar results have been obtained by S. M. Baumann et al. [254].

Interestingly, the Gouy phase shift has also been interpreted as the manifestation of a general Berry phase [255, 256].

Also note the presence of fringes in both the numerical and experimental intensity distribution on figure (25). I. Zeylikovich and A. Nikitin [257] argued that such fringes naturally appear in the diffraction from a gaussian beam and are the result from the interference between the helical wave created by an optical vortex near the cusp of a caustic formed in the shadow region of the straight edge and the cylindrical wave diffracted at the straight edge.

As illustrated on figure (27), both experimental and numerical results evidence angular, θ_{y} of equation (3.4), deviations from the geometric expectation, parallel to the biprism apex line. For a fixed value of **a**, the angular deviation scales with $|\ell|+1$. The angular deviations of the complementary beam parts are correlated, which increases the sensitivity of the Fresnel-biprism-based configuration to calculate angular deviations in comparison to edge diffracted beams.

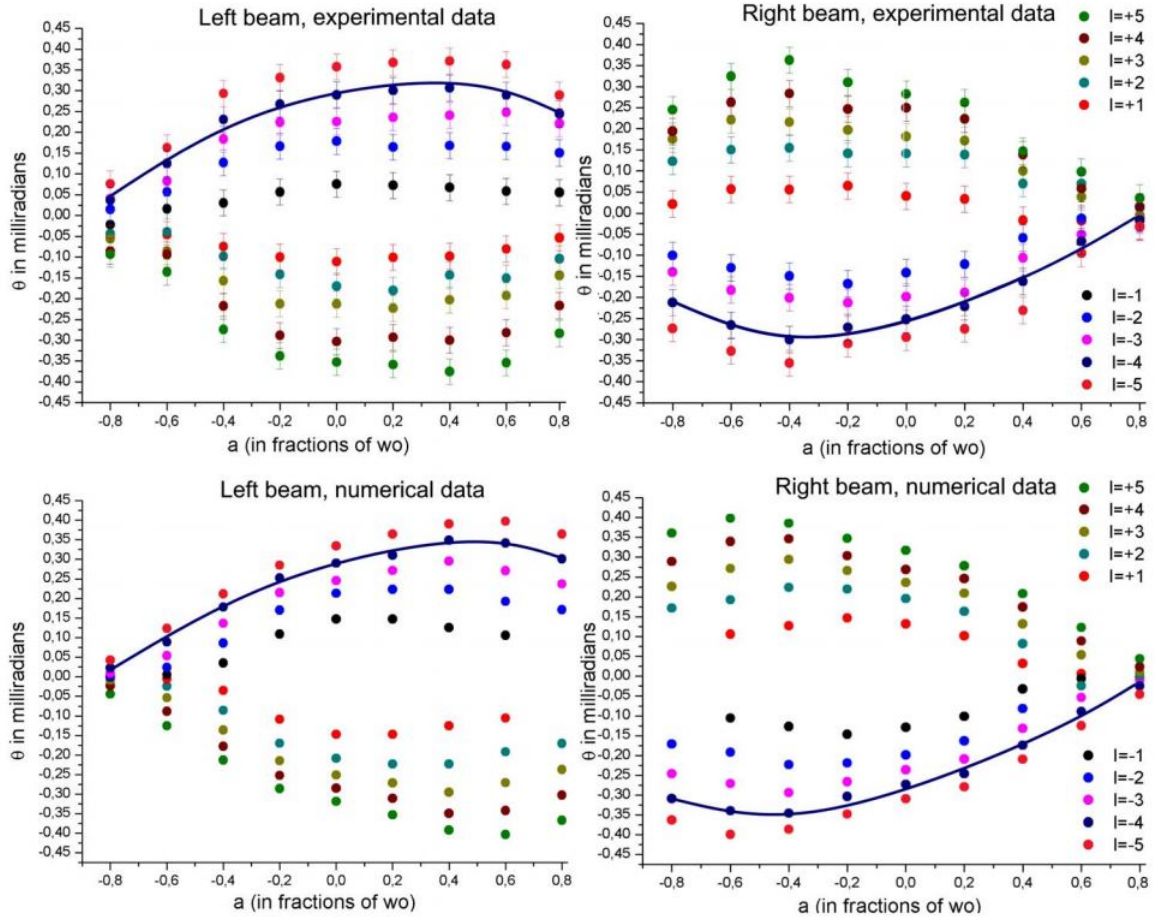

Figure 27 – Angular deviations of complementary beam parts of an initially symmetric LG beam, split by a Fresnel Biprism, in function of the relative position **a** between the incident beam and the Fresnel biprism apex. The blue line emphasizes the correlation between the right and left split beams for $\ell{=}-4$.

If the diffracted beam almost retains its circular symmetry, such is the case for $\mathbf{a}{=}-0.8$ and $\mathbf{a}{=}+0.8$ for the Left and the Right beam parts, respectively, angular deviations are small. Angular deviations increase as the beam asymmetry increases. However, the maximum value for angular deviations does not corresponds to $\mathbf{a}{=}0$, i.e., for two half beam parts. Take the left beam part for instance, for $\ell{=}-4$, the angular deviation is maximum for $\mathbf{a}{\approx}0.45$ for experimental results and for $\mathrm{a}{=}0.5$ for numerical results. Now for $\ell{=}-1$, these maxima are reached for $\mathbf{a}{\approx}0.05$ for experimental results and for $\mathbf{a}{=}0.1$ for numerical results.

These results are in agreement with A. Bekshaev's predictions, namely, that the angular deviation vanishes for a circularly symmetric beam and that the magnitude of the angular deviation does not grow monotonically [228].

Still according to A. Bekshaev, the transverse angular shift of a truncated beam should correspond to the transverse canonical momentum produced by the tilt of the beam and can be written as [4]

$$\mathrm{p}_{\perp}{=}\frac{1}{\mathrm{kP}}\mathrm{Im}\int \mathrm{u}_{\mathrm{y}}^{*}\nabla \mathrm{u}_{\mathrm{y}}\mathrm{dxdy} \tag{3.12}$$

[4] In our case, the direction parallel to the screen edge is the y, not the x direction.

The transverse canonical momentum along with the orthogonal displacement of the beam center produces EOAM. For an incident circular LG beam of radial order 0, equation (3.12) yields angular deviations proportional to the incident OV topological charge. As commented by A. Bekshaev, in general, the analytical expression for $\mathrm{p}_\perp$ is quite complex. For this reason, we calculate the values of transverse canonical momentum along y for $\ell{=}\pm1$ for various values of **a**, assuming an initial full and symmetric beam such that [5]

$$\mathrm{p}_\perp{=}\mp\gamma[\mathrm{q}+\sqrt{\pi}\,\mathrm{erfc}(\mathrm{q})\exp(\mathrm{q}^2)]^{-1} \tag{3.13}$$

Where it is assumed that the screen plane coincide with the beam waist. With $\mathrm{q}{=}\mathbf{a}/\mathrm{w}_0$ and q scaling from -1 to +1 and with $\gamma{=}(\sqrt{2}\,\mathrm{kw}_0)^{-1}$.

Figure (28) evidences good agreement between the transverse angular momentum values obtained from the analytical expression described in equation (3.13) and the experimental angular deviations for several **a**, for a beam of topological charge $\ell{=}-1$.

Discrepancies between experimental and numerical results can be attributed to our numerical integration method for the beam intensity profile due to slight asymmetries in the incident beam profile and the presence of small contributions from higher order radial modes, despite the application of a mask. Fresnel-based wavefront splitting however remains a promising approach to improve the accuracy of deviation calculations, by taking advantage of the complementarity between each beam part. Future works should ideally rely on a quadrant detectors or use weak measurements methods to improve the accuracy of the measure of angular deviations [258, 259].

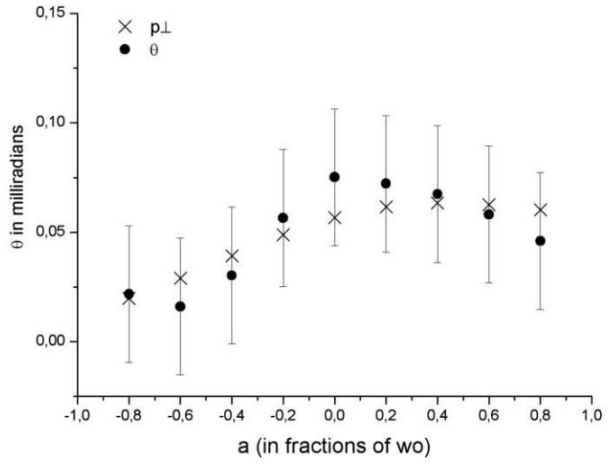

Figure 28 – Experimental and analytical angular deviations for an incident circular LG beam of topological charge $\ell{=}-1$, in function of the relative position **a** between the incident beam and the Fresnel biprism apex.

Beyond topological-dependent trajectory changes, i.e., orbit-orbit interactions, as evidenced above, it would also be interesting to study in further details the OAM transformation, such as the transfer of IOAM from vortex related IOAM and asymmetric IAOM, as defined by A. Bekshaev et al. [252]. It should also be interesting to consider that the incident mode purity is

[5] This expression slightly differ from the one found in the work of A. Bekshaev due to different definitions of the beam waist and **a**.

degraded when the spatial profile is restricted [94]. It recently came to our knowledge that the modal distribution of an OAM-carrying beam can be simply evaluated by using a second SLM or by using half of the primary SLM for mode sorting [260].

We also investigated the evolution of the OV core as **a** is varied. The position of the OV core was determined by interferometry. In our configuration, we did not observe the creation of auxiliary vortices, as predicted by A. Bekshaev et al. in the case of edge diffraction [227]. Figure (29) shows the interference pattern between the tail of each beam part, which can be approximated by a planar wavefront, and each beam part, at a short propagation distance after the biprism. When varying **a** such that the OV core passes from being diffracted on the left to the right direction, we observed that the OV core simply jumps from one split beam part to the other. We obtained similar numerical results.

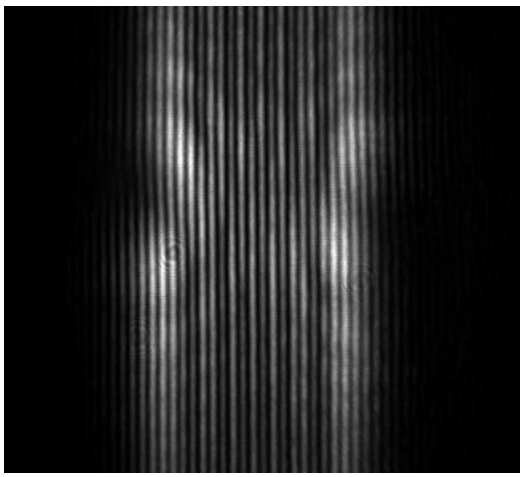

Figure 29 – Interference pattern between each beam part, for a beam topological charge $\ell{=}1$.

As a complementary study about orbit-orbit interactions, **Appendix 3** shows the interactions of two OV cores embedded in a diffracting LG beam. Our numerical results show that the topological charge of individual vortices influence the trajectory of individual OV cores and that a beam carrying OV cores of opposite topological charge separated by a small distance annihilate whereas beams with the the same topological charge do not. Similar studies about OV cores interactions can be found in the work of G. Molina-Terriza et al. [261].

3.2 Astigmatism in a vertical gradient of refractive index

3.2.1 Motivation

When investigating the evolution of OV cores in a symmetrical optical beam, a review of G. Molina-Terriza [56] came to our attention. In this review, the process of topological charge inversion in an asymmetric paraxial monochromatic beam is described.

The author gives a definition for the most general kind of stable isolated vortices, namely, "noncanonical" vortices. In the vicinity of an OV of unit topological charge, located at $(\mathrm{x_1}, \mathrm{y_1})$, the scalar field can be written as $\mathrm{E(x{\approx}x_1, y{\approx}y_1){=}a_x(x-x_1)+a_y(y-y_1)+O(x^2, y^2)}$,

where a_x and a_y are complex. Assuming $a_x \neq 0$, the electric field becomes [56]

$$E(x \approx x_1, y \approx y_1) = C((x - x_1) + i\,A(y - y_1)) + O(x^2 + y^2) \tag{3.14}$$

Where $C = a_x$ and $A = -i\,a_y/a_x$. The variable A is the noncanonical parameter of the OV core, the sign of its real part defines the vortex topological charge. Equation (3.14) allows to determine the intensity of the field associated with the non-canonical parameter A. G. Molina-Terriza provides a thorough study of the general dynamics of OV cores.

While the topological content of an optical beam is known to change when vortex-antivortex pairs are created or annihilated, as showed in **Appendix 3**, or when vortices appear or disappear from a reservoir at infinity, such as demonstrated in the work of A. Bekshaev, G. Molina-Terriza shows that an OV can also transform due to continuous deformations of its noncanonical parameter. In particular cases, this leads to an inversion of the beam topological charge, i.e., A changes sign [56].

Topological charge inversion is witnessed when a canonical vortex, embedded in the center of a collimated circular Gaussian beam, traverses an astigmatic lens. In this case, the OV core becomes elliptical until it becomes an edge dislocation [262]. In terms of OAM, in a linear homogeneous media, OAM is conserved along the propagation direction. For an incident circularly symmetric host beam, a cylindrical lens only mixes the eigenfunctions of angular momentum. The asymmetric beam produced by the lens is characterized by a superposition of angular momentum eigenmodes. For an incident beam carrying an OV core of unit topological charge, the main contribution comes from the modes of order $+1$ and -1. From the perspective of geometric optics, the cylindrical lens produces a mirror image of the incident field.

In this context, we decided to study OAM transformation in an incident monochromatic, paraxial cylindrical LG beam when introducing astigmatism in a vertical gradient of refractive index (VGRIN). This is, to my knowledge, the first time OAM is being investigated in a VGRIN, the large majority of studies being dedicated to gradients of refractive index maintaining a form of cylindrical symmetry, such is the case in waveguides [263, 264]. Contrary to mirror inversion occurring at sharp interfaces, a VGRIN allows to study OAM transformations as astigmatism is slowly introduced.

3.2.2 Realisation and probing of a Vertical gradient of refractive index

Mirage effects have been experimentally reproduced by heating surfaces [265, 266] and by superposing liquids if different densities [267, 268]. We choose the later approach as it is relatively risk-free, easy to implement, and minimizes edge effects.

A cylindrical glass cell of inner diameter 26 mm and 200 mm length enclosed with two quartz windows is filled with distilled water in its lower half and its upper half is filled with ethanol (>99,9%). Ethanol is poured in such a way to minimize initial liquid mixing. Ethanol having a lower density and higher refractive index with respect to distilled water, a VGRIN

establishes through the solution. A He-Ne laser beam is used to probe the solution as illustrated on figure (30). The beam deflections confirm the presence of a VGRIN.

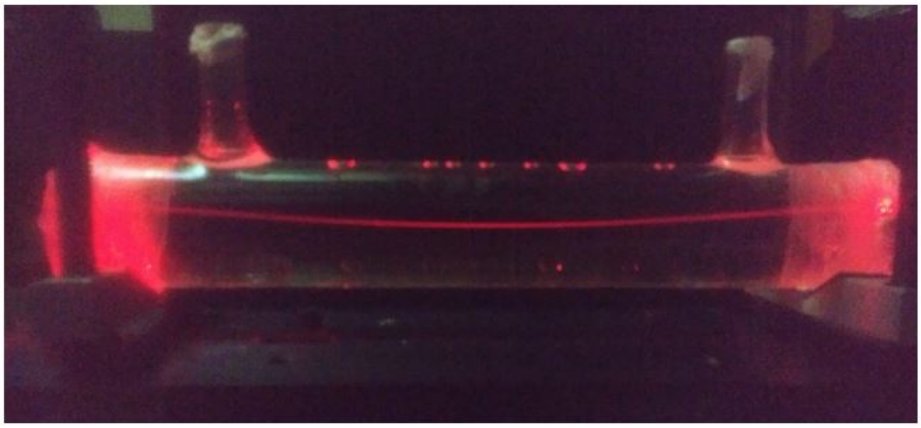

Figure 30 – A He-Ne laser beam (λ=632.8 nm) propagating through a binary solution of distilled water and ethanol. Commercial ethanol is used here for illustrative purposes only.

In the following, a GaN Fabry Perot laser diode source of wavelength 405 nm is used. The beam is collimated by a telescope to achieve a waist radius of size $850\,\mu\mathrm{m}$ at half of its maximum intensity. The same SLM and fork diffraction gratings as the ones described in the last section are used to impart OAM. After being spatially filtered, the beam corresponding to the first diffracted order is incident on a pair of mirrors which control the beam incidence angle on the cylindrical glass cell. The glass cell is positioned on a translation stage, which allows to control the incidence height of the incident beam upon the binary solution. A CCD camera is placed at the cell exit plane. The whole experimental setup is illustrated on figure (31).

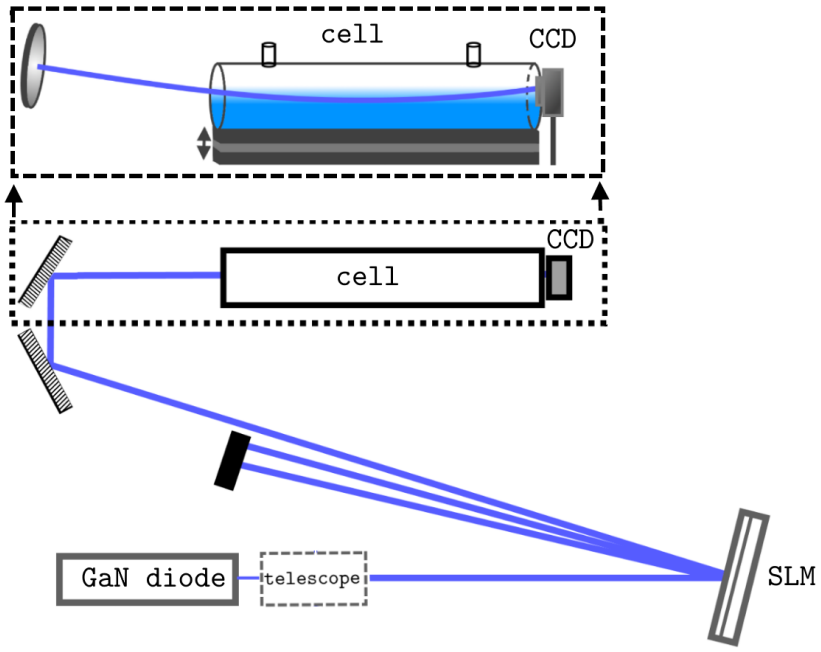

Figure 31 – Experimental setup for probing a vertical gradient of refractive index with an optical vortex beam (viewed from above). The inset above shows how the incident beam angle and height are adjusted. The cell is filled with a binary solution of water (in blue) and ethanol (in white).

A few minutes after the cylindrical cell is filled the incidence height of the beam is adjusted such that it enters the solution with a few millimetres above the water-ethanol interface with a small incidence angle ($\theta_0 < 5°$). Initially, two consecutive total internal reflections (TIR) are observed. Four hours later, a single TIR is visible, slowly fading away over the course of the next six hours. The VGRIN profile thus changes over time and gradually loses its steepness.

The temporal evolution of the VGRIN formed by a binary solution of distilled water and ethanol can be understood based on the following considerations. For a binary mixture, the refraction index of the solution is given by the Gladstone-Dale empiric relation [269]

$$(n_{mix} - 1)/\rho_{mix} = \alpha_1[(n_1 - 1)/\rho_1] + \alpha_2[(n_2 - 1)/\rho_2] \tag{3.15}$$

With $\alpha_{1,2}$ being the weight of the pure components and $n_{1,2}$ and $\rho_{1,2}$ being the refractive index and density of the pure components, respectively. For $\lambda = 405$ nm we consider $n_{H_2O} = 1.3429$ and $n_{C_2H_6O} = 1.3725$ [270, 271].

Assuming that there is no variation of refractive index along the horizontal direction, and based on the work of T. Zhang et al. [272], the VGRIN profile of the present binary solution can be expressed as:

$$n(y) = n_{H_2O} + a \cdot \mu(y) + b \cdot \mu(y)^2 + c \cdot \mu(y)^3 \tag{3.16}$$

With $a = 7.972 \times 10^{-2}$, $b = -3.706 \times 10^{-2}$, $c = -1.381 \times 10^{-2}$ and with $\mu(y)$ corresponding to the mass fraction of ethanol as function of liquid height which can be written as

$$\mu(y) = (1 + \mathrm{erf}(y - y_0)/d)/2 \tag{3.17}$$

with y_0 being the height of the water-ethanol interface at $t = 0$ and d being the diffusion length of this quasi-stationary distribution.

Just after the container is filled, a thin mixing layer is present, through which the fraction of alcohol increases, as illustrated on figure (32). The refractive index of the solution increases similarly across the mixing layer, however, liquid mixing also causes a peak in the VGRIN profile $\mu = 0.75$ of higher value than the refractive index of the pure components alone due to the volume contraction of the water-ethanol mixture.

As time passes, diffusion causes the mixing layer to broaden, decreasing the steepness of the VGRIN profile. Initial liquid mixing and diffusion thus strongly affect the VGRIN formed by the nonuniform binary solution.

Note that the VGRIN profile evolves more rapidly during the first hours according to Fick's laws [273] as diffusion lowers the concentration gradient. According to the interdiffusion constant of the two liquids, $D = 1.22 \times 10^{-5} \mathrm{cm^2 s^{-1}}$, the diffusion length d evolves at $d^2 = 4Dt = (4.2[\mathrm{mm}]^2[t]^{-1})t$, where t is measured in hours.

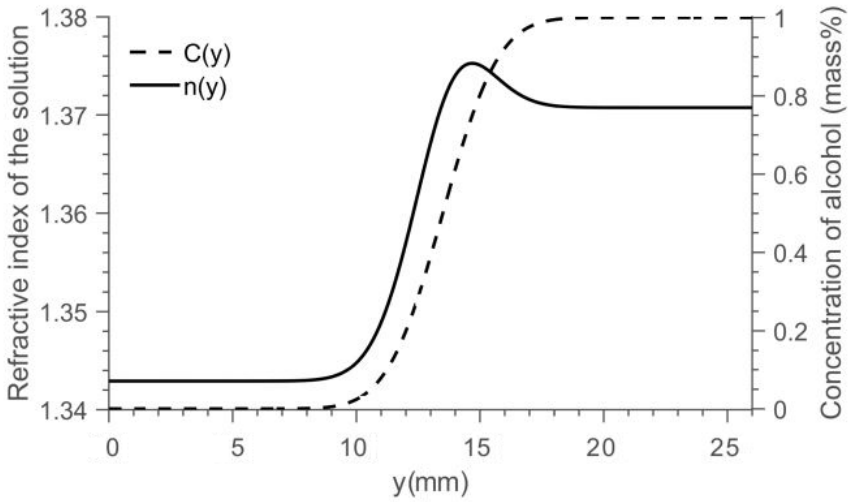

Figure 32 – Ethanol fraction and VGRIN profile of a solution of distilled water and ethanol as function of liquid height for a thin mixing layer ($\mathrm{d}{=}0.25$ cm) for $\lambda{=}405$ nm.

In order to obtain a quasi-stationary VGRIN profile from a binary liquid solution, an adequate timescale should therefore be considered.

In view the above results, for a binary solution of distilled water and alcohol, a stable ($<5\%$ variations) VGRIN profile producing an inferior mirage can be obtained over twenty minutes periods, four hours after the container has been filled.

3.2.3 Numerical ray tracing

The trajectory y(x) of a ray propagating in a known GRIN profile n(y) along the horizontal direction x can be simply deduced from Snell's law, as detailed in work of K. Mamola [274]. Snell's law can be written as $\mathrm{n}\sin(\theta){=}\mathrm{k}$, where k is a constant. When differentiated, Snell's law gives [274]:

$$\frac{\mathrm{dn}}{\mathrm{n}}{=}{-}\cos(\theta)\mathrm{d}\theta \tag{3.18}$$

Where $\cot(\theta){=}\mathrm{dy}/\mathrm{dx}$. The differential $\mathrm{d}\theta$ can be expressed in terms of x and y as [274]:

$$\mathrm{d}\theta{=}{-}\frac{\mathrm{d}^2\mathrm{y}/\mathrm{dx}^2}{1+(\mathrm{dy}/\mathrm{dx})^2}\mathrm{dx} \tag{3.19}$$

The ray trajectory y(x) is thus given by the following ordinary differential equation [274]:

$$\frac{\mathrm{d}^2\mathrm{y}}{\mathrm{dx}^2}{=}\frac{1}{\mathrm{n}}\frac{\mathrm{d}(\mathrm{n})}{\mathrm{dy}}\left[1+\left(\frac{\mathrm{dy}}{\mathrm{dx}}\right)^2\right] \tag{3.20}$$

Alternatively, the ray equation is determined by [274]:

$$\frac{\mathrm{d}^2\mathrm{y}}{\mathrm{dx}^2}{=}\frac{1}{2\mathrm{k}^2}\frac{\mathrm{d}(\mathrm{n}^2)}{\mathrm{dy}} \tag{3.21}$$

Where $\mathrm{k}{=}\mathrm{n}(1+(\mathrm{dy}/\mathrm{dx})^2)^{-1/2}$. Given $\mathrm{y}(0)$, the beam incidence height upon the binary solution and $\mathrm{y}'(0){=}\mathrm{atan}(\theta_0)$, where $\mathrm{k}{=}\mathrm{k}_0{=}\mathrm{nsin}(\theta_0)$, with θ_0 being the beam incidence angle upon the solution, equation (3.21) can be numerically solved. To do so, we use a system of first

order differential equations using the Matlab solver "ode45", which implements a Runge-Kutta iterative method.

For y_0=15.25 mm and θ_0=1.5°, a VGRIN corresponding to a thin mixing layer (15 mn after the cell has been filled) yields two successive total internal reflections, as illustrated on figure (33). As the mixing layer broadens due to diffusion (for a time of 4 hours after the cell has been filled), the magnitude of the beam's deflections diminishes and a single total internal reflection is observed, as illustrated on figure (33).

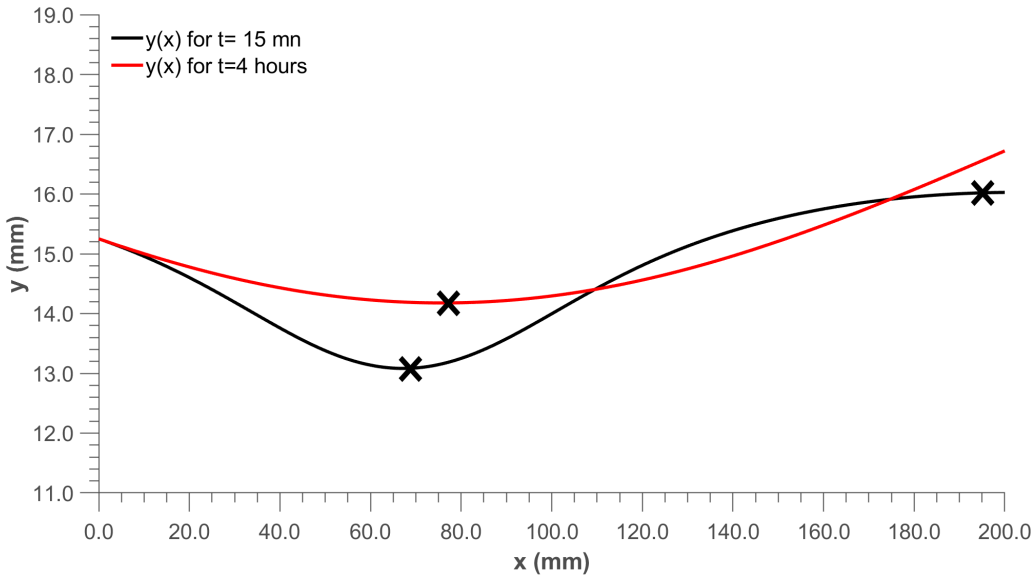

Figure 33 – Ray trajectories in a binary solution of distilled water and ethanol for times corresponding to a thin (t=15 mn) and broader (t=4 hours) mixing layer. For λ=405 nm, y_0=15.25 mm and θ_0=1.5°. Inflection points corresponding to one total internal reflection are indicated by crosses on each curve.

Mirror inversion and astigmatic effects can be evidenced by considering the trajectory of a series of rays, which incident height y_0 is constantly spaced, as illustrated on Figure (34).

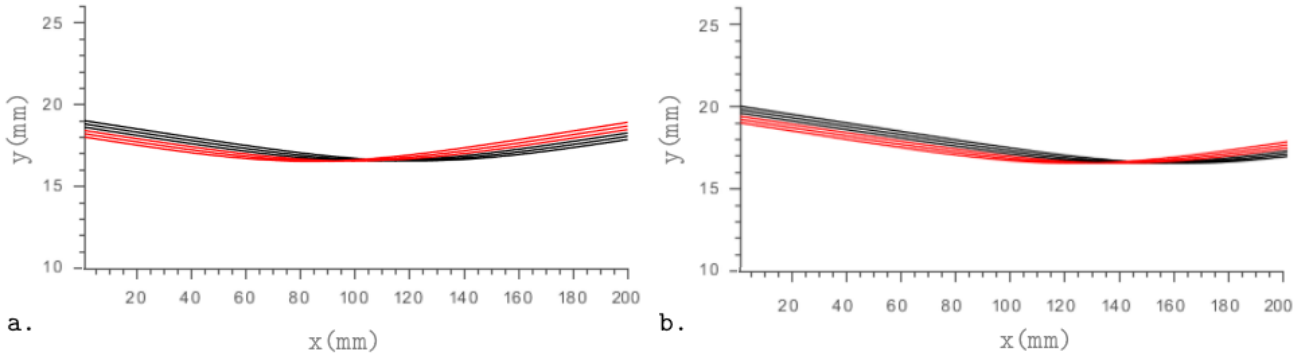

Figure 34 – Ray trajectories in a binary solution of distilled water and ethanol for a series of rays of different incidence height. The colour of the ray distinguishes the upper half of the beam from its lower half. θ_0=1.5°. The incidence height of the upper ray at the cell entrance is y_0=19.0 mm in a. and y_0=20.0 mm in b. The beam diameter has been exaggerated.

For a VGRIN profile corresponding to one total internal reflection and for an incidence

angle $\theta = 1.5°$, figure (34) shows that the VGRIN causes a lensing effect of the beam along the y-direction. This entails variations of the beam diameter in one direction, i.e., the beam becomes astigmatic, and the beam orientation is inverted upon traversing the lens focus plane, i.e., a mirror image will be produced. By varying the beam incidence height while keeping the incidence angle constant, the position of each inflection point for individual rays is varied.

Figure (35) shows the propagation of a series of rays as the incidence height of the leading ray (upper ray at $x = 0$) is increased. Varying the incidence height causes the VGRIN focus plane to migrate towards the cell exit plane, where the CCD camera is placed.

To overcome the limitations of the ray tracing numerical model defined by equation (3.21), we are now developing a complementary numerical model, which will allow to plot the intensity and phase distributions of a paraxial beam carrying OAM when propagating in an inhomogeneous media, for any propagation distance in the media.

This model will be based on the split-step beam propagation method, also known as beam propagation method, as defined in the book of T. Poom and T. Kim [275].

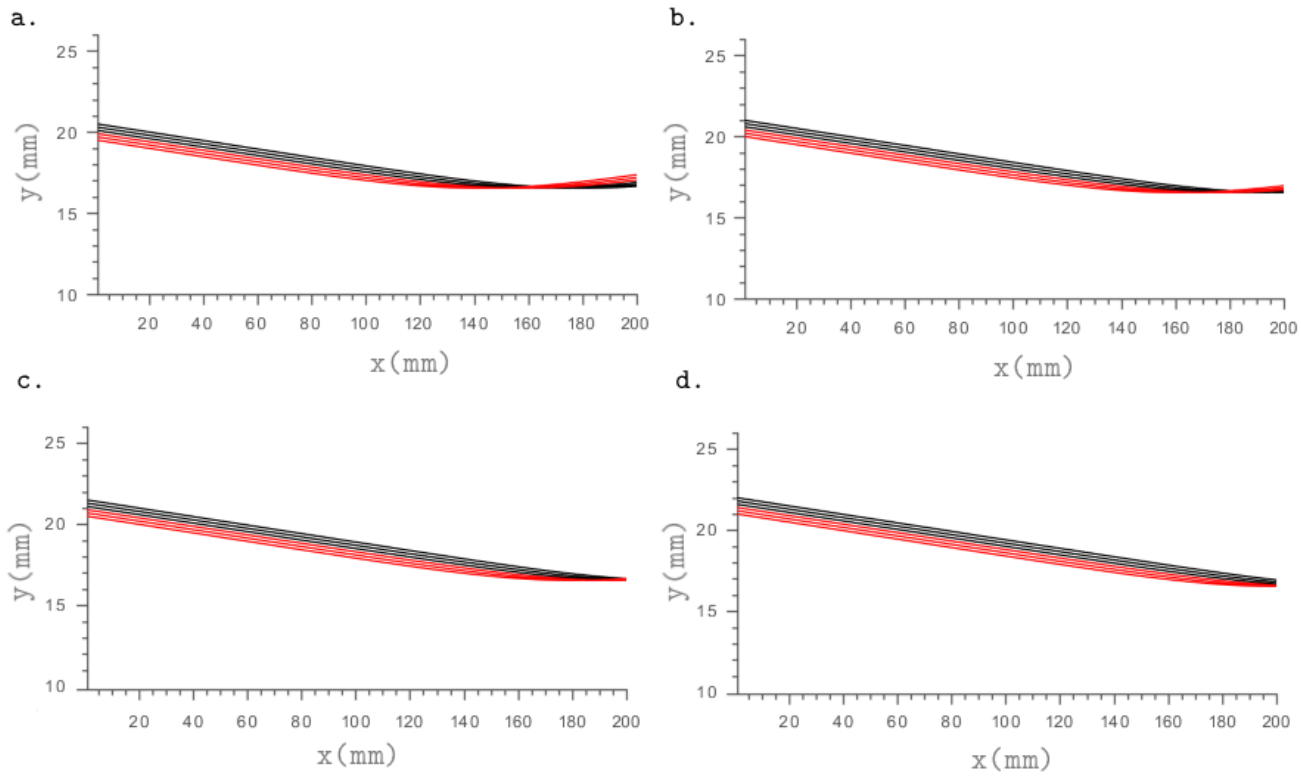

Figure 35 – Translation of the focus plane in a binary solution of distilled water and ethanol for a series of rays for different incidence height. Experimentally, the CCD camera is positioned at the exit of the cell ($x = 200$ mm). The incidence height of the upper ray at the cell entrance is $y_0 = 20.5$ mm in a., $y_0 = 21.0$ mm in b., $y_0 = 21.5$ mm in c. and $y_0 = 22.0$ mm in d. The incidence angle is $\theta_0 = 1.5°$.

3.2.4 Results and discussion

The intensity distributions recorded by the CCD camera, positioned at the exit of the cylindrical cell are summarised in figure (36), for various incidence height and topological charges ranging from $\ell{=}{-}5$ to $\ell{=}{+}5$. The incidence angle is constant $\theta_0{=}3°$ and the VGRIN under consideration allows to witness a single TIR.

For all ℓ, as the incidence height diminishes, the focusing plane associated with the VGRIN migrates closer to the CCD camera, as predicted by figure (35). The height of the CCD camera is progressively lowered to record the beam intensity distribution, in agreement with figure (35). The intensity distribution for an incidence height h_3 on figure (36) corresponds to the situation c. on figure (35).

The exiting beam undergoes astigmatic changes in the vertical dimension, its diameter along the y axis diminishes until the beam reaches the focal plane then increases back beyond this point. A beam exiting the binary solution and having experienced the VGRIN corresponding to one TIR will present astigmatism in relation to the incident beam, except in the situation illustrated on figure, where the rays inflection point is located at the cell center (34 a.).

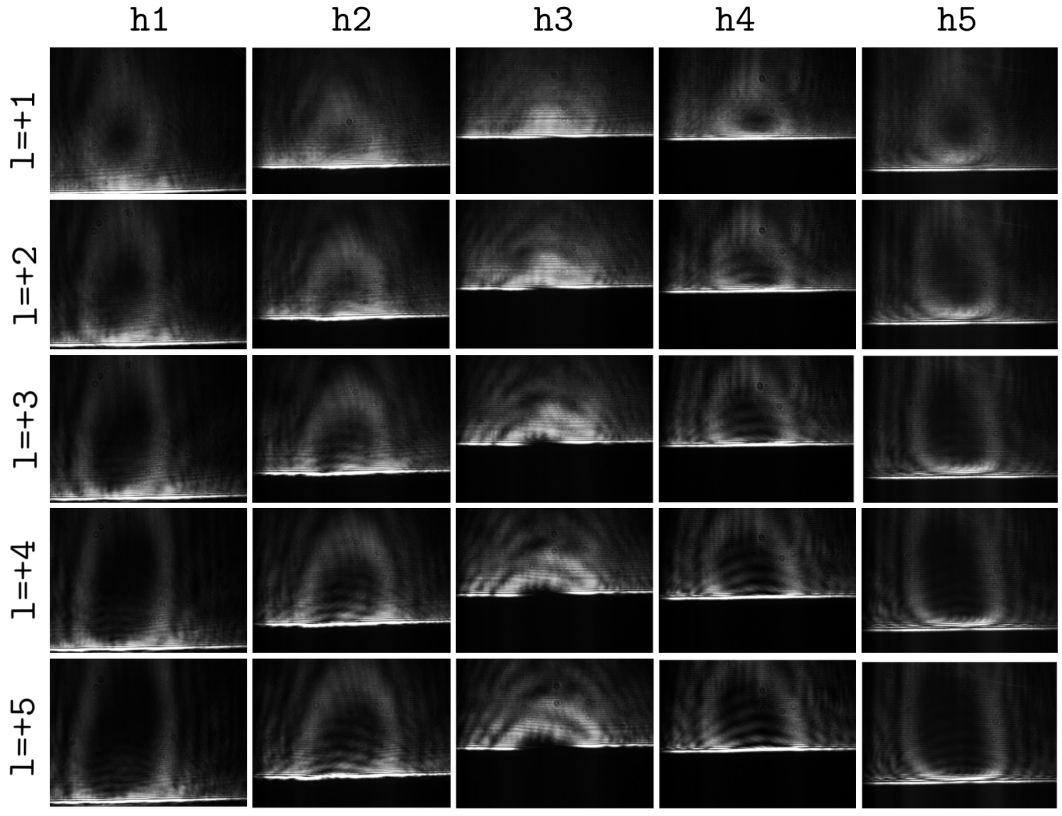

Figure 36 – Intensity distributions of OAM-carrying beams, when exiting an inhomogeneous binary solution of distilled water and ethanol. The beam incidence angle on the binary solution being $\theta_0{=}3°$ for decreasing incident heights denoted $\mathrm{h}_1, \mathrm{h}_2, \mathrm{h}_3, \mathrm{h}_4, \mathrm{h}_5$ and various incident topological charges ℓ. the height of the CCD camera is adjusted to record the beam intensity.

As illustrated on figure (35), the wave-vector distribution of the beam in the cell exit plane varies depending on the beam incidence height, for a constant incidence angle and a quasi-static VGRIN. After exiting the cell, the beam undergoes free propagation, thus, the intensity distribution corresponding to an incident height h_3 on figure (36) and appearing as a superposition of two half beams, can be spatially separated upon free propagation.

The intensity distributions corresponding to an intermediate situation described on figure (35 b. and c.), for an increasing propagation distance after the cell exit plane, are provided on figure (37).

According to figure (35), in c., at the cell exit, the upper part of the incident beam (in black) is not inverted and has a small gradient of wavevector. Upon free propagation, this beam part retains it overall shape and is slightly propagating in the downward direction, as illustrated on figure (37). The lower beam part of the incident beam (in red) however has a larger spread in its local wavevector direction at the cell exit, at c., this beam part still undergoes TIR and, upon propagation, undergoes strong astigmatic changes, as illustrated on figure (37).

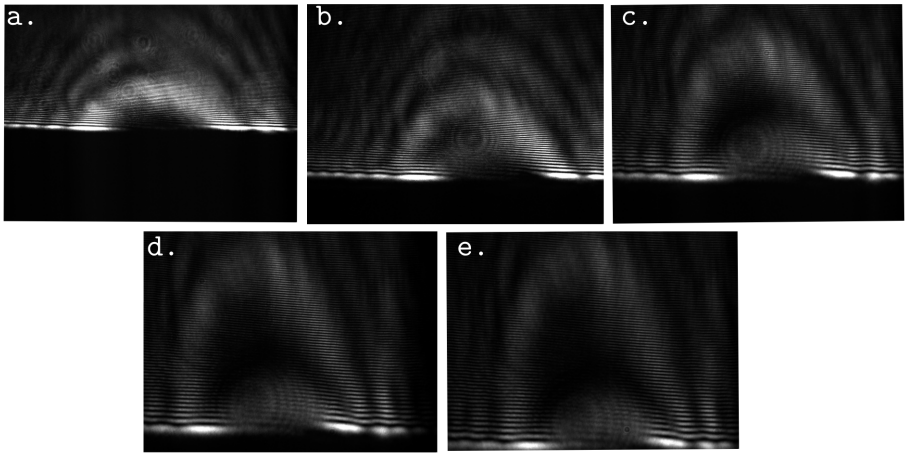

Figure 37 – Intensity distributions for an increasing propagation distance after the cell exit plane. $\mathrm{z}{=}0, 5, 10, 15, 20$ cm for a.,b.,c.,d.,e., respectively, where $\mathrm{z}{=}0$ corresponds to the cell exit plane.

According to figure (35), the full beams corresponding to the intensity distribution for h_1 and h_5 on figure (36) should correspond to mirrored images. Indeed, as the incidence beam experience the VGRIN present in the binary solution, the beam undergoes TIR, producing a mirror inversion of the beam about the vertical direction. As the beam incidence height increases, the deflection point of each individual ray migrates toward the cell exit plane, until only part of the beam undergoes TIR then none of the beam does. Image inversion can easily be verified by gradually obstructing the incident beam while observing its image through the solution.

Image inversions such as the ones produced by TIR are known to reverse the handedness of OAM-carrying beams, and, depending on the beam collimation, can also generate OAM sidebands, degrading the purity of the mode [276]. Dove prisms are capable of such transformation and do exhibit inversion of the beam topological charge [276]. However note that, in the case of a Dove prism, TIR occurs at a sharp interface, it is not the case here.

The handedness and average orbital angular momentum of a beam exiting the binary solution are determined using a tilted lens. The CCD camera is placed near the lens focal plane and records the beam intensity distribution corresponding to a fully inverted and a non-inverted beam. For an incident beam of topological charge $\ell{=}+1$, the difference of axial symmetry in the intensity distribution between a full inverted (figure (38) a.) and a full normal beam (figure (38) b.) indicates that the beams carry topological charges of opposite handedness.

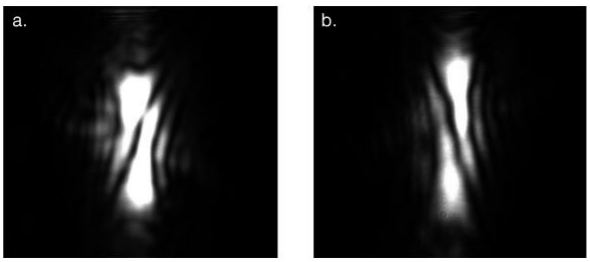

Figure 38 – Intensity distributions near the focal plane of a tilted lens for a full inverted beam (a.) and a full normal beam (b.) exiting a binary solution of ethanol and distilled water, for an incident beam of topological charge $\ell{=}+1$.

Based on the works of G. Molina-Terriza [56, 262], it would be interesting to further investigate mode conversion in the vicinity of the beam "focusing" region. In our case, practical limitations forbid us to record the intensity pattern in this entire region. For this reason, we are now developing a numerical model based on the split-step beam propagation method, which should allow us to study the apparition of the edge dislocation and the trajectory and the evolution of the vortex core, as well as the beam amplitude and phase distributions. We expect a modal decomposition to reveal the passage from a pure LG mode to a superposition of LG modes upon propagation through the VGRIN.

An interesting aspect of the VGRIN profile described above is that it allows, when the rays' deflection points is located near the cell exit plane, to split the beam into a mirrored and a normal part in variable proportions depending on the beam incident height. In terms of OAM, it is rather difficult to compare the OAM content of the individual beam parts as OAM is fully defined for beams with a full azimuthal range. Instead, it would be more interesting to study the whole OAM of the beam, by considering that the beam has been spatially folded. This will have to be investigated in the future.

In all of the above, a single TIR has been considered, allowing to observed an inferior mirage when the beam is partially or totally deflected in the "upward" direction. As illustrated on figure (33), a binary solution of distilled water and ethanol also allows to obtain two consecutive TIR, leading to the observation of the Fata Morgana effect, as illustrated on figure (39).

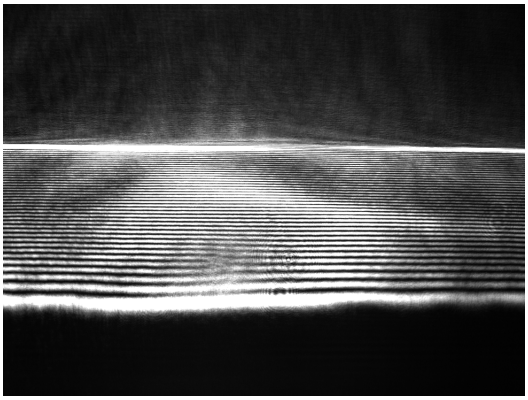

Figure 39 – Intensity distribution at the exit of the cylindrical cell for a VGRIN and incidence conditions leading to the formation of two consecutive TIR

In summary, the inferior mirage of an optical vortex beam carrying OAM has been obtained from a binary solution of distilled water and ethanol. The slow varying VGRIN profile present in the solution was explored to match the mirage propagation conditions. Preliminary results show that the handedness of an optical vortex beam propagating through the solution can be reversed and, depending on the incidence parameters, the beam can be decomposed into a mirrored and normal images. This process is accompanied by astigmatic effects, which role in topological inversion needs to be investigated. We intend to complement our analysis on OAM transformation by a numerical model based on the split-step beam propagation method before submitting our work to publication.

Beyond the scope of our study, nonuniform liquid solutions are versatile in comparison to bulk elements as they can lead to the formation of various VGRIN profiles. This configuration also opens possibilities to study spin-orbit couplings by adding optically active particles or molecules to the binary solution.

CONCLUSIONS

In this thesis, I have sought to provide a concise overview of our current understanding of spin orbit interactions of light and I have presented two original studies on orbit-orbit interactions of light in asymmetric optical beams.

In chapter 1, I have answered the question "what are the spin part and orbital part of light?" by showing that two competing approaches, one based on a symmetric energy-momentum tensor and the other based on gauge-invariant canonical densities, propose fundamentally different definitions. Fortunately, both approaches yield similar qualitative results and, under special circumstances, can even be considered equivalent. In the case of paraxial beams, both approaches agree that the total angular momentum of light can be split into a "spin angular momentum" (SAM) part, associated with the field polarisation, and an "intrinsic orbital angular momentum" (IAOM) part, associated with the phase distribution of the beam. It is also possible, by considering a shift of the beam centroid, to introduce "extrinsic orbital angular momentum" (EOAM), associated with the beam trajectory. Both approaches also agree that in the case of non-paraxial beams, a clear separation of angular momentum into a spin and orbit part is problematic. A few practical considerations regarding optical beams carrying SAM and OAM, with an emphasis on IOAM was also provided, intended to readers unfamiliar with the notion of optical IOAM.

Having laid the foundations for the study of spin-orbit interactions of light, which I define as the mutual conversions between SAM, IOAM and EOAM, I chose, In chapter 2, to describe spin-orbit interactions of light from the perspective of fibre bundle theory. This framework appears naturally when studying the transformation of light beams within a geometric representation and allows to draw analogies with other physical systems. I briefly reviewed a few fundamental concepts about fibre bundle theory, defining a geometric phase as the anholonomy of a fibre bundle and emphasizing the role of the connection and its curvature. I then studied geometric phases acquired by a light beam as its transformation traces a path in the parameter space or (and) in the state space. I showed that specific transformations can lead to spin-orbit interactions of light. I then presented the dynamical effects of the quantum fibre bundle, leading to another manifestation of spin-orbit interactions of light, namely, optical Hall effects.

Having defined spin-orbit interactions of light, in chapter 3, I present two original studies about orbit-orbit interactions of light upon symmetry breaking.

In the first study, an azimuthally symmetrical beam carrying OAM is split into two complementary beam parts using a Fresnel biprism. It is the first time, to my knowledge, that a Fresnel biprism is used to carry out wavefront splitting of a paraxial beam carrying OAM.

This device presents a considerable advantage in comparison with conventional symmetry-breaking configurations such as opaque masks, which is that both beam parts are preserved and propagate in different propagation directions. I interpret the rotation of the asymmetric beam distribution in terms of the Gouy phase of the beam and evidence orbital-dependent deflections, based on experimental and numerical results. Our results are in agreement with previous analytical studies. This work opens new perspectives to the study of asymmetric beams carrying angular momentum, both from a classical and quantum perspective, by allowing to simultaneously study two complementary beam parts. It also brings the question of IOAM to EOAM conversion upon symmetry breaking and invites to further study the question of angular momentum associated with the vortex core and the host beam. Future works should consider weak measurement methods to improve the accuracy on the measurement of the deflections, in particular if spin-dependent reflections are to be investigated.

In the second study, a vertical gradient of refractive index (VGRIN) is used to introduce astigmatism to an azimuthally symmetrical beam carrying OAM. A nonuniform binary solution of distilled water and ethanol is used to realize a VGRIN. In the literature, most graded-index medium preserved a form of cylindrical symmetry, it is not the case here. I show, based on experimental observations supported by a numerical model, that this binary solution forms a VGRIN profile evolving with time, depending on initial liquid mixing and diffusion. I obtained a quasi-static VGRIN profile yielding a single total internal reflection over twenty minutes periods, a time sufficient to investigate the transformation of the incident beam. I show that the VGRIN solution produces a mirror image of the incident beam, resulting in the inversion of the beam topological charge. This process is accompanied by the introduction of astigmatism along the vertical direction. It is possible, by varying the beam incidence condition upon the binary solution, to obtain two beam parts at the exit of the cell, one corresponding to the mirror image and one being the normal image of the incident beam. Numerical ray tracing is used to endorse our results, however, I am now developing a new model based on the split-step beam propagation method in order to further investigate the role of astigmatism in topological charge inversion. According to the literature, this study should evidence OAM mode competition upon mirror inversion. This also brings in discussions about OAM related to the optical vortex core and the host beam. Using a nonuniform binary solution to establish a VGRIN offers a few novel aspects to investigate, first, contrary to most bulk optical elements, mirror inversion does not occur at a sharp interface but occurs smoothly, second, optically active particles or molecules can easily be introduced to the solution.

BIBLIOGRAPHY

[1] J. Kepler. *De cometis libelli tres*. Typis Andreae Apergeri, sumptibus Sebastiani Mylii bibliopolae Augustani, 1619.

[2] C. R. McInnes. *Solar Sailing: Technology, Dynamics and Mission Applications*. Astronomy and Planetary Sciences. Springer, 2004.

[3] J. C. Maxwell. *Treatise on electricity and magnetism*. Clarendon Press, Oxford, UK, 1873.

[4] J. H. Poynting. On the transfer of energy in the electromagnetic field. *Phil. Trans. Roy. Soc. London*, (175):343, 1884.

[5] J. J. Thomson. *Notes on Recent Researches in Electricity and Magnetism: Intended as a Sequel to Professor Clerk-Maxwell's Treatise on Electricity and Magnetism*. Cambridge University Press, Cambridge, UK, 2010.

[6] H. Poincaré. Théorie de Lorentz et le principe de la réaction. *Archives Néerlandaises des Sciences exactes et naturelles*, (5):252, 1900.

[7] P. Lebedev. *Untersuchungen über die Druckkräfte des Lichtes*. Annalen der Physik, 311 (11): 433–458, 1901.

[8] E.F. Nichols and G.F. Hull. A preliminary communication on the pressure of heat and light radiation. *Phys. Rev.*, 13:307–320, 1901.

[9] J. H. Poynting. The wave-motion of a revolving shaft, and a suggestion as to the angular momentum in a beam of circularly-polarized light. *Proc. R. Soc. Lond. A*, (82):560–567, 1909.

[10] R. Beth. Mechanical detection and measurement of the angular momentum of light. *Phys. Rev.*, 50:115–125, 1936.

[11] C. G. Darwin. Notes on the theory of radiation. *Proc. R. Soc. Lond. A*, (136):36–52, 1932.

[12] E. Abramochkin and V. Volostnikov. Beam transformations and nontransformed beams. *Optics Communications*, 83(1):123 – 135, 1991.

[13] L. Allen, M. W. Beijersbergen, R. J. C. Spreeuw, and J. P. Woerdman. Orbital angular-momentum of light and the transformation of Laguerre–Gaussian laser modes. *Phys. Rev. A*, 45:8185–8189, 1992.

[14] V. Garcés-Chávez, D. McGloin, M. J. Padgett, W. Dultz, H. Schmitzer, and K. Dholakia. Observation of the transfer of the local angular momentum density of a multiringed light beam to an optically trapped particle. *Phys. Rev. Lett.*, 91:093602, 2003.

[15] K. Y. Bliokh, M. A Alonso, E. A. Ostrovskaya, and A. Aiello. Angular momenta and spin-orbit interaction of nonparaxial light in free space. *Phys. Rev. A*, 82:063825, 2010.

[16] K. Y. Bliokh, F. J. Rodríguez-Fortuño, F. Nori, and A. V. Zayats. Spin-orbit interactions of light. *Nat. Photonics*, 9:796, 2015.

[17] E. Leader. The photon angular momentum controversy: Resolution of a conflict between laser optics and particle physics. *Phys. Lett. B*, 756:303 – 308, 2016.

[18] S. M. Barnett. Rotation of electromagnetic fields and the nature of optical angular momentum. *J. Mod. Opt.*, 57(14-15):1339–1343, 2010.

[19] S. M. Barnett, L. Allen, R. P. Cameron, C. R. Gilson, M. J. Padgett, F. C. Speirits, and A. M. Yao. On the natures of the spin and orbital parts of optical angular momentum. *J. Opt.*, 18(6):064004, 2016.

[20] K. Y. Bliokh. Geometrodynamics of polarized light: Berry phase and spin Hall effect in a gradient-index medium. *J. Opt. A*, 11(9):094009, 2009.

[21] K. Bliokh. Geometrical optics of beams with vortices: Berry phase and orbital angular momentum hall effect. *Phys. Rev. Lett.*, 97:043901, 2006.

[22] F. Wilczek and A. Shapere. *Geometric Phases in Physics*. Advanced series in mathematical physics. World Scientific, 1989.

[23] V.G. Fedoseyev. Spin-independent transverse shift of the centre of gravity of a reflected and of a refracted light beam. *Opt. Commun.*, 193(1):9 – 18, 2001.

[24] A. Aiello, N. Lindlein, C. Marquardt, and G. Leuchs. Transverse angular momentum and geometric spin Hall effect of light. *Phys. Rev. Lett.*, 103:100401, 2009.

[25] E. Noether. Invariante variationsprobleme. *Achrichten von der Gesellschaft der Wissenschaften zu Göttingen Mathematisch-Physikalische Klasse*, 1918:235–257, 1918.

[26] H. Kleinert. *Particles and Quantum Fields*. World Scientific, Singapore, 2016.

[27] Y. K. Bliokh, J. Dressel, and F. Nori. Conservation of the spin and orbital angular momenta in electromagnetism. *New J. Phys*, 16:093037, 2014.

[28] I. Bialynicki-Birula. The photon wave function. 36:245 – 294, 1996.

[29] S. J. Van Enk and G. Nienhuis. Spin and orbital angular momentum of photons. *EPL*, 25(7):497, 1994.

[30] S. J. Van Enk and G. Nienhuis. Eigenfunction description of laser beams and orbital angular momentum of light. *Opt. Commun.*, 94(1):147 – 158, 1992.

[31] S. J. Van Enk and G. Nienhuis. Commutation rules and eigenvalues of spin and orbital angular momentum of radiation fields. *J. Mod. Opt.*, 41(5):963–977, 1994.

[32] J. B. Götte, S. Franke-Arnold, R. Zambrini, and S. M. Barnett. Quantum formulation of fractional orbital angular momentum. *J. Mod. Opt.*, 54(12):1723–1738, 2007.

[33] J. D. Jackson. *Classical electrodynamics*. Wiley, New York, NY, 3rd ed. edition, 1999.

[34] D. J. Griffiths. *Introduction to electrodynamics*. Pearson, Boston, 4th ed. edition, 2013.

[35] S. M. Barnett and L. Allen. Orbital angular momentum and nonparaxial light beams. *Opt. Commun.*, 110(5):670 – 678, 1994.

[36] A. Bekshaev, K. Y. Bliokh, and M. Soskin. Internal flows and energy circulation in light beams. *J. Opt.*, 13(5):13:32, 2011.

[37] S. M. Barnett. Optical angular-momentum flux. *J. Opt.*, 4(2):S7, 2002.

[38] C. Cohen-Tannoudji, J. Dupont-Roc, and G. Grynberg. *Photons and Atoms*. Wiley, New York, 1989.

[39] X.C. Chen, X.F Lü, W.M. Sun, W. Fan, and T. Goldman. Spin and orbital angular momentum in gauge theories: Nucleon spin structure and multipole radiation revisited. *Phys. Rev. Lett.*, 100:232002, 2008.

[40] E. Leader and C. Lorce. The angular momentum controversy: What's it all about and does it matter? *Phys. Rep.*, (541):163–248, 2014.

[41] K. Y. Bliokh and F. Nori. Transverse and longitudinal angular momenta of light. *Phys. Rep.*, 592:1–38, 2015.

[42] E. Leader. A proposed measurement of optical orbital and spin angular momentum and its implications for photon angular momentum. *Phys. Lett. B*, 779:385 – 387, 2018.

[43] X. B. Chen and X. S. Chen. Energy-momentum tensor is nonsymmetric for spin-polarized photons. *ArXiv e-prints*, 2012.

[44] D. P. Ghai, P. Senthilkumaran, and R.S. Sirohi. Single-slit diffraction of an optical beam with phase singularity. *Opt. Las. Eng.*, 47(1):123 – 126, 2009.

[45] M. Antognozzi, C. R Bermingham, R. L. Harniman, S. Simpson, J. Senior, R. Hayward, and H. Hoerber. Direct measurements of the extraordinary optical momentum and transverse spin-dependent force using a nano-cantilever. *Nat. Phys.*, 12:731–735, 2016.

[46] R. Mir, J. S. Lundeen, M. W. Mitchell, A. M. Steinberg, J. L. Garretson, and H. M. Wiseman. A double-slit 'which-way' experiment on the complementarity–uncertainty debate. *New J. Phys.*, 9(8):287, 2007.

[47] S. Kocsis, B. Braverman, S. Ravets, M. J. Stevens, R. P. Mirin, L. K. Shalm, and A. M. Steinberg. Observing the average trajectories of single photons in a two-slit interferometer. *Science*, 332(6034):1170–1173, 2011.

[48] S. M. Barnett and M. V. Berry. Superweak momentum transfer near optical vortices. *J. Opt.*, 15(12):125701, 2013.

[49] C. N. Alexeyev, Y. A. Fridman, and A. N. Alexeyev. Spin continuity and birefringence in locally isotropic weakly inhomogeneous media. 4403:71–81, 2001.

[50] M. Mazilu. Spin and angular momentum operators and their conservation. *J. Opt. A*, 11(9):094005, 2009.

[51] S. M. Barnett, R. P. Cameron, and A. M. Yao. Duplex symmetry and its relation to the conservation of optical helicity. *Phys. Rev. A*, 86:013845, 2012.

[52] K. Y. Bliokh, A. Y. Bekshaev, and F. Nori. Optical momentum, spin, and angular momentum in dispersive media. *Phys. Rev. Lett.*, 119:073901, 2017.

[53] D. Goldstein and D.H. Goldstein. *Polarized Light, Revised and Expanded*. Optical engineering. CRC Press, 2003.

[54] I. Freund. Critical point explosions in two-dimensional wave fields. *Opt. Commun.*, 159(1):99 – 117, 1999.

[55] P. Coullet, L. Gil, and F. Rocca. Optical vortices. *Opt. Commun.*, 73(5):403 – 408, 1989.

[56] D. L. Andrews and M. Babiker. *The Angular Momentum of Light*. Cambridge University Press, 2013.

[57] J. Leach, E. Yao, and M. J. Padgett. Observation of the vortex structure of a non-integer vortex beam. *New J. Phys.*, 6(1):71, 2004.

[58] D. Preece1 F. Flossmann S. Franke-Arnold S. M. Barnett J. B. Gotte, K. O. Holleran and M. J. Padgett. Light beams with fractional orbital angular momentum and their vortex structure. *Opt. Express*, 16(2):993, 2008.

[59] M. V. Berry, J. F. Nye, and F. J. Wright. The elliptic umbilic diffraction catastrophe. 291(1382):453–484, 1979.

[60] H. Wolter. Untersuchungen zur strahlversetzung bei totalreflexion des lichtes mit der methode der minimumstrahlkennzeichnung. *Natureforschung*, (5a):143–153, 1950.

[61] W W. Braunbek and G. Laukien. Einzelheiten zur halbebenen-beugung. *Optik*, 9:174–179, 1952.

[62] M. R. Dennis, K. O. Holleran, and M. J. Padgett. Optical vortices and polarization singularities. volume 53 of *Progress in Optics*, pages 293 – 363. Elsevier, 2009.

[63] J. Leach, M. R. Dennis, J. Courtial, and M. J. Padgett. Knotted threads of darkness. *Nature*, 432:165, 2004.

[64] F. S. Roux. Coupling of noncanonical optical vortices. *J. Opt. Soc. Am. B*, 21(3):664–670, 2004.

[65] V. V. Kotlyar, A. A. Kovalev, and A. P. Porfirev. *Vortex Laser Beams*. CRC Press, 2018.

[66] J.M. Vaughan and D.V. Willetts. Interference properties of a light beam having a helical wave surface. *Opt. Commun.*, 30(3):263 – 267, 1979.

[67] Chr. Tamm and C. O. Weiss. Bistability and optical switching of spatial patterns in a laser. *J. Opt. Soc. Am. B*, 7(6):1034–1038, 1990.

[68] G. Nienhuis and L. Allen. Paraxial wave optics and harmonic oscillators. *Phys. Rev. A*, 48:656–665, 1993.

[69] D. McGloin, N. B. Simpson, and M. J. Padgett. Transfer of orbital angular momentum from a stressed fiber-optic waveguide to a light beam. *Appl. Opt.*, 37(3):469–472, 1998.

[70] M.W. Beijersbergen, R.P.C. Coerwinkel, M. Kristensen, and J.P. Woerdman. Helical-wavefront laser beams produced with a spiral phaseplate. *Opt. Commun.*, 112(5):321 – 327, 1994.

[71] V.Yu. Bazhenov, M.S. Soskin, and M.V. Vasnetsov. Screw dislocations in light wavefronts. *J. Mod. Opt.*, 39(5):985–990, 1992.

[72] A.Ya. Bekshaev and A.I. Karamoch. Spatial characteristics of vortex light beams produced by diffraction gratings with embedded phase singularity. *Opt. Commun.*, 281(6):1366 – 1374, 2008.

[73] E. Karimi, G. Zito, B. Piccirillo, L. Marrucci, and E. Santamato. Hypergeometric-gaussian modes. *Opt. Lett.*, 32(21):3053–3055, 2007.

[74] E. Bolduc, N. Bent, E. Santamato, E. Karimi, and R. W. Boyd. Exact solution to simultaneous intensity and phase encryption with a single phase-only hologram. *Opt. Lett.*, 38(18):3546–3549, 2013.

[75] T. Ando, Y. Ohtake, N. Matsumoto, T. Inoue, and N. Fukuchi. Mode purities of Laguerre-Gaussian beams generated via complex amplitude modulation using phase-only spatial light modulators. *Opt. Lett.*, 34(1):34–36, 2009.

[76] M. D Williams, M. M. Coles, D. S. Bradshaw, and D. L. Andrews. Direct generation of optical vortices. *Phys. Rev. A*, 89:033837, 2014.

[77] J. Hartmann. Bemerkungen über den Bau und die Justirung von Spektrographen. *Zeitschrift Für Instrumentenkunde*, 20:17–58, 1900.

[78] Z. Wang, Z. Zhang, and Q. Lin. A novel method to determine the helical phase structure of Laguerre–Gaussian beams. *J. Opt. A*, 11(8):085702, 2009.

[79] H. I. Sztul and R. R. Alfano. Double-slit interference with Laguerre-Gaussian beams. *Opt. Lett.*, 31(7):999–1001, 2006.

[80] P. H. F. Mesquita, A. J. Jesus-Silva, E. J. S. Fonseca, and J. M. Hickmann. Engineering a square truncated lattice with light's orbital angular momentum. *Opt. Express*, 19(21):20616–20621, 2011.

[81] J. Arlt. Handedness and azimuthal energy flow of optical vortex beams. *J. Mod. Opt.*, 50(10):1573–1580, 2003.

[82] P. Vaity, J. Banerji, and R.P. Singh. Measuring the topological charge of an optical vortex by using a tilted convex lens. *Phys. Lett. A*, 377(15):1154 – 1156, 2013.

[83] O. Bryngdahl. Geometrical transformations in optics. *J. Opt. Soc. Am.*, 64(8):1092–1099, 1974.

[84] P. G. Kwiat, A. G. White, J. R. Mitchell, O. Nairz, G. Weihs, H. Weinfurter, and A. Zeilinger. High-efficiency quantum interrogation measurements via the quantum Zeno effect. *Phys. Rev. Lett.*, 83:4725–4728, 1999.

[85] L. Allen and M. Padgett. *The Orbital Angular Momentum of Light*, pages 1–12. Wiley-Blackwell, 2011.

[86] M. J. Padgett, J. E. Molloy, and D. McGloin. *Optical Tweezers. Methods and Applications*. Taylor and Francis Group, Boca Raton London New York, 2010.

[87] K. Toyoda, F. Takahashi, S. Takizawa, Y. Tokizane, K. Miyamoto, R. Morita, and T. Omatsu. Transfer of light helicity to nanostructures. *Phys. Rev. Lett.*, 110:143603, 2013.

[88] B. Wetzel, C. Xie, P. A. Lacourt, J. M. Dudley, and F. Courvoisier. Femtosecond laser fabrication of micro and nano-disks in single layer graphene using vortex bessel beams. *Appl. Phys. Lett.*, 103(24):241111, 2013.

[89] L. Torner, J. P. Torres, and S. Carrasco. Digital spiral imaging. *Opt. Express*, 13(3):873–881, 2005.

[90] S. Fürhapter, A. Jesacher, S. Bernet, and M. Ritsch-Marte. Spiral phase contrast imaging

in microscopy. *Opt. Express*, 13(3):689–694, 2005.

[91] B. Jack, J. Leach, J. Romero, S. Franke-Arnold, M. Ritsch-Marte, S. M. Barnett, and M. J. Padgett. Holographic ghost imaging and the violation of a Bell inequality. *Phys. Rev. Lett.*, 103:083602, 2009.

[92] A. Aleksanyan, N. Kravets, and E. Brasselet. Multiple-star system adaptive vortex coronagraphy using a liquid crystal light valve. *Phys. Rev. Lett.*, 118:203902, 2017.

[93] G. Molina-Terriza, J. P. Torres, and L. Torner. Management of the angular momentum of light: Preparation of photons in multidimensional vector states of angular momentum. *Phys. Rev. Lett.*, 88:013601, 2001.

[94] S. Franke-Arnold, S. M. Barnett, E. Yao, J. Leach, J. Courtial, and M. Padgett. Uncertainty principle for angular position and angular momentum. *New J. Phys.*, 6(1):103, 2004.

[95] K. Dholakia, N. B. Simpson, M. J. Padgett, and L. Allen. Second-harmonic generation and the orbital angular momentum of light. *Phys. Rev. A*, 54:R3742–R3745, 1996.

[96] A. Berzanskis, A. Matijosius, A. Piskarskas, V. Smilgevicius, and A. Stabinis. Conversion of topological charge of optical vortices in a parametric frequency converter. *Opt. Commun.*, 140(4):273 – 276, 1997.

[97] D. P. Caetano, M. P. Almeida, P. H. Souto Ribeiro, J. A. O. Huguenin, B. Coutinho dos Santos, and A. Z. Khoury. Conservation of orbital angular momentum in stimulated down-conversion. *Phys. Rev. A*, 66:041801, 2002.

[98] G. A. Swartzlander and C. T. Law. Optical vortex solitons observed in Kerr nonlinear media. *Phys. Rev. Lett.*, 69:2503–2506, 1992.

[99] H. Rubinsztein-Dunlop, A. Forbes, M. V. Berry, M. R. Dennis, D. L. Andrews, M. Mansuripur ..., and A. M Weiner. Roadmap on structured light. *J. Opt.*, 19(1):013001, 2016.

[100] Q. Zhan. Cylindrical vector beams: from mathematical concepts to applications. *Adv. Opt. Photon.*, 1(1):1–57, 2009.

[101] I. Freund. Cones, spirals, and mobius strips, in elliptically polarized light. *Opt. Commun.*, 249:7–22, 2005.

[102] E. J. Galvez, I. Dutta, K. Beach, J. J. Zeosky, J. A. Jones, and B. Khajavi. Multitwist möbius strips and twisted ribbons in the polarization of paraxial light beams. *Sc. Rep.*, 7(1):13653, 2017.

[103] M V Berry. Optical currents. *J. Opt. A*, 11:094001, 2009.

[104] J. F. Nye. Lines of circular polarization in electromagnetic wave fields. *Proc. Royal Soc.*, 389(1797):279–290, 1983.

[105] D. L. Andrews. *Fundamentals of photonics and physics, Volume 1*. John Wiley and Sons, Inc., Hoboken, New Jersey, 2015.

[106] I. Freund. Polarization singularity indices in gaussian laser beams. *Opt. Commu.*, 201(4):251 – 270, 2002.

[107] K. Y. B., A. Niv, V. Kleiner, and E. Hasman. Singular polarimetry: Evolution of polariza-

tion singularities in electromagnetic waves propagating in a weakly anisotropic medium. *Opt. Express*, 16(2):695–709, 2008.

[108] F. Flossmann, U. T. Schwarz, M. Maier, and M. R. Dennis. Stokes parameters in the unfolding of an optical vortex through a birefringent crystal. *Opt. Express*, 14(23):11402–11411, 2006.

[109] D. Pohl. Operation of a ruby laser in the purely transverse electric mode TE01. *App. Phys. Lett.*, 20(7):266–267, 1972.

[110] K. Yonezawa, Y. Kozawa, and S. Sato. Generation of a radially polarized laser beam by use of the birefringence of a c-cut Nd:YVO4 crystal. *Opt. Lett.*, 31(14):2151–2153, 2006.

[111] V. G. Niziev, R. S. Chang, and A. V. Nesterov. Generation of inhomogeneously polarized laser beams by use of a Sagnac interferometer. *Appl. Opt.*, 45(33):8393–8399, 2006.

[112] G. Machavariani, Y. Lumer, I. Moshe, A. Meir, and S. Jackel. Spatially-variable retardation plate for efficient generation of radially- and azimuthally-polarized beams. *Opt. Commun.*, 281(4):732 – 738, 2008.

[113] R. Yamaguchi, T. Nose, and S. Sato. Liquid crystal polarizers with axially symmetrical properties. *Jap. J. App. Phys.*, 28(Part 1, No. 9):1730–1731, 1989.

[114] T Grosjean, D Courjon, and M Spajer. An all-fiber device for generating radially and other polarized light beams. *Opt. Commun.*, 203(1):1 – 5, 2002.

[115] G. Volpe and D. Petrov. Generation of cylindrical vector beams with few-mode fibers excited by Laguerre–Gaussian beams. *Opt. Commun.*, 237(1):89 – 95, 2004.

[116] S Quabis, R Dorn, M Eberler, O Glöckl, and G Leuchs. Focusing light to a tighter spot. *Opt. Commu.*, 179(1):1 – 7, 2000.

[117] D. P. Biss, K. S. Youngworth, and T. G. Brown. Dark-field imaging with cylindrical-vector beams. *Appl. Opt.*, 45(3):470–479, 2006.

[118] H. Kawauchi, K. Yonezawa, Y. Kozawa, and S. Sato. Calculation of optical trapping forces on a dielectric sphere in the ray optics regime produced by a radially polarized laser beam. *Opt. Lett.*, 32(13):1839–1841, 2007.

[119] V G Niziev and A V Nesterov. Influence of beam polarization on laser cutting efficiency. *J. Phys. D*, 32(13):1455–1461, 1999.

[120] H. Kano, S. Mizuguchi, and S. Kawata. Excitation of surface-plasmon polaritons by a focused laser beam. *J. Opt. Soc. Am. B*, 15(4):1381–1386, 1998.

[121] S. Barnett. *Quantum Information*. Oxford University Press, Inc., 2009.

[122] P. R. S. Gomes. Polarization of electron and photon beams. *Rev. Bras. Fis.*, 11:4, 1981.

[123] H. Lyre. Berry phase and quantum structure. *Studies in History and Philosophy of Science Part B: Studies in History and Philosophy of Modern Physics*, 48:45 – 51, 2014.

[124] F. Bloch. Nuclear induction. *Phys. Rev.*, 70(7-8):460–474, 1946.

[125] A. M. Yao and M. J. Padgett. Orbital angular momentum: origins, behavior and applications. *Adv. Opt. Photonics*, 3:161–204, 2011.

[126] M.W. Beijersbergen, L. Allen, H.E.L.O. van der Veen, and J.P. Woerdman. Astigmatic

laser mode converters and transfer of orbital angular momentum. *Opt. Commun.*, 96(1):123 – 132, 1993.

[127] G. S. Agarwal. SU(2) structure of the Poincaré sphere for light beams with orbital angular momentum. *J. Opt. Soc. Am. A*, 16(12):2914–2916, 1999.

[128] M. J. Padgett and J. Courtial. Poincaré-sphere equivalent for light beams containing orbital angular momentum. *Opt. Lett.*, 24(7):430–432, 1999.

[129] G. Milione, H. I. Sztul, D. A. Nolan, and R. R. Alfano. Higher-order Poincaré sphere, Stokes parameters, and the angular momentum of light. *Phys. Rev. Lett.*, 107:053601, 2011.

[130] Pérola Milman. Phase dynamics of entangled qubits. *Phys. Rev. A*, 73:062118, Jun 2006.

[131] C. E. R. Souza, J. A. O. Huguenin, P. Milman, and A. Z. Khoury. Topological phase for spin-orbit transformations on a laser beam. *Phys. Rev. Lett.*, 99:160401, Oct 2007.

[132] M. Berry. Anticipations of the geometric phase. *Phys. Today*, 43:34–40, 1990.

[133] M. V. Berry. Quantal phase factors accompanying adiabatic changes. *Proc. R. Soc. Lond. A*, 392(1802):45–57, 1984.

[134] J. Samuel and R. Bhandari. General setting for Berry's phase. *Phys. Rev. Lett.*, (60):2339, 1988.

[135] A. Uhlmann. Parallel transport and quantum holonomy along density operators. *Rep. Math. Phys*, 24(2):229 – 240, 1986.

[136] Frank Wilczek and A. Zee. Appearance of gauge structure in simple dynamical systems. *Phys. Rev. Lett.*, 52:2111–2114, 1984.

[137] B. Simon. Holonomy, the quantum adiabatic theorem, and Berry's phase. *Phys. Rev. Lett.*, 51:2167–2170, 1983.

[138] E. Malek. Topology and geometry for physicists. *PoS*, Modave 2017:002, 2018.

[139] T.D. Stanescu. *Introduction to Topological Quantum Matter & Quantum Computation*. CRC Press, Taylor & Francis Group, 2017.

[140] N. Mukunda and R. Simon. Quantum kinematic approach to the geometric phase. *Annals of Physics*, 228(2):205 – 268, 1993.

[141] S. Ganguli. Fibre bundles and gauge theories in classical physics: a united description of falling cats, magnetic monopoles and Berry's phase. 2008.

[142] R. Montgomery. Gauge theory of the falling cat. *Fields Inst. Commun.*, 1, 1993.

[143] J W Zwanziger, M Koenig, and A Pines. Berry's phase. *Annu. Rev. Phys. Chem.*, 41(1):601–646, 1990.

[144] Jens Von Bergmann, Von Hsingchi, and Hsingchi Bergmann. Foucault pendulum through basic geometry. *American Journal of Physics - AMER J PHYS*, 75, 10 2007.

[145] Y. Aharonov and J. Anandan. Phase change during a cyclic quantum evolution. *Phys. Rev. Lett.*, 58:1593–1596, 1987.

[146] A. Bohm, L. J. Boya, and B. Kendrick. On the uniqueness of the Berry connection. *J. Math. Phys.*, 33(7):2528–2532, 1992.

[147] D. M. Tong, E. Sjöqvist, L. C. Kwek, and C. H. Oh. Kinematic approach to the mixed state geometric phase in nonunitary evolution. *Phys. Rev. Lett.*, 93:080405, Aug 2004.

[148] R. Y. Chiao and Y. S. Wu. Manifestations of Berry's topological phase for the photon. *Phys. Rev. Lett.*, 57:933–936, 1986.

[149] A. Tomita and R. Y. Chiao. Observation of Berry's topological phase by use of an optical fiber. *Phys. Rev. Lett.*, 57:937–940, 1986.

[150] T. F. Jordan. Berry phases and unitary transformations. *J. Math. Phys.*, 29(9):2042–2052, 1988.

[151] S M Rytov. On the transition from wave to geometric optics. *Dokl. Akad. Nauk USSR*, 18(263), 1938.

[152] V. V. Vladimirskii. *Dokl. Akad. Nauk USSR*, 31(222), 1941.

[153] Y Q Cai, G Papini, W R Wood, and S R Valluri. On the classical origin of Berry's phase for photons. *J. Eur. Opt. Soc.*, 1(1):49–52, 1989.

[154] E.J Galvez, M.R Cheyne, J.B Stewart, C.D Holmes, and H.I Sztul. Variable geometric-phase polarization rotators for the visible. *Opt. Commun.*, 171(1-3):7–13, 1999.

[155] R. Armis, Z. M Mansuripur, and E. M. Wright. Spin and orbital angular momenta of light reflected from a cone. *Phys rev. A.*, 84:033813, 2011.

[156] M. Kitano, T. Yabuzaki, and T. Ogawa. Comment on "observation of Berry's topological phase by use of an optical fiber". *Phys. Rev. Lett.*, 58:523–523, 1987.

[157] Enrique J. Galvez and Chris D. Holmes. Geometric phase of optical rotators. *J. Opt. Soc. Am. A*, 16(8):1981–1985, 1999.

[158] J. Courtial, K. Dholakia, D. A. Robertson, L. Allen, and M. J. Padgett. Measurement of the rotational frequency shift imparted to a rotating light beam possessing orbital angular momentum. *Phys. Rev. Lett.*, 80:3217–3219, 1998.

[159] S Pancharatnam. Generalized theory of interference and its applications - part ii. partially coherent pencils. *Proceedings of The Indian Academy of Sciences-mathematical Sciences - PROC INDIAN ACAD SCI-MATH SCI*, 44:398–417, 12 1956.

[160] S. Pancharatnam. Generalized theory of interference and its applications. *Proc. Indian Acad. Sci.*, 44, 1956.

[161] D. Pescetti. Interference between elliptically polarized light beams. *A. J. Phys.*, 40(5):735–740, 1972.

[162] C. V. S. Borges, M. Hor-Meyll, J. A. O. Huguenin, and A. Z. Khoury. Bell-like inequality for the spin-orbit separability of a laser beam. *Phys. Rev. A*, 82:033833, Sep 2010.

[163] N. Mukunda, S. Chaturvedi, and R. Simon. Classical light beams and geometric phases. *J. Opt. Soc. Am. A*, 31(6):1141–1157, Jun 2014.

[164] H. G. Jekrard. Transmission of light through birefringent and optically active media: the Poincaré sphere. *J. Opt. Soc. Am.*, 44(8):634–640, 1954.

[165] R. Bhandari. Polarization of light and topological phases. *Phys. Rep.*, 281(1):1 – 64, 1997.

[166] J. Lages, R. Giust, and J. M. Vigoureux. Geometric phase and Pancharatnam phase induced by light wave polarization. *Physica E: Low-dimensional Systems and Nanostructures*, 59:6 – 14, 2014.

[167] D. A. Smirnova, V. M. Travin, K. Y. Bliokh, and F. Nori. Relativistic spin-orbit interactions of photons and electrons. *Phys. Rev. A.*, 97(4), 2018.

[168] K. Y. Bliokh and F. Nori. Spatio-temporal vortex beams and angular momentum. *Phys. Rev. A*, 86:033824, 2012.

[169] B. A. Garetz and S. Arnold. Variable frequency shifting of circularly polarized laser radiation via a rotating half-wave retardation plate. *Opt. Commun.*, 31(1):1 – 3, 1979.

[170] Z. Bomzon, V. Kleiner, and E. Hasman. Formation of radially and azimuthally polarized light using space-variant subwavelength metal stripe gratings. *App. Phys. Lett.*, 79(11):1587–1589, 2001.

[171] L. Marrucci, C. Manzo, and D. Paparo. Optical spin-to-orbital angular momentum conversion in inhomogeneous anisotropic media. *Phys. Rev. Lett.*, 96:163905, 2006.

[172] F. Liu S. Zhang X. Yin S. Xiao, J. Wang and J. Li. Spin-dependent optics with metasurfaces. *Nanophotonics*, (6(1)):215–234, 2017.

[173] E. Galvez. Applications of geometric phase in optics. 2019.

[174] P. F. Chimento, P. F. A. Alkemade, G. W. Hooft, and E. R. Eliel. Optical angular momentum conversion in a nanoslit. *Opt. Lett.*, 37(23):4946–4948, 2012.

[175] M. Mansuripur, A. R. Zakharian, and E. M. Wright. Spin and orbital angular momenta of light reflected from a cone. *Phys. Rev. A*, 84(3), 2011.

[176] N. Radwell, R. D. Hawley, J. B. Götte, and S. Franke-Arnold. Achromatic vector vortex beams from a glass cone. *Nat. Comm.*, 7(1), 2016.

[177] F. Bouchard, H. Mand, M. Mirhosseini, E. Karimi, and R. W Boyd. Achromatic orbital angular momentum generator. *New J. Phys.*, 16(12):123006, 2014.

[178] S.J. van Enk. Geometric phase, transformations of gaussian light beams and angular momentum transfer. *Opt. Commun.*, 102(1):59 – 64, 1993.

[179] E. J. Galvez, P. R. Crawford, H. I. Sztul, M. J. Pysher, P. J. Haglin, and R. E. Williams. Geometric phase associated with mode transformations of optical beams bearing orbital angular momentum. *Phys. Rev. Lett.*, 90:203901, 2003.

[180] G. Milione, H. I. Sztul, D. A. Nolan, and R. R. Alfano. Higher-order Poincaré sphere, Stokes parameters, and the angular momentum of light. *Phys. Rev. Lett.*, 107(5), 2011.

[181] L. Allen, J. Courtial, and M. J. Padgett. Matrix formulation for the propagation of light beams with orbital and spin angular momenta. *Phys. Rev. E*, 60:7497–7503, 1999.

[182] K. Y. Bliokh, M. A. Alonso, and M. R. Dennis. Geometric phases in 2D and 3D polarized fields: geometrical, dynamical, and topological aspects. *arXiv:1903.01304*, 2019.

[183] C. Bouchiat and G.W. Gibbons. Non-integrable quantum phase in the evolution of a spin-1 system : a physical consequence of the non-trivial topology of the quantum state-space. *J. Phys.*, 49(2):187–199, 1988.

[184] G. Khanna, S. Mukhopadhyay, R. Simon, and N. Mukunda. Geometric phases for SU(3) representations and three level quantum systems. *Annals of Physics*, 253:55–82, 1997.

[185] R. Bhandari. Geometric phase in an arbitrary evolution of a light beam. *Phys. Lett. A*, 135(4-5):240–244, 1989.

[186] J. H. Hannay. The Majorana representation of polarization, and the Berry phase of light. *J. Mod. Opt.*, 45:1001 –1008, 1998.

[187] J. H. Hannay. The Berry phase for spin in the Majorana representation. *J. Phys. A.*, 31(2):L53–L59, 1998.

[188] K. Y. Bliokh, Y. Gorodetski, V. Kleiner, and E. Hasman. Coriolis effect in optics: Unified geometric phase and spin-Hall effect. *Phys. Rev. Lett.*, 101:030404, 2008.

[189] A. Karnieli and A. Arie. Fully controllable adiabatic geometric phase in nonlinear optics. *Opt. Express*, 26(4):4920, 2018.

[190] L. B. Ma, S. L. Li, V. M. Fomin, M. Hentschel, J. B. Götte, Y. Yin, M. R. Jorgensen, and O. G. Schmidt. Spin–orbit coupling of light in asymmetric microcavities. *Nat. Comm.*, 7(1), 2016.

[191] J. Kreismann and M. Hentschel. The optical Möbius strip cavity: Tailoring geometric phases and far fields. *EPL*, 121(2):24001, 2018.

[192] K. Y. Bliokh, E. A. Ostrovskaya, M. A. Alonso, O. G. Rodríguez-Herrera, D. Lara, and C. Dainty. Spin-to-orbital angular momentum conversion in focusing, scattering, and imaging systems. *Opt. Express*, 19(27):26132–26149, 2011.

[193] A. V. Arzola, L. Chvátal, P. Jákl, and P. Zemánek. Spin to orbital light momentum conversion visualized by particle trajectory. *Sc. Rep.*, 9(1), 2019.

[194] E. H. Hall. On a new action of the magnet on electric currents. *A. J. Math.*, 2(3):287–292, 1879.

[195] E.H. Hall. On the "rotational coefficient" in nickel and cobalt. *The London, Edinburgh, and Dublin Philosophical Magazine and Journal of Science*, 12(74):157–172, 1881.

[196] N. Nagaosa, J. Sinova, S. Onoda, A. H. MacDonald, and N. P. Ong. Anomalous Hall effect. *Rev. Mod. Phys.*, 82:1539–1592, 2010.

[197] X. Ling, X. Zhou, K. Huang, Y. Liu, C. W. Qiu, H. Luo, and S. Wen. Recent advances in the spin Hall effect of light. *Reports on Progress in Physics*, 80(6):066401, 2017.

[198] V. S. Liberman and B. Ya. Zel'dovich. Spin-orbit interaction of a photon in an inhomogeneous medium. *Phys. Rev. A*, 46:5199–5207, 1992.

[199] K. Y. Bliokh and Y. P. Bliokh. Conservation of angular momentum, transverse shift, and spin Hall effect in reflection and refraction of an electromagnetic wave packet. *Phys. Rev. Lett.*, 96:073903, 2006.

[200] Masaru Onoda, Shuichi Murakami, and Naoto Nagaosa. Hall effect of light. *Phys. Rev. Lett.*, 93:083901, 2004.

[201] A. V. Dooghin, N. D. Kundikova, V. S. Liberman, and B. Ya. Zel'dovich. Optical Magnus effect. *Phys. Rev. A*, 45:8204–8208, 1992.

[202] K. Y. Bliokh, I. V. Shadrivov, and Y. S. Kivshar. Goos–Hänchen and Imbert–Fedorov shifts of polarized vortex beams. *Opt. Lett.*, 34(3):389–391, 2009.

[203] F. Goos and H. Hänchen. Ein neuer und fundamentaler versuch zur totalreflexion. *Annalen der Physik*, 436(7-8):333–346, 1947.

[204] F.I. Ferodov. On the theory of total reflection. *Dokl Akad Nauk SSSR*, (105):465–468, 1955.

[205] C. Imbert. Calculation and experimental proof of the transverse shift induced by total internal reflection of a circularly polarized light beam. *Phys. Rev. D*, 5:787–796, 1972.

[206] K Y Bliokh and A Aiello. Goos–Hänchen and Imbert–Fedorov beam shifts: an overview. *J. Opt.*, 15(1):014001, 2013.

[207] H. Luo, X. Ling, X. Zhou, W. Shu, S. Wen, and D. Fan. Enhancing or suppressing the spin Hall effect of light in layered nanostructures. *Phys. Rev. A*, 84:033801, 2011.

[208] K. Yu. Bliokh and Yu. P. Bliokh. Polarization, transverse shifts, and angular momentum conservation laws in partial reflection and refraction of an electromagnetic wave packet. *Phys. Rev. E*, 75:066609, 2007.

[209] M. Merano, N. Hermosa, J. P. Woerdman, and A. Aiello. How orbital angular momentum affects beam shifts in optical reflection. *Phys. Rev. A*, 82:023817, 2010.

[210] R. Dasgupta and P.K. Gupta. Experimental observation of spin-independent transverse shift of the centre of gravity of a reflected Laguerre–Gaussian light beam. *Opt. Commun.*, 257(1):91–96, 2006.

[211] J. Zhang, X.X. Zhou, X.H. Ling, S. Z. Chen, H. L. Luo, and S. C. Wen. Orbit-orbit interaction and photonic orbital Hall effect in reflection of a light beam. *Chinese Physics B*, 23(6):064215, 2014.

[212] K. Y. Bliokh and A. S. Desyatnikov. Spin and orbital Hall effects for diffracting optical beams in gradient-index media. *Phys. Rev. A*, 79:011807, 2009.

[213] H. Okuda and H. Sasada. Huge transverse deformation in nonspecular reflection of a light beam possessing orbital angular momentum near critical incidence. *Opt. Express*, 14(18):8393–8402, 2006.

[214] H. Okuda and H. Sasada. Significant deformations and propagation variations of Laguerre-Gaussian beams reflected and transmitted at a dielectric interface. *J. Opt. Soc. Am. A*, 25(4):881–890, 2008.

[215] O. Hosten and P. Kwiat. Observation of the spin Hall effect of light via weak measurements. *Science*, 319(5864):787–790, 2008.

[216] F. Nori. The dynamics of spinning light. *Nat. Photonics*, 2:717, 2008.

[217] X. Ling, X. Zhou, X. Yi, W. Shu, Y. Liu, S. Chen, H. Luo, S. Wen, and D. Fan. Giant photonic spin Hall effect in momentum space in a structured metamaterial with spatially varying birefringence. *Light: Science &Amp; Applications*, 4:e290, 2015.

[218] K. Y. Bliokh and F. Nori. Relativistic Hall effect. *Phys. Rev. Lett.*, 108:120403, 2012.

[219] K. Y. Bliokh, Y. V. Izdebskaya, and F. Nori. *Transverse Relativistic Effects in Paraxial*

Wave Interference, pages 237–246.

[220] X. Ling, X. Zhou, and X. Yi. Geometric spin Hall effect of light with inhomogeneous polarization. *Opt. Commun.*, 383:412–417, 2017.

[221] Y. Gorodetski, K. Y. Bliokh, B. Stein, C. Genet, N. Shitrit, V. Kleiner, E. Hasman, and T. W. Ebbesen. Weak measurements of light chirality with a plasmonic slit. *Phys. Rev. Lett.*, 109:013901, 2012.

[222] N. Shitrit, I. Bretner, Y. Gorodetski, V. Kleiner, and E. Hasman. Optical spin hall effects in plasmonic chains. *Nano Letters*, 11(5):2038–2042, 2011.

[223] H. Luo, S. Wen, W. Shu, Z. Tang, Y. Zou, and D. Fan. Spin Hall effect of a light beam in left-handed materials. *Phys. Rev. A*, 80(4), 2009.

[224] D. O'Connor, P. Ginzburg, F. J. Rodríguez-Fortuño, G. A. Wurtz, and A. V. Zayats. Spin–orbit coupling in surface plasmon scattering by nanostructures. *Nat. Comm.*, 5(1), 2014.

[225] X. Ling, X. Yi, X. Zhou, Y. Liu, W. Shu, H. Luo, and S. Wen. Realization of tunable spin-dependent splitting in intrinsic photonic spin Hall effect. *Appl. Phys. Lett.*, 105(15):151101, 2014.

[226] Y. Zhang, P. Li, S. Liu, and J. Zhao. Unveiling the photonic spin Hall effect of freely propagating fan-shaped cylindrical vector vortex beams. *Opt. Lett.*, 40(19):4444–4447, 2015.

[227] A. Bekshaev, A. Chernykh, A. Khoroshun, and L. Mikhaylovskaya. Singular skeleton evolution and topological reactions in edge-diffracted circular optical-vortex beams. *Opt. Communun.*, 397:72–83, 2017.

[228] A. Y. Bekshaev. Spin–orbit interaction of light and diffraction of polarized beams. *J. Opt.*, 19(8):085602, 2017.

[229] Z. Zhang, Z. You, and D. Chu. Fundamentals of phase-only liquid crystal on silicon (LCOS) devices. *Light Sci. Appl.*, 3(10):213–213, 2014.

[230] J. Harriman, S. Serati, and J. Stockley. Comparison of transmissive and reflective spatial light modulators for optical manipulation applications. In K. Dholakia and G. C. Spalding, editors, *Optical Trapping and Optical Micromanipulation II*. SPIE, 2005.

[231] H. Takagi, J. Kim, K. H. Chung, S. Mito, H. Umezawa, and M. Inoue. Magneto-optic spatial light modulators with magnetophotonic crystals driven by PZT films. *J. Magn. Soc. Jpn.*, 33(6_2):525–527, 2009.

[232] T. Bifano. MEMS deformable mirrors. *Nat. Photonics*, 5:21 EP –, 2011.

[233] J. S. Ahearn, M. H. Weiler, S. B. Adams, T. P. McElwain, A. Stark, L. DePaulis, A. L. Sarafinas, T. Hongsmatip, R. J. Martin, and B. Lane. Multiple quantum well (MQW) spatial light modulators (SLMs) for optical data processing and beam steering. In U. Efron, editor, *Spatial Light Modulators: Technology and Applications*. SPIE, 2001.

[234] M. A. Cibula and D. H. McIntyre. General algorithm to optimize the diffraction efficiency of a phase-type spatial light modulator. *Optics Letters*, 38(15):2767, 2013.

[235] I. Moreno, C. Iemmi, A. Márquez, J. Campos, and M. J. Yzuel. Modulation light efficiency of diffractive lenses displayed in a restricted phase-mostly modulation display. *Applied Optics*, 43(34):6278, 2004.

[236] R. Bowman, V. D'Ambrosio, E. Rubino, O. Jedrkiewicz, P. Di Trapani, and M. J. Padgett. Optimisation of a low cost SLM for diffraction efficiency and ghost order suppression. *The European Physical Journal Special Topics*, 199(1):149–158, 2011.

[237] M. Ohtsu and T. Yatsui, editors. *Progress in Nanophotonics 3*. Springer International Publishing, 2015.

[238] A.Ya. Bekshaev and S.V. Sviridova. Effects of misalignments in the optical vortex transformation performed by holograms with embedded phase singularity. *Opt. Commun.*, 283(24):4866–4876, 2010.

[239] B. Sephton, A. Dudley, and A. Forbes. Radial modes in phase-only twisted light beams. In *Optical Trapping and Optical Micromanipulation XIV*. SPIE, 2017.

[240] J. M. Hickmann, E. J. S. Fonseca, W. C. Soares, and S. Chávez-Cerda. Unveiling a truncated optical lattice associated with a triangular aperture using light's orbital angular momentum. *Phys. Rev. Lett.*, 105:053904, 2010.

[241] J. G. Silva, A. J. Jesus-Silva, M. A. R. C. Alencar, J. M. Hickmann, and Ed. J. S. Fonseca. Unveiling square and triangular optical lattices: a comparative study. *Opt. Lett.*, 39(4):949–952, 2014.

[242] S. N. Alperin, R. D. Niederriter, J. T. Gopinath, and M. E. Siemens. Quantitative measurement of the orbital angular momentum of light with a single, stationary lens. *Opt. Lett.*, 41(21):5019–5022, 2016.

[243] A. Fresnel, H. H. Senarmont, E. Verdet, and L. F. Fresnel. *OEuvres completes d'Augustin Fresnel*. Imprimerie imperiale Paris, 1866.

[244] T. Young. On the theory of light and colours. *Philosophical Transactions of the Royal Society of London*, 92:12–48, 1802.

[245] F. A. Jenkins and H. E. White. *Fundamentals of optics*. McGraw-Hill New York, 2nd ed. edition, 1950.

[246] A. Sabatyan and S. A. Hoseini. Fresnel biprism as a 1D refractive axicon. *Optik*, 124(21):5046 – 5048, 2013.

[247] J. Arlt and K. Dholakia. Generation of high-order Bessel beams by use of an axicon. *Opt. Communun.*, 177(1):297 – 301, 2000.

[248] J. W. Goodman. *Introduction to Fourier optics*. 1995.

[249] F. Kottler. Elektromagnetische theorie der beugung an schwarzen schirmen. *Annalen der Physik*, 376(15):457–508, 1923.

[250] F. Shen and A. Wang. Fast-Fourier-transform based numerical integration method for the Rayleigh-Sommerfeld diffraction formula. *Appl. Opt.*, 45(6):1102–1110, 2006.

[251] T. C. Poon and J. P. Liu. *Introduction to Modern Digital Holography*. Cambridge University Press, 2013.

[252] A. Y. Bekshaev, K. A. Mohammed, and I. A. Kurka. Transverse energy circulation and the edge diffraction of an optical vortex beam. *Appl. Opt.*, 53(10):B27–B37, 2014.

[253] J. Hamazaki, Y. Mineta, K. Oka, and R. Morita. Direct observation of Gouy phase shift in a propagating optical vortex. *Opt. Express*, 14(18):8382–8392, 2006.

[254] S. M. Baumann, D. M. Kalb, L. H. MacMillan, and E. J. Galvez. Propagation dynamics of optical vortices due to gouy phase. *Opt. Express*, 17(12):9818–9827, Jun 2009.

[255] R. Simon and N. Mukunda. Bargmann invariant and the geometry of the Gouy effect. *Phys. Rev. Lett.*, 70:880–883, 1993.

[256] S. Feng and H. G. Winful. Physical origin of the Gouy phase shift. *Optics Letters*, 26(8):485, 2001.

[257] I. Zeylikovich and A. Nikitin. Diffraction of a gaussian laser beam by a straight edge leading to the formation of optical vortices and elliptical diffraction fringes. *Opt. Commun.*, 413:261–268, 2018.

[258] J. Korger, A. Aiello, V. Chille, P. Banzer, C. Wittmann, N. Lindlein, C. Marquardt, and G. Leuchs. Observation of the geometric spin Hall effect of light. *Phys. Rev. Lett.*, 112:113902, 2014.

[259] M. Neugebauer, S. Nechayev, M. Vorndran, G. Leuchs, and P. Banzer. Weak measurement enhanced spin Hall effect of light for particle displacement sensing. *Nano Letters*, 19(1):422–425, 2018.

[260] G. Gibson, J. Courtial, M. J. Padgett, M. Vasnetsov, V. Pas'ko, S. M. Barnett, and S. Franke-Arnold. Free-space information transfer using light beams carrying orbital angular momentum. *Opt. Express*, 12(22):5448–5456, 2004.

[261] Gabriel Molina-Terriza, Jaume Recolons, and Lluis Torner. The curious arithmetic of optical vortices. *Opt. Lett.*, 25(16):1135–1137, 2000.

[262] G. Molina-Terriza, J. Recolons, J. P. Torres, L. Torner, and E. M. Wright. Observation of the dynamical inversion of the topological charge of an optical vortex. *Phys. Rev. Lett.*, 87:023902, 2001.

[263] M. Hisatomi, M.C. Parker, and S.D. Walker. Waveguiding of orbital angular momentum light using chiral-selectivity azimuthally graded index fibre. In *OFC/NFOEC Technical Digest. Optical Fiber Communication Conference, 2005.* IEEE, 2005.

[264] Y. Yang, A. Liu, L. Chin, X. Zhang, D. Tsai, C.L. Lin, C. Lu, G.P. Wang, and N.I. Zheludev. Optofluidic waveguide as a transformation optics device for lightwave bending and manipulation. *Nat. Commu.*, 3:651, 2012.

[265] E. Fabri, G. Fiorio, F. Lazzeri, and P. Violino. Mirage in the laboratory. *A. J. Phys.*, 50(6):517–520, 1982.

[266] K. Tennakone. A mirage from a laser. *Am. J. Phys.*, 51(3):270–271, 1983.

[267] W. M. Strouse. Bouncing light beam. *Am. J. Phys.*, 40(6):913–914, 1972.

[268] R. G. Greenler. Laboratory simulation of inferior and superior mirages. *J. Opt. Soc. Am. A*, 4(3):589–590, 1987.

[269] J. H. Gladstone and T. P. Dale. Researches on the refraction, dispersion, and sensitiveness of liquids. *Philosophical Transactions of the Royal Society of London*, 153:317–343, 1863.

[270] M. Daimon and A. Masumura. Measurement of the refractive index of distilled water from the near-infrared region to the ultraviolet region. *Appl. Opt.*, 46(18):3811–3820, 2007.

[271] I. Z. Kozma, P. Krok, and E. Riedle. Direct measurement of the group-velocity mismatch and derivation of the refractive-index dispersion for a variety of solvents in the ultraviolet. *J. Opt. Soc. Am. B*, 22(7):1479–1485, 2005.

[272] T. Zhang, G. Feng, Z. Song, and S. Zhou. A single-element interferometer for measuring refractive index of transparent liquids. *Opt. Commun.*, 332:14 – 17, 2014.

[273] A. Fick. Ueber diffusion. *Annalen der Physik*, 170(1):59–86, 1855.

[274] K. C. Mamola, Wilhelm F. Mueller, and Bruce J. Regittko. Light rays in gradient index media: A laboratory exercise. *A. J. Phys.*, 60(6):527–529, 1992.

[275] T. C Poon and T. Kim. *Engineering Optics With Matlab*. World Scientific Publishing Co., Inc., River Edge, NJ, USA, 2006.

[276] N. González, G. Molina-Terriza, and J. P. Torres. How a Dove prism transforms the orbital angular momentum of a light beam. *Opt. Express*, 14(20):9093–9102, 2006.

[277] A. Roszkiewicz and W. Nasalski. Extraordinary optical transmission and vortex excitation by periodic arrays of Fresnel zone plates. *Bulletin of the Polish Academy of Sciences: Technical Sciences*, 61(4):855–861, 2013.

[278] B. M. Azizur Rahman and Arti Agrawal. *Finite element modeling methods for photonics*. Artech House, Boston, Massachusetts, 2013. b2302287.

APPENDIX 1

Interference between vector vortex beams

Claire Marie Cisowski[1], Amanda Kronhardt Fritsch[1], Ricardo Rego Bordalo Correia[1]
[1]Universidade Federal do Rio Grande do Sul, Av. Bento Gonçalves 9500 Agronomia, 91501-970 Porto Alegre, RS, Brasil.
Author e-mail address: claire.cisowski@ufrgs.br

Abstract: We numerically demonstrate that interfering two paraxial monochromatic beams corresponding to orthogonal states on the higher-order Poincaré sphere leads to the disappearance of the interference pattern. This extends the concept of quantum eraser to vector vortex beams.

1. Introduction

In 1816, Fresnel and Arago established that two orthogonally polarized do not interfere [1]. Homogeneous polarization states of light are often represented as points spanning the surface of the Poincaré Sphere (PS), diametrically opposite points representing orthogonal states. Interfering a state B with a state A corresponds to transporting B to A along the shorter geodesic on the PS, performing a "projection". Orthogonal states do not interfere as their phase difference is undefined [2]. Recently, beams with inhomogeneous polarization and phase distributions such as vector vortex beams have received considerable attention [3]. To account for both spin and higher dimensional orbital states, Milione et. al. introduced higher-order Poincaré spheres (HOPS) [4]. Such representation features orthogonal circularly polarized optical vortex beams at the poles and cylindrical vector (CV) beams at the equator. Relying on Jones formalism, we study the interference between pairs of VV beams spanning the surface of an HOPS (see Fig.1.a). VV beams are defined as follows [5]:

$$E(r,\Phi,\Theta) = \cos\left(\tfrac{\Phi}{2}\right) \mathrm{LG}_0^{\ell}\, e^{-i\Theta/2}\ \hat{\mathbf{R}} + \sin\left(\tfrac{\Phi}{2}\right) \mathrm{LG}_0^{\ell}\, e^{i\Theta/2}\ \hat{\mathbf{L}} \qquad (1)$$

With $\hat{\mathbf{R}}$ and $\hat{\mathbf{L}}$ being the unitary vectors of the right and left CP basis and with $\Phi \in [0,\pi]$ and $\Theta \in [0,2\pi]$.

3. Numerical results and discussion

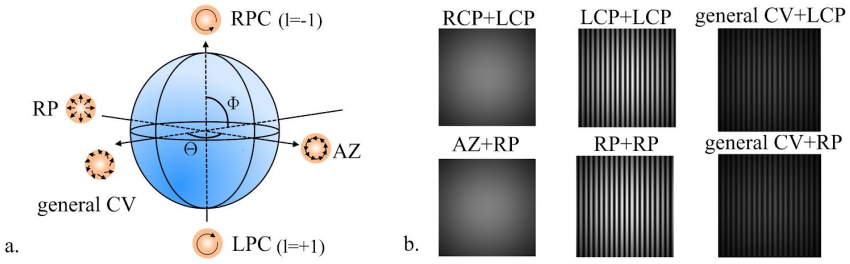

Fig.1. a. Higher order Poincaré sphere for $\ell = \pm 1$ OV beams at the poles, the arrows indicate the polarization distribution. b. Interference patterns of various combination of VV beams spanning the higher order Poincaré sphere.

We evidence that the interference of two orthogonal states on the higher order Poincaré sphere leads to the disappearance of the interference fringes (see Fig.1.b). Our results are in agreement with the experimental work of I. Nape et al. [6]. Such interference studies opens perspectives to exploring higher-order Pancharatnam Berry phases.

[1] D. F. J. Arago and A. J. Fresnel "On the action of rays of polarized light upon each other", *Ann. Chim. Phys.,* **2**, 288-304 (1819).
[2] R. Bhandari. "Polarization of light and topological phases", *Phys. reports.,* **281**, 1-64 (1997).
[3] A. Zhan. "Cylindrical vector beams: from mathematical concepts to applications", *Adv. Opt. Photon.,* **1**, 1-57 (2009).
[4] G. Milione, H.I. Sztul, D.A. Nolan, R.R. Alfano. "Higher-order Poincaré Sphere, Stokes Parameters and the Angular momentum of light", *Phys. Rev. Letters.,* **107**, 053601 (2011).
[5] N. Bhebhe, P.A.C. Williams, C. R-Guzman, V. R.-Fajardo, A. Forbes. "A vector holographic optical trap", *Nat. Sc. Reports,* **8**, 17387 (2018).
[6] I. Nape, B. Ndagano, A. Forbes. "Erasing the orbital angular momentum information of a photon", *Phys. Rev. A.* **95,** 053859 (2017).

APPENDIX 2

Based on the work of P. F. Chimento et al [174] and of A. Roszkiewicz and W. Nasalski [277] on SAM to OAM conversion upon transmission from a circular air nanoslit on a thin metal film, we investigated as a proof of principle numerical study, the phase and polarization distribution exiting from a air nanoslit of radius 100 nm and width 20 nm in a gold layer of 200 nm thickness on a glass substrate, when illuminated by a monochromatic (λ=530 nm), circularly polarized plane wave.

This study was carried out using a Finite-difference time-domain method, which computes the full electric and magnetic field within the computation domain [278].

As illustrated on figure (40), we find that at a propagation distance $2\mu\mathrm{m}$ after the slit, the phase distribution of the electric field spin-flipped component exhibits a helical phase distribution of topological charge ℓ=$+2$ and that the spatial distribution of the transverse total electric field direction in the transverse plane is inhomogeneous.

SAM to OAM conversion is only partial in this case as the ring retardation was not optimised nor characterized in this preliminary study.

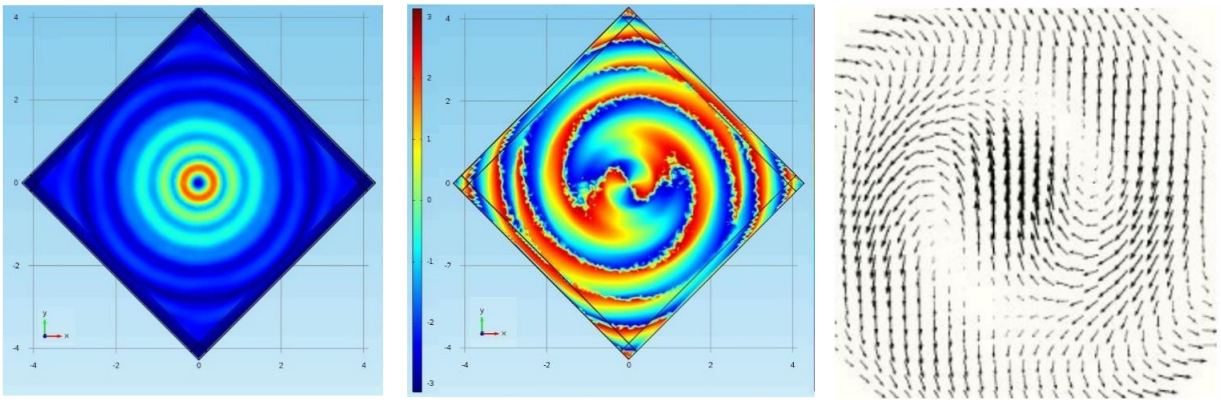

a. b. c.

Figure 40 – a. Intensity and b. phase of the spin-flip component. c. transverse electric vector distribution at a propagation distance of $2\mu\mathrm{m}$ after a nano aperture.

APPENDIX 3

Letter Vol. 43, No. 3 / February 1 2018 / Optics Letters 499

Optics Letters

Splitting an optical vortex beam to study photonic orbit–orbit interactions

Claire M. Cisowski* and Ricardo R. B. Correia

Instituto de Física, Universidade Federal do Rio Grande do Sul, Av. Bento Gonçalves 9500 Porto Alegre, RS, Brazil
**Corresponding author: claire.cisowski@ufrgs.br*

Received 27 November 2017; revised 25 December 2017; accepted 29 December 2017; posted 2 January 2018 (Doc. ID 314313); published 25 January 2018

We numerically and experimentally evidence photonic orbit–orbit interactions in freely propagating asymmetrical beams carrying orbital angular momentum. A Fresnel biprism is used to carry out the wavefront division of an optical vortex beam, generating two complementary asymmetrical beams. The optical orbital Hall effect is presented in the form of angular deviations from the beam's geometrical expectation. We also observe the rotation of the field transverse profile near the nominal propagation axis upon propagation, which direction depends on orbital momentum currents.

OCIS codes: (260.6042) Singular optics; (050.4865) Optical vortices; (070.2580) Paraxial wave optics.

https://doi.org/10.1364/OL.43.000499

In the semi-classical approximation [1], the spin and orbital properties of light become coupled. In paraxial beams, photonic spin–orbit interactions refer to the coupling between spin angular momentum, associated with circular polarization, and extrinsic orbital angular momentum (EOAM), related to the trajectory of the beam's centroid [2]. Similarly, coupling between intrinsic orbital angular momentum, associated with optical vortices, and EOAM is known as orbit–orbit interaction. Both interactions are related to geometrical Berry phases and topological spin or orbital transport, namely the spin Hall effect (SHE) for spin–orbit interactions or orbital Hall effect (OHE) for orbit–orbit interactions [3].

SHEs consist of polarization-dependent deflections of the beam's trajectory. SHEs can manifest at sharp interfaces in the form of polarized-dependent transverse shifts known as Fedorov–Imbert shifts [4,5] and in smoothly inhomogeneous media, as spin-dependent angular deflections (also known as optical Magnus effect [6]), leading to splitting of beams with different polarization states [7].

OHEs refer to orbital-dependent deflections of the beam's trajectory. OHEs have been extensively studied at sharp interfaces in the form of orbital-dependent transverse shifts [8,9] and orbital angular deflections in smoothly inhomogeneous media [3]. The latter evidence splitting of beams with different topological charges ℓ (pitch, in units of wavelength, of the helical wavefront on the single full rotation near the axis) as well as splitting of multi-charged vortex beams into constellations of ℓ unit strength vortices [10,11]. Deformation of the beams intensity distributions, involved in the process of orbital momentum conservation, and the appearance of rotation of the beam profile upon propagation, dependent on orbital momentum current, have also been reported in this context [12,13].

Remarkably, Hall effects can also manifest in freely propagating asymmetrical beams [14] and, in the case of SHE effects, can even be enhanced without relying on complex fabrication techniques [15]. By breaking the symmetry of a paraxial linearly polarized optical vortex beam, OHE emerges as unbalanced transverse fluxes generate an extra transverse OAM, responsible for OAM-dependent angular deflections [16,17] and multi-charged vortices breakdown [18]. The process of multi-charged optical vortices breakdown upon symmetry breaking is of particular interest as it exposes processes involved in orbital momentum conversion and implies complex optical vortices dynamics [17].

Symmetry breaking also reveals the rotation of the field transverse profile near the nominal propagation axis upon propagation [3,19]. The role of transverse-orbital and spin momentum currents upon the rotation of a free propagating beam's centroid has been discussed by Luo *et al.* in the case of a general vector field, who also related the rotation angle to the Gouy phase [20]. For helical beams, the rotation direction indeed shows a dependence on transverse OAM currents, related to the sign of the optical vortex topological charge ℓ [21–23].

To study these effects, we consider a paraxial Laguerre–Gauss (LG) beam carrying an optical vortex of topological charge ℓ propagating in the z direction, incident upon a Fresnel biprism to perform symmetry breaking. A Fresnel biprism is an optical plate with equal wedges from opposite extremities forming a centered wide apex angle. Each wedge refracts light in a direction determined by the apex's complementary angle β, causing an incident beam simultaneously illuminating both wedges to be split into two complementary beams propagating in different directions [24]. In the biprism's exit plane $z = z_1 = 0$, the field complex amplitude $u_1(\ell, a)$ can be written as

$$u_1(\ell, a) = \mathrm{LG}_{0\ell}(\ell)\mathrm{FB}(a), \tag{1}$$

0146-9592/18/030499-04 Journal © 2018 Optical Society of America

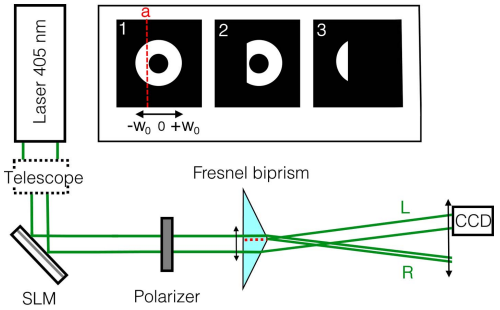

Fig. 1. (a) Linearly polarized LG beam carrying an optical vortex of topological ℓ illuminates a Fresnel biprism and is split into two complementary beams propagating in the right (R) and left (L) directions. Inset: lateral displacement of the Fresnel biprism's center a ranging from $-w_o$ to $+w_o$.

with LG(ℓ) a standard LG beam of topological charge ℓ as defined by Allen *et al.* [25] and BF(a) accounting for the action of the Fresnel biprism,

$$\mathrm{FB}(a) = \exp(-ik(\beta/2)\mathrm{sgn}(x-a))(x-a), \tag{2}$$

with a being the position of the biprism's apex. At the biprism's exit plane, the field's relative position with respect to the biprism's apex a defines two possible propagation directions forming an angle $\beta/2$ with the z-axis. Consequently, the initial beam is split into two complementary beams propagating to the right (R) or to the left (L) direction (see Fig. 1) and Eq. (1) can be rewritten as $u_1(\ell) = u_{1,R}(\ell) + u_{1,L}(\ell)$.

At a propagation distance r_{12}, each split beam's complex amplitude $u_{2,R(L)}(\ell)$ in the plane $z = z_2$ can be obtained using the Rayleigh–Sommerfeld diffraction formula [26]:

$$u_{2,R(L)}(\ell, a) = \iint u_{1,R(L)}(\ell, a)(z_{12}/(i\lambda r_{12}^2)) \times \exp(+ikr_{12})\mathrm{d}x_1\mathrm{d}y_1. \tag{3}$$

The gravity center g of each split beam in the $z = z_2$ plane can be defined as [27]

$$\mathbf{g_{R(L)}}(\ell, a) = \frac{1}{P}\int \mathbf{r}|u_{2,R(L)}(\ell, a)|^2\mathrm{d}x\mathrm{d}y, \tag{4}$$

with P being the beam's power $P = \int |u_{2,R(L)}(\ell, a)|^2\mathrm{d}x\mathrm{d}y$ and $\mathbf{r}$ being the transverse radius vector.

In the absence of OHE, $\mathbf{g_{R(L)}}(\ell, a)$ coincides with the geometrical expectation of the split beam's trajectory due to the biprism's edge diffraction; this is the case for split beams without orbital angular momentum ($\ell = 0$). Angular deviations θ_y along y of each split beam's trajectory from its geometrical expectations can be calculated as

$$\theta_y = \mathrm{atan}[(\mathbf{g_{R(L)}}(\ell, a) - \mathbf{g_{R(L)}}(\ell = 0, a))_y/z_{12}]. \tag{5}$$

Our experimental setup is shown in Fig. 1. We use a fiber-coupled Fabry–Perot laser operating at 405 nm. The beam's output is collimated and illuminates a forked diffraction grating produced by a spatial light modulator (SLM). The SLM produces LG beams of topological charges ranging from $\ell = 0$ to $\ell = \pm 5$ in its first diffraction order [28]. A polarizer introduced after the SLM determines a linear polarization state for the beam.

The beam illuminates a Fresnel biprism of diffraction angle $\beta = 6.46$ mrad mounted on a millimetric stage. Lateral scan of the Fresnel biprism allows to control in which proportion each biprism's wedge is illuminated. The biprism's center position a ranges from $-w_0$ to w_0, covering the whole incident beam, with $a = 0$ generating two perfect half beams. The beam's waist radius at the exit of the biprism z_1 is $w_0 = 431$ μm. The intensity pattern of the two complementary split beams are recorded on a CCD camera of resolution 1296×964 and pixel size 3.75 μm. The CCD camera is placed at 60.0 cm after the biprism on a millimetric stage such that it can image both diffracted beams. Our SLM produces a LG beam with various radial modes; only the lowest-order intensity ring is extracted from the images for post-processing. The beam's center of gravity from the CCD images are calculated using Eq. (4) and the deviation angle is obtained using Eq. (5).

We perform a series of measures based on the following procedure: for a given position of a (Fig. 1, inset image 1), the CCD camera is centered on one split beam (Fig. 1, inset image 2). The incident beam's topological charge is varied from $\ell = -5$ to $\ell = +5$ including $\ell = 0$ and the intensity profiles are recorded on the CCD camera. For the same position a, the camera is translated and centered on the other split beam (Fig. 1, inset image 3) and the procedure is repeated. The image acquisition is repeated for various positions of a and the centers of gravity for each beam part $\mathbf{g_{R(L)}}(\ell, a)$ are calculated.

A numerical model using the Rayleigh–Sommerfeld diffraction formula described above is used to calculate the corresponding angular diffraction. We consider a LG beam of azimuthal order ℓ and radial order 0. Intensity patterns at 60.0 cm after the biprism are generated for various values of a, using the parameters of our biprism. The positions of the gravity centers are extracted from the numerical model, as well as the corresponding angular deviations.

Both split beams' experimental and numerical intensity patterns exhibit a rotation as a whole, related to the sign of the topological charge ℓ: for $\ell > 0$ the intensity pattern follows an anti-clockwise rotation whereas for $\ell < 0$ the intensity pattern follows a clockwise rotation, following the circulation of internal OAM fluxes. The emergence of beam rotation as a whole has been described by Basistiy *et al.* [29] by considering the phase of a paraxial LG beam, neglecting propagating factors, as originating from the Gouy phase of the beam, for a beam with radial mode 0, $-(|\ell| + 1)\arctan(z/z_R)$ (z_R being the Rayleigh length) combined with the characteristic azimuthal dependence $\ell\varphi$. They showed the expression for the phase can be rewritten to evidence a new azimuth angle $\varphi' = \varphi - \mathrm{sgn}(\ell)\arctan(z/z_R)$, demonstrating rotation of coordinate frame or rotation of a beam as a whole during propagation, dependent on the sign of ℓ and independent of its magnitude. In the far-field limit, the beam's apparent rotation stabilizes after having performed a $\pi/2$ rotation [29]. Other works also relate the rotation to the Gouy phase [30–33]. Note that the Gouy phase shift is a manifestation of a general Berry phase [34] and originates from a transverse spatial confinement, introducing a spread in the transverse momenta [35]. The rotation is particularly noticeable for high values of ℓ (see Fig. 2) [36]. Evidence of internal fluxes in symmetry breaking has been reported in the case of edge-diffracted beams [17], and

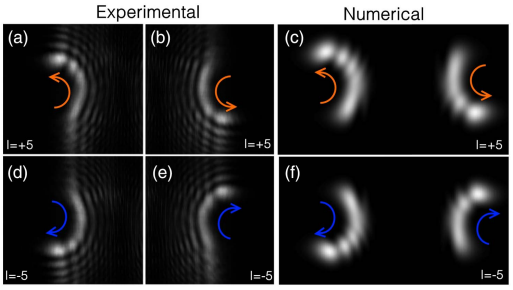

Fig. 2. (a, b, d, e) Experimental and (c, f) simulated intensity patterns of complementary split beams for $a = 0$ at $z = 60$ cm for $\ell = +5$ (upper panel) and $\ell = -5$ (lower panel). For $\ell > 0$ the intensity patterns exhibit an anti-clockwise rotation whereas for $\ell < 0$ they exhibit clockwise rotation.

here we extend this observation to the two complementary split beams.

The analysis of the beam's center of gravity for both experimental and numerical data evidence angular deviations from the geometrical expectation, scaling with the amount of OAM carried by the beam, evidencing another phenomenon related to orbit–orbit interaction, i.e., the orbital Hall effect. Angular deviations occur parallel to the biprism's apex line. The error upon the beam's experimental displacement was evaluated by taking the full beam, entirely refracted in one single direction after the Fresnel biprism, and taking the displacement of the gravity centers for $\ell = -5$ to $\ell = +5$; $\ell = 0$ included, a maximum error of 0.03 mrad was found.

For an initial beam carrying orbital angular momentum, changing the split beams' asymmetry by selecting various values of a alters the angular deviations in agreement with the orbital Hall effect. Note that for a fixed value of a, the angular deviations scale with $|\ell| + 1$ ($\forall\ |\ell| \geq 1$) (see Fig. 3). This is due to the difference between the fluxes' velocity according to different values of ℓ. Both experimental and numerical results evidence that the angular deviation between the right and left split beams are correlated (see blue line in Fig. 3). This feature theoretically gives our setup an additional sensitivity when it comes to measuring angular deviations due to Hall effects, in contrast to partially blocked beams.

In this regard the usage of a Fresnel biprism to provide symmetry breaking adds a full new perspective to explore the complementarity properties of the split beams. Using the biprism to split optical vortex beams also allows us to study quantum correlations between the two beams' split parts. Another subject of interest is the dynamics of the single-charge vortices created from a multi-charged optical vortex beam in both complementary beams. A good sensitivity in measures of deviations can also be used to study spin Hall effects, which are expected to be of lower magnitude than orbital Hall effects [3].

The transverse angular shift of a truncated beam corresponds to the transverse canonical momentum (here along the y direction) produced by the tilt of the beam propagation direction [22], defined as [27]

$$p_{\perp} = \frac{1}{\mathrm{kP}}\,\mathrm{Im}\int u_x^{\star}\nabla u_x \mathrm{d}x\mathrm{d}y. \tag{6}$$

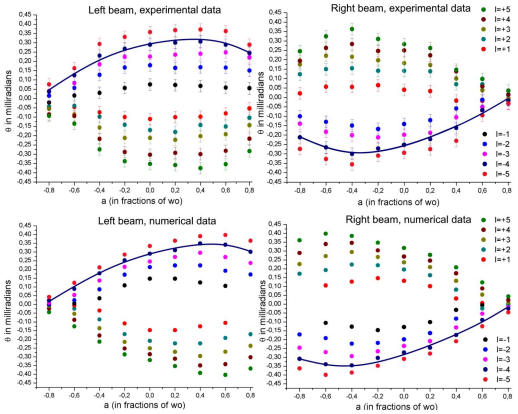

Fig. 3. Angular deviations θ_y, in milliradians, for various positions of a and values of ℓ. The first row shows experimental results for the split beams propagating to the left (L) and right (R) directions, respectively. The second row shows numerical results from the split beams propagating to the left (L) and right (R) directions, respectively. The blue line emphasizes the correlation between the right and left split beams for $\ell = -4$, in both experimental and numerical data.

The transverse canonical momentum along with the orthogonal displacement of the beam center produces EOAM. As the apex angle of the biprism is small, one can consider that angular deviations due to the orbital Hall effect produced by such a device are expected to be similar to the ones produced by edge diffraction.

To illustrate the similarity, we calculate values of the transverse canonical momentum along y for $\ell = -1$ for various values of a using the approach presented by Bekshaev [27], assuming an initially full and symmetric beam (related to the left panel of Fig. 3):

$$p_{\perp} = \mp\gamma\left[q + \sqrt{\pi}\,\mathrm{erfc}(q)\,\exp(q^2)\right]^{-1}, \tag{7}$$

with $q = a/w_o$, q scaling from −1 to +1 and $\gamma = (\sqrt{2}kw_o)^{-1}$. The results are presented in Fig. 4 and are compared with the

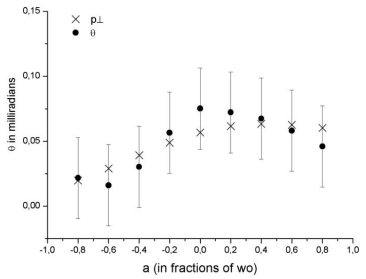

Fig. 4. Transverse angular momentum $p_{\perp}$ along the y direction, given by edge diffraction, compared with experimental angular deviation θ along y, for the left part of the beam, split with the Fresnel biprism (Fig. 3, upper left panel). Both configurations assuming an initial full and symmetrical LG beam of topological charge $\ell = -1$.

angular deviations obtained from the biprism configuration for one split beam part with $\ell = -1$.

Good agreement between the two methods is found. The numerical results slightly overestimate the angular deviations, which can be attributed to the technique chosen to perform integrations over the beam intensity profile.

In conclusion, we used a Fresnel biprism to perform a tunable symmetry breaking of an optical vortex beam. This configuration allows us to evidence orbit–orbit interactions in the form of angular deviations attributed to the optical orbital Hall effect. We also evidenced the rotation of the field transverse profile near the nominal propagation axis upon propagation, which direction depends on orbital momentum currents. We numerically and experimentally measure the angular deviations due to optical orbital effect. These results are compared with the expectation value of the transverse canonical momentum in the transverse direction for $\ell = -1$ using a model based on edge diffraction, which can be considered as a very similar configuration for the individual split beam parts. Good agreement is found between the two methods, and could be improved by refining the integration model over the intensity profile. The Fresnel biprism being a device that allows preservation of the two complementary split beams, we hope this work will open perspectives for entanglement studies as well as studies dealing with optical vortex symmetry breaking.

Funding. Ministério da Educação (MEC) (CAPES PROEX).

Acknowledgment. This work was supported by the CAPES PROEX scholarship. The authors also would like to thank the engineer H. C. Rigon for providing computational resources and support in the numerical implementation of our algorithm.

REFERENCES

1. Y. A. Kravtsov and Y. I. Orlov, *Geometrical Optics of Inhomogeneous Medium* (Springer-Verlag, 1990).
2. K. Y. Bliokh, F. J. Rodríguez-Fortuño, F. Nori, and A. Zayats, Nat. Photonics **9**, 796 (2015).
3. K. Y. Bliokh, Phys. Rev. Lett. **97**, 043901 (2006).
4. F. I. Fedorov, Dokl. Akad. Nauk SSSR **105**, 465 (1955).
5. K. Y. Bliokh and Y. P. Bliokh, Phys. Rev. E **75**, 066609 (2007).
6. A. V. Dooghin, N. D. Kundikova, V. S. Liberman, and B. Y. Zel'dovich, Phys. Rev. A **45**, 8204 (1992).
7. V. S. Liberman and B. Y. Zel'dovich, Phys. Rev. A **46**, 5199 (1992).
8. V. Fedoseyev, Opt. Commun. **193**, 9 (2001).
9. K. Y. Bliokh, I. V. Shadrivov, and Y. S. Kivshar, Opt. Lett. **34**, 389 (2009).
10. K. Y. Bliokh and A. Aiello, J. Opt. **15**, 014001 (2013).
11. M. R. Dennis and J. B. Götte, Phys. Rev. Lett. **109**, 183903 (2012).
12. H. Okuda and H. Sasada, J. Opt. Soc. Am. A **25**, 881 (2008).
13. K. Y. Bliokh and A. S. Desyatnikov, Phys. Rev. A **79**, 011807 (2009).
14. K. Y. Bliokh, M. A. Alonso, E. A. Ostrovskaya, and A. Aiello, Phys. Rev. A **82**, 063825 (2010).
15. X. Ling, X. Yi, X. Zhou, Y. Liu, W. Shu, H. Luo, and S. Wen, Appl. Phys. Lett. **105**, 151101 (2014).
16. A. Y. Bekshaev, K. A. Mohammed, and I. A. Kurka, Appl. Opt. **53**, B27 (2014).
17. A. Bekshaev and K. Mohammed, Opt. Commun. **341**, 284 (2015).
18. A. Y. Bekshaev, M. Soskin, and M. Vasnetsov, Opt. Commun. **241**, 237 (2004).
19. C. Huang, Y. Zheng, and H. Li, J. Opt. Soc. Am. A **33**, 2137 (2016).
20. H. Luo, S. Wen, and D. Fan, Phys. Rev. A **81**, 053826 (2010).
21. A. Bekshaev, J. Opt. A **11**, 094003 (2009).
22. A. Bekshaev, K. Y. Bliokh, and M. Soskin, J. Opt. **13**, 053001 (2011).
23. Z. Jin, Z. Xin-Xing, L. Xiao-Hui, C. Shi-Zhen, L. Hai-Lu, and W. Shuang-Chun, Chin. Phys. B **23**, 064215 (2014).
24. A. Sabatyan and S. A. Hoseini, Optik **124**, 5046 (2013).
25. L. Allen, M. W. Beijersbergen, R. J. C. Spreeuw, and J. P. Woerdman, Phys. Rev. A **45**, 8185 (1992).
26. J. W. Goodman, *Introduction to Fourier Optics* (McGraw-Hill, 1968).
27. A. Y. Bekshaev, J. Opt. **19**, 085602 (2017).
28. D. L. Andrews, *Photonics, Fundamentals of Photonics and Physics* (Wiley, 2015).
29. I. V. Basistiy, L. V. Kreminskaya, I. G. Marienko, M. S. Soskin, and M. Vasnetsov, Proc. SPIE **3487**, 34 (1998).
30. J. Hamazaki, Y. Mineta, K. Oka, and R. Morita, Opt. Express **14**, 8382 (2006).
31. S. M. Baumann, D. M. Kalb, L. H. MacMillan, and E. J. Galvez, Opt. Express **17**, 9818 (2009).
32. H. X. Cui, X. L. Wang, B. Gu, Y. N. Li, J. Chen, and H. T. Wang, J. Opt. **14**, 055707 (2012).
33. G. Guzzinati, P. Schattschneider, K. Y. Bliokh, F. Nori, and J. Verbeeck, Phys. Rev. Lett. **110**, 093601 (2013).
34. R. Simon and N. Mukunda, Phys. Rev. Lett. **70**, 880 (1993).
35. S. Feng and H. G. Winful, Opt. Lett. **26**, 485 (2001).
36. J. Arlt, J. Mod. Opt. **50**, 1573 (2003).

Dynamics of a double optical vortex beam

Claire M. Cisowski, Ricardo R. B. Correia

UFRGS
UNIVERSIDADE FEDERAL
DO RIO GRANDE DO SUL

Introduction

Optical vortices are scalar singularities where the phase of the optical field is undefined and its amplitude null.

Beams carrying a single central optical vortex can exhibit dynamical properties dependent on the vortex topological charge.

In this work we numerically investigate the dynamical properties of a gaussian beam containing two optical vortices.

Modelling a double optical vortex beam

The complex field of a paraxial, z-propagating beam carrying two optical vortices can be written as[1]:

$$u_1(z_1 = 0) \propto exp(-r^2/(w^2))exp(-i(\ell_a\phi_a(r - r_a) + \ell_2\phi_b(r - r_b)))$$

With ϕ_a and ϕ_b being the angles around the vortices positions r_a and r_b respectively and ℓ standing for the vortex topological charge, i.e, the number of 2π phase circulation in a closed circuit around the optical singularity.[2]

We embed pairs of optical vortices with various topological charges in a gaussian beam of waist radius 423 μm and wavelength 405 nm. Beam propagation is performed numerically based on the Rayleigh-Sommerfeld integral.[3]

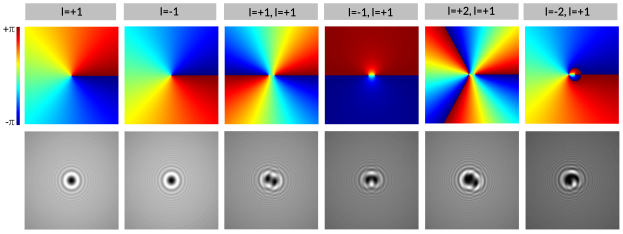

Figure 1. Phase (first row) and intensity (second row) distributions of a beam embedded with optical vortices of various topological charges. The distance between two vortices is 20μm.

Fluid-like rotation

Upon propagation, fluid-like rotations of the beam intensity profile are observed. The rotation rate and direction is dependent on the vortices topological charges. This effect is due to the fact that the Gouy phase is dependent on the beam's topological content.[4]

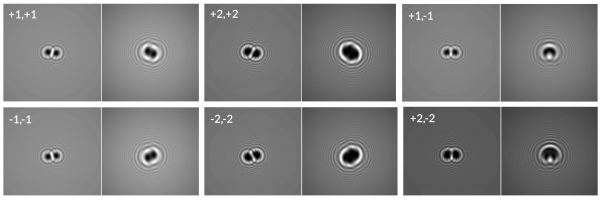

Figure 2. Intensity distributions for various vortex pairs for propagation distances 10 cm(left image) and 50cm(right image).

Vortex-vortex interactions

Upon propagation, vortices of high topological charge break into a constellation of vortices of unit charge.

Vortices of identical topological charge do not interact while vortices of opposite topological charge annihilate.

The annihilation distance varies with the topological strength of the initial vortices.

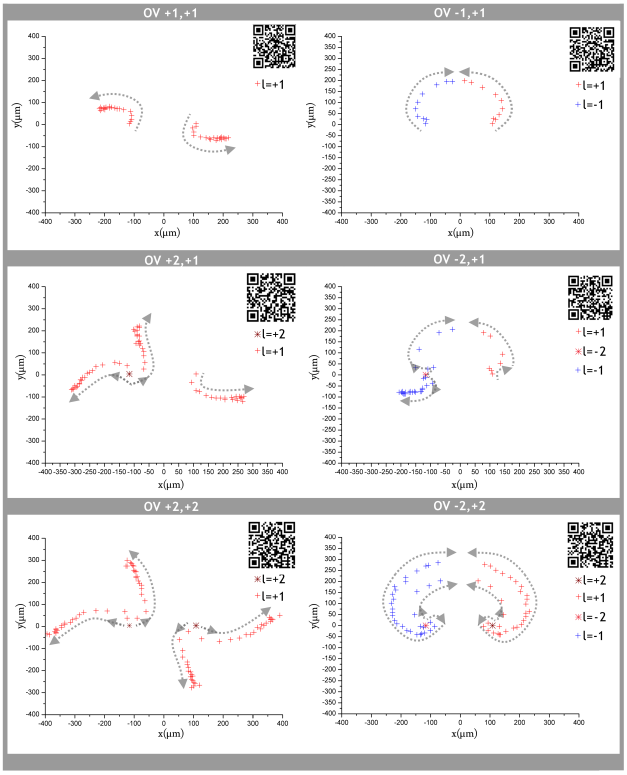

Figure 3. Trajectory of optical vortices cores when propagating from 0 to 250 cm. Light-gray arrows indicate the trajectory direction and QR codes are linked to the full evolution sequence.

Conclusion

The topological charge of individual vortices embedded in a gaussian beam influences the trajectory of each vortex core while modifying the beam intensity distribution upon propagation.

References

1. I. Freund "Critical point explosions in two-dimensional wave fields" Opt. Com. 159, 99-117 (1999)
2. A. Yao, M. Padgett "Orbital angular momentum, origin behavior and applications" Adv. Opt. P. 3 (2001)
3. J. Goodman "Introduction to Fourier Optics" McGraw-Hill (1968)
4. I. Bassisty, L Kreminskaya, I. Marienko, M. Soskin, M. Vasnetsov "Experimental observation of rotation and diffraction of a singular light beam"Proc. SPIE (1997)

-This work was made possible thanks to the Brazilian National Council for Scientific Development-